The impact of hydrological and climatic variations on the oxygen-18 content of atmospheric CO_2

by

Nikolaus Howard Buenning

B.A. University of Colorado, Boulder, 2002

M.S. University of Colorado, Boulder, 2006

A thesis submitted to the

Faculty of the Graduate School of the

University of Colorado in partial fulfillment

of the requirements for the degree of

Doctor of Philosophy

Department of Atmospheric and Oceanic Sciences

2010

The thesis entitled:
The impact of hydrological and climatic variations on the oxygen-18 content of atmospheric CO_2

Written by Nikolaus Howard Buenning

has been approved for the Department of Atmospheric and Oceanic Sciences

_____

Dr. David C. Noone

_____

Dr. James W. C. White

_____

Dr. Darin Toohey

Date: _____

The final copy of this thesis has been examined by the signatories, and we find that both the content and the form meet acceptable presentation standards of scholarly work in the above mentioned discipline.

Buenning, Nikolaus H. (Ph.D., Atmospheric and Oceanic Sciences)

Thesis directed by Dr. David C. Noone

Abstract

The ^{18}O composition of atmospheric CO_2 is a potentially valuable tracer of global interactions between the hydrologic and carbon cycles. The observed ^{18}O composition of atmospheric CO_2 (hereafter δC_a, where $\delta = (R/R_{standard}-1) \times 1000$ and R is the molar ratio of heavy to light isotopes) does not show a clear long-term trend, though almost all monitoring stations observed an impressive decrease in δC_a from 1992 to 1998. The cause(s) of this and other interannual δC_a variations are still relatively unknown, and this work aims to better understand the driving mechanisms that caused the observed interannual δC_a variations.

Observed interannual δC_a anomalies from Mauna Loa were correlated with anomalies of certain meteorological variables that could potentially affect δC_a. Negative correlation existed between δC_a and both relative humidity and precipitation amount within parts of the tropics. Positive correlations existed between δC_a variations and the ^{18}O content of precipitation for the same tropical regions. Rough estimates suggest that about 20% of the decrease in δC_a during the 1990s was due to increases in relative humidity and about 80% of the decrease was due to decreases in the $\delta^{18}O$ value of precipitation (and likely a consequence of increases in the amount of precipitation).

A global model was constructed to simulate atmospheric CO_2 and $CO^{18}O$ (and thus δC_a). This model employed an isotopic land model (ISOLSM) and the Community Atmosphere Model (CAM). The model is used for a series of sensitivity experiments to better understand how both steady-state and interannual varying δC_a respond to changes in relative humidity, $\delta^{18}O$

values of precipitation and water vapor, temperature, and light levels. δC_a responded the most to changes in the $\delta^{18}O$ values of precipitation and water vapor, with moderate responses to relative humidity changes. Model results suggest that the decrease in δC_a during the 1990s was due primarily to decreases in the ^{18}O composition of precipitation with a smaller a contribution from increased relative humidity. Thus, observations of δC_a may become a powerful integrative tool in the coming decades for monitoring large scale changes in the hydrological cycle should it accelerate under a warming climate, as predicted.

Contents

Tables

Figures

Chapter 1

Introduction

Atmospheric CO_2 is an important greenhouse gas in Earth's atmosphere, and its recent short-term variability (relative to geological times) is mostly controlled by five net fluxes. These include photosynthetic leaf fluxes, respiration, fluxes to and from the oceans, fossil fuel consumption, and biomass burning [*Sarmiento and Gruber*, 2002]. These last two fluxes have lead to the increase in atmospheric CO_2 concentration over the past several decades (Figure 1a). The same fluxes are also believed to be the primary cause for observed decrease in the carbon-13 content of atmospheric CO_2. This is because of $^{13}C/^{12}C$ ratios within present-day plants and ancient plants (i.e. fossil fuels) are lower than atmospheric ratios by about 2% [*Quay et al.*, 1991]. However, the oxygen-18 content of atmospheric CO_2 (hereafter denoted δC_a, where $\delta=(R/R_{Standard}-1) \times 1000$ and R is the molar ratio of heavy to light isotopes) is not observed to have any long-term increasing or decreasing trend (Figure 1.1). Instead, δC_a was about constant during the early 1990s, then decreased throughout the mid and late-1990s, and then began to increase after the year 1999. To better understand any potential cause for these variations, it is useful to examine the budget equation for δC_a values, which can be written as:

$$\frac{\partial C_a}{\partial t} = \frac{1}{C_a M}\left[F_A\Delta_A + F_r\Delta_r + F_o\Delta_o + \left(F_F + F_B\right)\Delta_F\right] \qquad (1.1)$$

where C_a is atmospheric CO_2 mixing ratio, M is a flux conversion factor, F values are fluxes (GtC yr^{-1}), Δ values are (apparent) discriminations (‰) against δC_a and subscripts A, r, o, F, and B refer to assimilation, respiration, ocean, fossil fuel and biomass burning, respectively. *Francey*

and Tans [1987] and *Farquhar et al.* [1993] have shown that the respiratory and photosynthetic leaf fluxes (i.e. the first two terms of equation 1) can largely influence δC_a values.

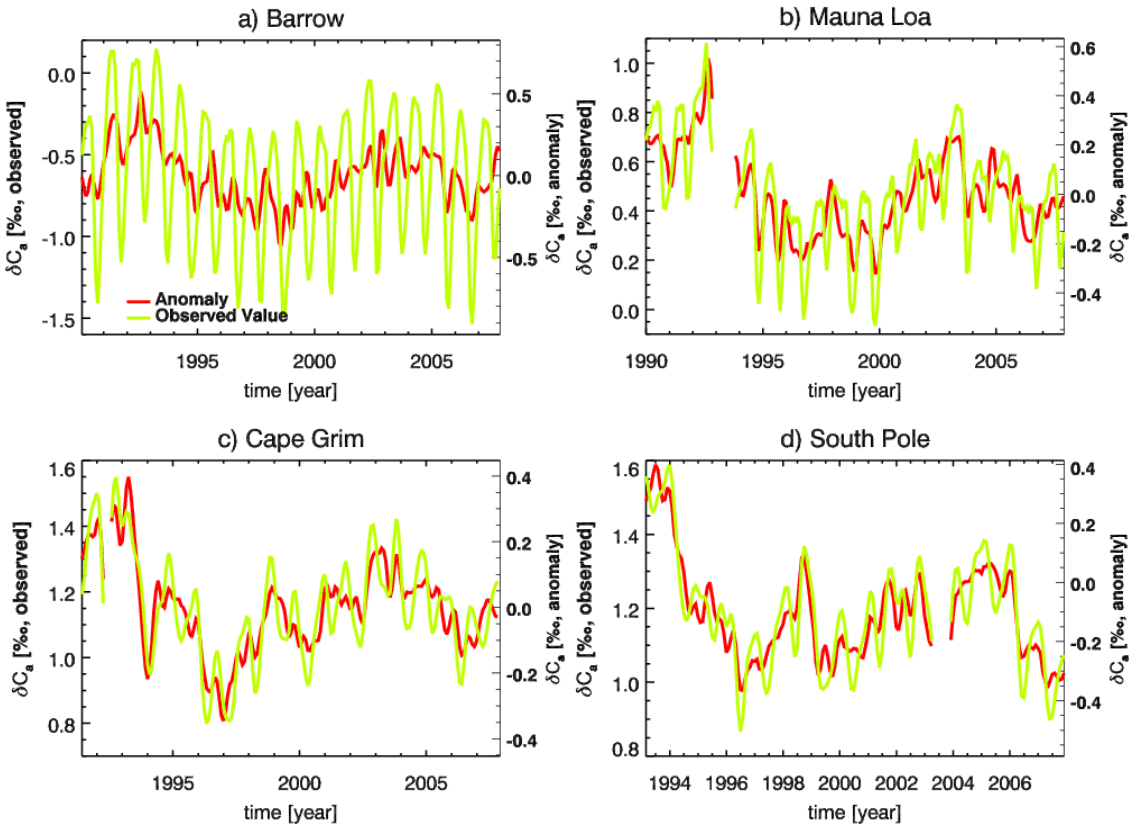

Figure 1.1 Observed seasonal and interannual variations of δCa (‰) at Barrow (a), Mauna Loa (b), Cape Grim (c), and the South Pole (d). The green line represents the observed values, while the red line represents monthly anomalies.

The respiration term can be rewritten as:

$$F_r \Delta_r = F_r \left[\left(\delta C_S - \delta C_a \right) + \varepsilon_S \right] \qquad (1.2)$$

where δC_S is the isotopic composition of soil CO_2 and, ε_S is fractionation associated with diffusion through the soil column. Autotrophic and heterotrophic respiration produces CO_2 within the soil column and the value of δC_S is largely dependent on the isotopic signature of local water (i.e., either root or bacterial medium water). The isotopic composition of soil-

respired CO_2 is further dependent on differential diffusion of CO_2 and $CO^{18}O$ through the soil column (ε_S), as well as the equilibration with soil water. A third process that influences δC_a is the "invasion effect" [*Tans*, 1998; *Miller et al.*, 1999; *Riley et al.*, 2002] in which atmospheric CO_2 diffuses into the top layer of the soil, attains the isotopic signature of the surface soil water through rapid isotopic equilibration, and diffuses back to the atmosphere. This invasion process is influenced by soil temperature and water content and atmospheric mixing conditions adjacent the surface, which in turn are influenced by radiation and evaporation, as well as the concentration of CO_2 immediately above the soil surface [*Miller et al.*, 1999; *Stern et al.*, 2001; *Riley*, 2005].

Similar to equation (1.2), the 2nd term in equation (1) can be rewritten as:

$$F_A \Delta_A = F_A \left[\frac{C_C}{C_a - C_C} \left(\delta C_l - \delta C_a \right) - \varepsilon_l \right] \tag{1.3}$$

where δC_l is the isotopic composition of CO_2 inside the stomatal cavity (C_C) and ε_l is the fractionation factor associated with diffusion through the stomatal interface.

The oxygen isotope exchange in leaves between water and CO_2 occurs primarily in mesophyll cells (adjacent to the stomatal cavity), where dissolved CO_2 molecules exchange oxygen atoms with mesophyll water [*Farquhar and Lloyd*, 1993; *Gillon and Yakir*, 2000]. In the presence of carbonic anhydrase, the catalyzed reaction occurs almost instantaneously [*Gillon and Yakir*, 2001]. During transpiration, the lighter water isotopologue evaporates and diffuses through the stomata more efficiently than the heavy isotopologue, thereby enriching leaf water. *Craig and Gordon* [1965] formulated a model to predict the isotopic composition of surface water, and *Flanagan et al.* [1991] modified the model to show that during steady-state conditions, the ratio of $H_2{}^{18}O/H_2{}^{16}O$ (R_l) at the evaporation site of a water body can be written as

$$R_{l-CG} = 1/\alpha_e \left(\frac{1}{\alpha_k} R_X \left(\frac{e_i - e_s}{e_i} \right) + \frac{1}{\alpha_{kb}} R_X \left(\frac{e_s - e_c}{e_i} \right) + R_{CV} \frac{e_c}{e_i} \right) \quad (1.4).$$

In equation (1.1) R_X is the ratio of the xylem/stem water ($H_2{}^{18}O/H_2O$), R_{CV} is the ratio of canopy water vapor, e_i (Pa) is the vapor pressure within the leaf, e_s is the vapor pressure at the leaf surface, e_c is the vapor pressure in the canopy, α_k is the water vapor kinetic fractionation for molecular diffusion, α_{kb} is the vapor kinetic fractionation for diffusion through a laminar boundary layer, and α_e is the temperature dependant equilibrium fractionation factor. The simple mass balance equation shows that the isotopic composition of the leaf water (δW_l) is related to that of the stem water (δW_X) which is set by the isotopic composition of soil water (δW_S) and also to the relative humidity ($h_l = e_c/e_i$). A relative humidity equal to zero causes the leaf water ratio to depend only on the ratio of the soil water (i.e., transpiration is a one-way flux out of the leaf). Likewise a relative humidity of 100% creates a thermodynamic equilibrium between water in the leaf and the ambient vapor, thus stopping transpiration. Observational studies [e.g., *Flanagan et al.*, 1991; *Roden and Ehleringer*, 1999] show that the isotopic composition of bulk leaf water under steady-state conditions varies with the isotopic composition of water vapor and relative humidity, in close agreement with the Craig-Gordon model. Therefore, changes in humidity can have significant impacts on the isotopic composition of leaf water, and consequently the ^{18}O composition of CO_2 fluxes from leaves to the atmosphere.

Farquhar et al. [1993] presented a basis for modeling δC_a and constructed a quantitative model based on isotopic budget considerations and included leaf exchanges. *Ciais et al.* [1997] extended this work by using an atmospheric tracer transport model to examine latitudinal variations as well as seasonal cycles of δC_a. Their model ingested surface fluxes generated from monthly mean statistics from a number of sources, including previous runs from a land surface

model [*Sellers et al.*, 1996a, 1996b], to evaluate terms describing ecosystem exchange in the budget proposed by *Farquhar et al.* [1993]. *Peylin et al.* [1999] used the same model framework to examine the role of different ecosystems on the seasonal and latitudinal variations of δC_a. This approach yielded promising results in the mean distributions (e.g. inter-hemispheric gradient) and amplitudes of seasonal variations, as well as dependence of δC_a on ecosystem type. *Cuntz et al.* [2003a, 2003b] examined such variations further by constructing the first comprehensive global three-dimensional model that allowed the atmosphere to interact with the biosphere, and thereby simulate diurnal cycles and transport of CO_2, $C^{18}OO$, and $H_2{}^{18}O$ in a more consistent manner than previous "off-line" calculations. In this manner, $CO^{18}O$ exchanges also depend explicitly on δC_a. The model simulated the observed north-south gradient credibly, and confirmed that the largest contribution to the gradient comes from assimilation and respiration fluxes. However, this comprehensive model simulated a seasonal cycle in δC_a with a two month phase lead over the observations, particularly at high northern latitudes. This deficiency was attributed to poorly modeled seasonal cycles in the isotopic composition of soil water.

Based on the National Center for Atmospheric Research (NCAR) Land Surface Model (LSM) [*Bonan*, 1996], *Riley et al.* [2002] developed an isotopic scheme (ISOLSM) that simulates the $\delta^{18}O$ values of H_2O reservoirs of the soil and plant, and the oxygen isotope exchanges of H_2O and CO_2. This model divides the canopy into sunlit and shaded leaves, and differentiates direct and diffuse light fluxes. *Riley et al.* [2002, 2003] used ISOLSM to show with sensitivity tests that significant changes in the isotopic composition of leaf, soil, and surface soil water result from variations of the $\delta^{18}O$ value of atmospheric water vapor and CO_2. They

also found that changes in the isotopic composition of leaf and stem water were as large as 2‰ with variations in assumed root depth, further supporting the claim of *Cuntz et al.* [2002b] that the details of the soil hydrology are very important for δC_a. These findings demonstrate that even subtle changes in the meteorological or physiological conditions can have substantial influences on the isotopic state of the terrestrial biosphere and consequently that of atmospheric CO_2 and $CO^{18}O$.

To obtain a better understanding of the observed variations of δC_a this body of work explores how variations in environmental conditions can affect the oxygen-18 content of CO_2 in the atmosphere. Considering equation 1.1-1.4, the interannual δC_a time-series observed at Mauna Loa is correlated with observed variations in the potential drivers of δC_a, and resulting changes to δC_a are approximated for regions where correlations exist (Chapter 2). Motivated by the findings of the correlation analysis, a model is constructed to simulate atmospheric CO_2 and $CO^{18}O$. ISOLSM is used to predict CO_2 and $CO^{18}O$ ecosystem fluxes, which (along with dataset-derived fluxes from oceans, fossil fuel consumption, and biomass burning) are incorporated into the NCAR Community Atmosphere Model (CAM) to simulate δC_a. Sensitivity tests are conducted using this model framework to evaluate how steady-state δC_a responds to changes in humidity, and the $\delta^{18}O$ value of precipitation and water vapor, temperature, and radiation levels (Chapter 3). This model is then reconfigured to simulate the interannual variations in δC_a, and experiments are conducted by eliminating the interannual variations of individual variables in order to quantify each variable's contribution to the year-to-year change in δC_a values (Chapter 4). The focus of the work then shifts to examine the isotopic composition of precipitation, and specifically how local and non-local processes affect the

annual mean and seasonal phases of observed and modeled δW_P (Chapter 5). This work then examines an additional application of ISOLSM in which the model is used to demonstrate how leaf water enrichment may have been different during an earlier point in time (Chapter 6). Specifically, ISOLSM is used to show how changes in environmental conditions can alter the isotopic composition of leaf water and influence the validity of a particular climate proxy. This work concludes with a recap of the findings and how they relate to one another, and perhaps more importantly, what knowledge is gained from this collective body of work (Chapter 7).

Chapter 2

Correlations between the observed interannual variations in $\delta^{18}O$ of atmospheric CO_2 and the hydrological cycle

2.1 Introduction

Direct monitoring of atmospheric CO_2, an important greenhouse gas, began at Mauna Loa in the late 1950s, and the global secular increase of CO_2 has been attributed to increases in fossil fuel emissions and land cover changes that release CO_2 [*Keeling*, 1961; *Denman et al*., 2007]. These fluxes have also influenced the carbon isotope composition of atmospheric CO_2. For example, the $^{13}C/^{12}C$ content of atmospheric CO_2 has been gradually decreasing from year-to-year due to increases in fossil fuel burning and subsequent changes in isotopic ocean fluxes [*Quay et al.*, 1992; *Francey et al.*, 1995; *Keeling et al.*, 1995; *Fung et al.*, 1997; *Rayner et al.*, 2008]. On the other hand, the $\delta^{18}O$ value of atmospheric CO_2 (δC_a) has not shown a multi-decadal trend at any of the monitoring stations (e.g., the measurements shown in Figure 1.1). However interannual variations appear to be consistent amongst these stations [*Ishizawa et al.*, 2002]. This work aims for a better understanding of the processes controlling these variations.

Modeling studies have led to a better understanding of the spatial structure and seasonality of atmospheric δC_a [*Farquhar et al.*, 1993; *Ciais et al.*, 1997a, 1997b; *Peylin et al.*, 1999; *Cuntz et al.*, 2003a, 2003b]. Using relatively simple atmospheric mass balance models, *Francey and Tans* [1987] and *Farquhar et al.* [1993] demonstrated that terrestrial ecosystem components largely determine the spatial structure of δC_a. Studies using more complex models have shown that both the north-south gradient and the seasonal cycle in δC_a are almost entirely driven by terrestrial ecosystem fluxes and atmospheric transport [*Ciais et al.*, 1997a, 1997b;

Peylin et al., 1999; *Cuntz et al.*, 2003a, 2003b]. None of these global modeling studies were aimed at understanding the interannual δC_a variations, though others have suggested that the year-to-year changes could be a result of terrestrial carbon flux anomalies [*Gillon and Yakir*, 2001; *Stern et al.*, 2001; *Ishizawa et al.* 2002; *Flanagan* 2005]. In contrast, *Still et al.* [2009], using a land surface isotope model, showed that regional δC_a variations could be driven by changes in the hydrological cycle (such as humidity and cloud cover variations). As such, there is no clear indication of what is controlling the observed interannual δC_a variations

This study seeks empirical evidence of potential drivers of the year-to-year variations in δC_a. To this end, both station observations and assimilated meteorological data were used to compute correlation coefficients between meteorological data and observed δC_a variations to determine regions and quantities that are potential drivers of the variability. Based on the magnitude of the temporal variations in the meteorological data and the relationships between meteorological variables and δC_a, first-order approximations are applied to evaluate which factors associated with climate variations might have contributed to the observed variability in δC_a and the decrease during the mid-1990s in particular.

2.2 Atmospheric Budget for $\delta^{18}O$ of atmospheric CO_2

2.2.1 CO_2 fluxes to and from the atmosphere

The total gross CO_2 flux from the surface to the atmosphere (F_{sa}) is the sum of individual gross fluxes from the five major sources:

$$F_{sa} = F_{la} + F_r + F_{oa} + F_f + F_u \qquad (2.1)$$

where F values are fluxes to the atmosphere (GtC y^{-1}) and subscripts *la*, *r*, *oa*, *f*, and *u* refer to leaf-to-atmosphere, soil and stem respiration, ocean-to-atmosphere, fossil fuel and land use changes, respectively (A complete list variables used here is given in Appendix 2.B). *Denman et al.* [2007, Figure 7.3] estimated these CO_2 fluxes (from *Sarmiento and Gruber* [2006], *Sabine et al.* [2004], and *Houghton* [2003]) as follows: F_r = 119.6 GtC y^{-1}; F_{oa} = 90.6 GtC y^{-1}; F_f = 6.4 GtC y^{-1}; and F_u = 1.6 GtC y^{-1}. *Denman et al.* [2007] also estimated global Gross Primary Production (GPP) to be 120 GtC y^{-1}. The global leaf-to-atmosphere CO_2 flux can be estimated as GPP times the enhancement factor [*Farquhar et al.*, 1993], C_C / (C_a-C_C) (where C_a and C_C are the CO_2 mixing ratio in the atmosphere and at the surface chloroplast within leaf stomata, respectively). This enhancement factor varies primarily with the relative amounts of C3 and C4 vegetation, as each plant type exhibits very different C_C values [*Still et al.*, 2009]. Using a biophysical model *Cuntz et al.* [2003a] calculated a global average of C_C /(C_a-C_C) to be approximately three. The global mean estimates calculated by *Ciais et al*. [1997a] and *Farquhar et al.* [1993] were 1.7 and 1.3, respectively. Any one of these three estimates could be correct. As such, the unbiased value assumed here is the average of the three estimates, which is two. Using an enhancement factor of two results in a flux from leaves of approximately 240 GtC y^{-1}. Combining F_{la} with the other fluxes yields a total gross global CO_2 flux from the Earth's surface to atmosphere (F_{sa}) of 458 GtC y^{-1}. Thus, approximately 52% (240 / 458) of the surface-to-atmospheric CO_2 should carry the isotopic composition of CO_2 that is set inside leaves, while 26% (119.6 / 458) should carry the isotopic label of respiration.

The total gross flux from the atmosphere to the surface (F_{as}) can be written as:

$$F_{as} = F_{al} + F_{ao} \qquad (2.2)$$

where subscripts *al* and *ao* refer to atmosphere-to-leaf and atmosphere-to-ocean, respectively. The global atmosphere-to-leaf CO_2 flux can be estimated as GPP times C_a / (C_a-C_C). With an atmospheric CO_2 mixing ratio of 385 ppm and an enhancement factor of two, would suggests that the C_a / (C_a-C_C) factor is approximately three (i.e., F_{al} is three times GPP). Using GPP reported by *Denman et al.* [2007] results in the global atmosphere-to-leaf CO2 flux equal to 360 GtC y^{-1}. *Denman et al.* [2007] estimated the atmosphere-to-ocean flux to be 92.8 GtC y^{-1}. Thus, 80% of the global atmosphere-to-surface CO_2 flux is due to atmosphere-to-leaf fluxes. Theses fraction as well as the ones mentioned above will be used to estimate changes to δC_a values in section 2.5.

2.2.2 Potential drivers of $\delta^{18}O$ of atmospheric CO_2

The mass balance for δC_a can be written fluxes defined above and their apparent discriminations against atmospheric $CO^{18}O$ (Δ, ‰) [*Farquhar et al.*, 1993; *Ciais et al.*, 1997a, 1997b, *Cuntz et al.*, 2003a, 2003b]:

$$\frac{d(\delta C_a)}{dt} = \frac{1}{C_a M}\left[F_A\Delta_A + F_r\Delta_r + F_o\Delta_o + (F_f + F_u)\Delta_f\right] \qquad (2.3)$$

where M is a CO_2 unit conversion factor (2.122 PgC ppm^{-1}) and subscripts A, r, o, f, and u refer to assimilation, respiration, ocean, fossil fuel consumption, and land use changes, respectively. In equation (2.3), F_A equals GPP minus leaf respiration, and thus all other ecosystem respiration is contained in the F_r term. The terrestrial ecosystem fluxes comprise the first two terms within the brackets of equation (2.3), which can be rewritten as [*Farquhar and Lloyd* 1993; *Ciais et al.* 1997a]:

$$F_A \Delta_A = F_A \left[\frac{C_C}{C_a - C_C} \left(\delta C_l - \delta C_a \right) - \varepsilon_l \right] \quad (2.4)$$

$$F_r \Delta_r = F_r \left[\left(\delta C_S - \delta C_a \right) + \varepsilon_S \right] \quad (2.5)$$

where ε values are diffusive fractionation factors, and subscripts l and S refer to leaves and soil, respectively. Equation (2.3) shows that δC_a may respond to changes in assimilation or respiration due to factors such as light levels, relative humidity or precipitation. Similarly, one would expect δC_a to be affected by changes in δC_l and δC_S (the $\delta^{18}O$ value of leaf and soil CO_2), via changes to Δ_A and Δ_r in equation (2.3).

δC_l and δC_S are primarily controlled by the isotopic composition of the water pools with which CO_2 interacts (the leaf and soil water, δW_l and δW_S) during leaf photosynthesis and soil and stem respiration. The isotopic composition of soil-respired CO_2 also depends on isotopic kinetic fractionation from diffusion of molecular CO_2 and $CO^{18}O$ (accounted for in the ε_S term). Another process that influences the isotopic composition of soil CO_2 fluxes is atmospheric CO_2 diffusing into the upper layers of the soil, attaining the isotopic signature of the surface soil water through rapid equilibration, and diffusing back to the atmosphere without any net flux to or from the atmosphere (the so-called amount effect [*Tans* 1998; *Miller et al.*, 1999; *Riley et al.*, 2002; *Riley*, 2005]). This effect is not directly accounted for in the analysis below, though the isotopic composition of CO_2 fluxes from soils is assumed to be dependent on the isotopic composition soil water.

Within leaves, CO_2 in the stomatal pore equilibrates with liquid water rapidly through hydration reactions catalyzed by the ubiquitous enzyme carbonic anhydrase. Thus, δC_l is primarily determined by δW_l plus a temperature-dependent equilibrium offset. *Craig and Gordon*

[1965] formulated a model to predict the isotopic composition of surface water, and the model has been modified [*Flanagan et al.*, 1991] to estimate the steady-state isotopic composition of leaf water at the evaporation site at the bottom of leaf stomata

$$\delta W_{l-CG} = \varepsilon_{LV}(T) + (1 - h_l)(\delta W_X - \varepsilon_k) + h_l \delta W_{CV} \qquad (2.6),$$

where $\varepsilon_{LV}(T)$ is the temperature-dependent equilibrium fractionation of $H_2{}^{18}O$ during the liquid-vapor phase transition (~9.8‰ at 298K [*Horita and Wesolowski*, 1994]), ε_k is the kinetic fractionation of $H_2{}^{18}O$ during diffusion of vapor across the stomata (-32‰ [*Cappa et al.*, 2003] or 28‰ [*Luz et al.*, 2009]) and leaf boundary layer (-21‰ [*Cappa et al.*, 2003]), h_l is relative humidity at the leaf surface, δW_X is the isotopic composition of the xylem (stem) water, and δW_{CV} is the isotopic composition of the canopy vapor. δW_X and δW_{CV} are primarily influenced by the isotopic composition of soil water (which is dependent on the isotopic composition of precipitation, δW_P) and atmospheric vapor, δW_{AV}. Because the isotopic composition of soil water is typically enriched relative to vapor [*Dansgaard*, 1964; *Ciais et al.*, 1998a; *Zhang et al.*, 2009] and because h_l determines kinetic fractionation strength, equation (2.6) predicts δW_l will decrease as relative humidity increases (and vice versa). As such, it is likely that interannual variability in relative humidity would cause variations in δC_a via changes in the isotopic composition of leaf water (and thus CO_2) within the stomatal cavity. Indeed, differentiating equation (2.6) with respect to h_l shows that a relative humidity increase of 1% at constant temperature corresponds to a δW_l decrease of approximately 0.36‰ (given ε_k = -26‰ and δW_{CV} - δW_S = -10‰). However, this dependence is reduced when considering non-steady state effects and diffusive mixing of xylem water and water at the leaf evaporation site (i.e. the Péclet effect) [*Farquhar and Lloyd*, 1993].

Oceanic fluxes of CO_2 are thought to only have minor influences on δC_a [*Ciais et al.*, 1997a; *Cuntz et al.*, 2003a], largely because of low discriminations (Δ_o), relative to terrestrial fluxes. Because of this small influence, this study will focus mostly on the terrestrial ecosystem components of equation (2.3), with minor considerations to the ocean component in the middle and high-latitudes where the ocean discrimination may be larger.

The budget consideration given above highlights three processes that could potentially dominate variations in δC_a: (1), relative humidity and its influence on leaf water isotopic composition; (2) the isotopic composition of precipitation and water vapor and their impact on leaf and soil water $\delta^{18}O$ values; and (3) gross CO_2 fluxes, especially assimilation and respiration, which are sensitive to changes in temperature, light levels, and moisture availability. The intent of this paper is to seek quantitative evidence for the relative importance of each of these from observations.

2.3 Methods and Data

2.3.1 Isotope Data

Observed δC_a used here come from the Stable Isotope Lab at the Institute of Arctic and Alpine Research and NOAA's Earth System Research Laboratory, Global Monitoring Division. These data span 1990 to 2007 and come from flask samples that are dried to avoid potential ^{18}O exchange between water and carbon dioxide [*Gemery et al.*, 1996]. CO_2 is then extracted from the sample and its isotopic composition is measured relative to CO_2 in a reference gas using a dual-inlet mass spectrometer. The precision of these measurements is 0.03‰ and the uncertainty of the absolute value is 0.07‰ [*White and Vaughn*, 2009].

Observed interannual variations in the isotopic composition of precipitation (δW_P) used here comes from the Global Network for Isotopes in Precipitation (GNIP) database, which is a joint project of the International Atomic Energy Agency and the WMO [*Isotope Hydrology Section*, 2006]. Unfortunately, there are only 295 stations that have at least 1 continuous year of observed monthly mean $\delta^{18}O$ values. Furthermore, many of the stations ceased to measure water isotopes after 1990 (when consistent δC_a observations typically began), thus there is only a limited amount of precipitation isotope data to use for the statistical analysis. Only 69 GNIP stations (most of which are located in Europe) have 90 or more months of data that overlap with the Mauna Loa δC_a record used in the analysis.

2.3.2 Meteorological Data

Relative humidity and temperature data were compiled from the Global Summary of the Day from the National Climatic Data Center and the World Meteorological Organization (WMO). This network of observations consists of 30,727 stations, though only about 7000 have sufficient data in recent years (130 or more months of data from 1990 to 2007). These stations cover mostly continental regions with large gaps in Sahara, Siberia, Greenland, and Antarctica. The WMO station observations span from 1929 (i.e., well before modern $CO^{18}O$ measurements began) to the present and are updated daily within 1-2 days after the observation. The solar radiation data came from the gridded product of *Qian et al.* [2006], who adjusted the NCEP/NCAR reanalysis radiation data based on radiation/cloud cover relationships and station cloud cover data [*New et al.*, 2002; *Mitchell et al.*, 2004; *Dai et al.*, 2006]. The mean bias in the reanalysis radiation is further minimized by using an atmospheric radiation transfer model and the cloud, surface, and atmospheric properties from the International Satellite Cloud Climatology

Project (ISCCP) [*Zhang et al.*, 2004], which was found to correlate well with the high-quality Baseline Surface Radiation Network measurements for the 1992-2001 period ($r = 0.98$). Monthly precipitation data was taken from version-2 of the combined precipitation dataset of the Global Precipitation Climatology Project (GPCP) [*Adler et al.*, 2003], which is a gridded product (at 2.5° resolution) based on low-orbit satellite microwave data, geosynchronous-orbit satellite infrared data, and surface rain gauge observations. Monthly mean values were calculated for each station (or grid-cell in the case of radiation), and similar to the observed δC_a values, long-term monthly means were removed from each station or grid-cell's time series. This is done because it is the interannual variations (not the seasonal variations) that are of interest.

2.4 Results

2.4.1 Correlations among station observations

The auto-correlations of monthly δC_a anomalies approach zero with a 3-year lag for all four sites (Figure 2.1). The highest correlations at zero lag between different stations are between Mauna Loa and Barrow and Cape Grim. Between Barrow and Mauna Loa, the correlation is the highest when Barrow is lagged by 1-2 months (Figure 2.1b). This small lag suggests that near synchronous interannual δC_a variations are observed throughout the Northern Hemisphere on a monthly time-scale and perhaps the source of the variations originates within the tropics. This signal takes about 6 to 8 months to reach Cape Grim as the correlation increases from $r = 0.714$ to $r = 0.746$ when the Cape Grim time series is lagged by 6 months. Similar results also emerge for the South Pole, where correlations are higher and statistically significant ($p \leq 0.05$, as per the discussion below) when the South Pole time-series is lagged by 9 to 10

months with respect to Mauna Loa and Barrow observations, and 7 to 8 months when correlated with Cape Grim. This suggest that the δC_a signal originates in the tropics and/or Northern Hemisphere and then is transported into the Southern Hemisphere, which is expected considering the scarcity of productive ecosystems in the Southern Hemisphere outside of the tropics. Furthermore, these variations are first observed at Mauna Loa before reaching the other 3 stations.

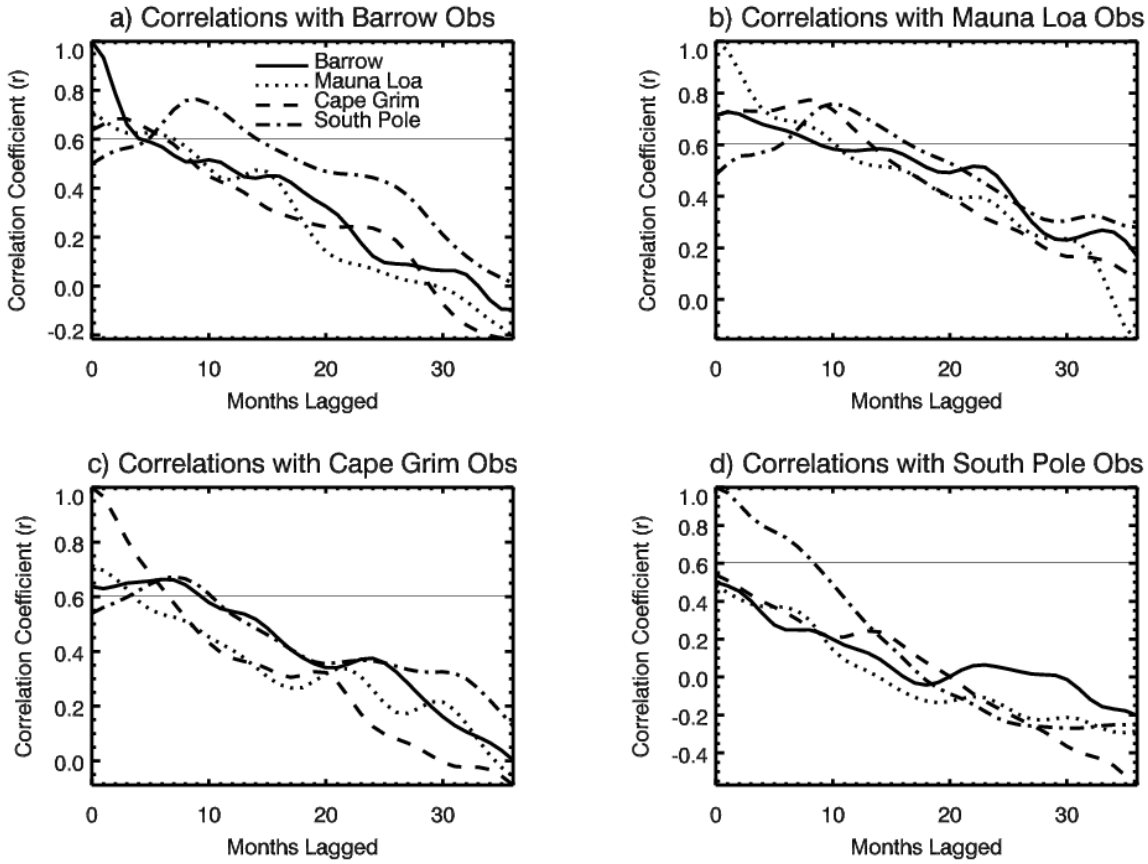

Figure 2.1 Correlation coefficient when four NOAA stations are correlated with one another with different lags. The thin solid line shows where the correlation is significant at the 95% level, assuming 11 degrees of freedom.

In light of these findings, the remainder of this study will focus on the Mauna Loa time series. The Mauna Loa record begins in January 1990 and goes through December 2007, with 11 missing months from December 1992 to October 1993, making for a total of 205 months to use for the correlation analysis. Figure 2.1b shows that the autocorrelation is above 0.602 ($p \leq 0.05$) for a lag of 1 to 6 months, but goes to zero with more than a 33-month lag. To estimate the degrees of freedom with the Mauna Loa time series, the turnover time of isotopic oxygen in atmospheric CO_2 (τ) is calculated assuming the atmosphere contains 762 GtC [*Denman et al.*, 2007] and the surface-to-atmosphere flux equals 458 $GtCy^{-1}$ (section 2.2.1), yields a turnover time of 1.66 years. Thus, it is assumed here that every 1.66 year interval is independent (τ ~1.66 year), and the degrees of freedom (N) is not 205 monthly values but rather 11. With this value of N, the statistical significance limits of r (using 2 sided p-values) at the 99%, 95%, 90%, and 80% confidence level are 0.735, 0.602, 0.521, and 0.419, respectively. Correlation coefficients were computed from the monthly anomalies (r), and to decipher the contribution of low frequency variations to the values of r, low frequency correlations (r_L) are found with high frequency variations in the meteorological data and δC_a removed by applying a low pass filter that removes periods shorter than 3 years (the approximate lag with which the autocorrelation of Mauna Loa δC_a goes to zero). Similarly, correlations are calculated with low frequency variations, periods longer than 3 years, removed (r_H).

2.4.2 Correlations with Mauna Loa δC_a

The Mauna Loa δC_a record exhibits robust negative correlations with relative humidity (which is consistent with enrichment of leaf water) in Southeast Asia / Indonesia / Northern

Australia (hereafter Asia Pacific region); southern Central America and northern South America (hereafter the Tropical Americas); Central and Eastern Europe; central North America; Southeastern Africa; and near the coast of Antarctica (Figure 2.2a). Regions where meteorological station density is high are resolved in Figures 2.2c-2.2f, which also shows positive correlations in each region that oppose the anticipated leaf water enrichment mechanism. There were no stations with negative r values above the 99% confidence level, 2 above the 95% level, 13 above the 90% level, and 60 above the 80% level. Many of the correlation values found in North America increase when δC_a was lagged by 2 years (Figures 2.2e and 2.2f). The increase in correlation values may be expected, as τ is approximately 1-2 years (section 2.4.1), so δC_a may take 1-2 years to respond to sustained forcing from that region over that period. Positive correlations are found in France, Eastern U.S., the Middle East, and Argentina (with no lag). Since one might expect the strongest signal to be associated with the time of year when CO_2 fluxes are largest, the analysis was repeated using a dataset in which only the growing season months were retained. The growing season analysis was remarkably similar to the full annual data (specifically, no change in the regions where consistent negative and positive correlations were found).

Only five GNIP stations within the tropics have over 90 months of δW_P observations during the 1990-2005 period, while no systematic observations of tropical δW_{AV} exist. Two of these five stations have positive correlations with δC_a above 0.2: Bangkok, Thailand (r = 0.284, r_L = 0.682) and Izobama, Ecuador (r = 0.201 and r_L = 0.553). Two of the other three stations are on remote islands and the fifth station is in Ethiopia. Darwin, Australia has the 2nd longest record for the Asia Pacific region during the 1990-2005 period: 64 months, r = 0.296, r_L = 0.639 (Figure 2.3). For all three stations, values of r_H were much smaller and of opposite sign.

Furthermore, the values of r_L were always positive and larger, an indication that the positive correlations were primarily due to low frequency (periods greater than 3 years) variations.

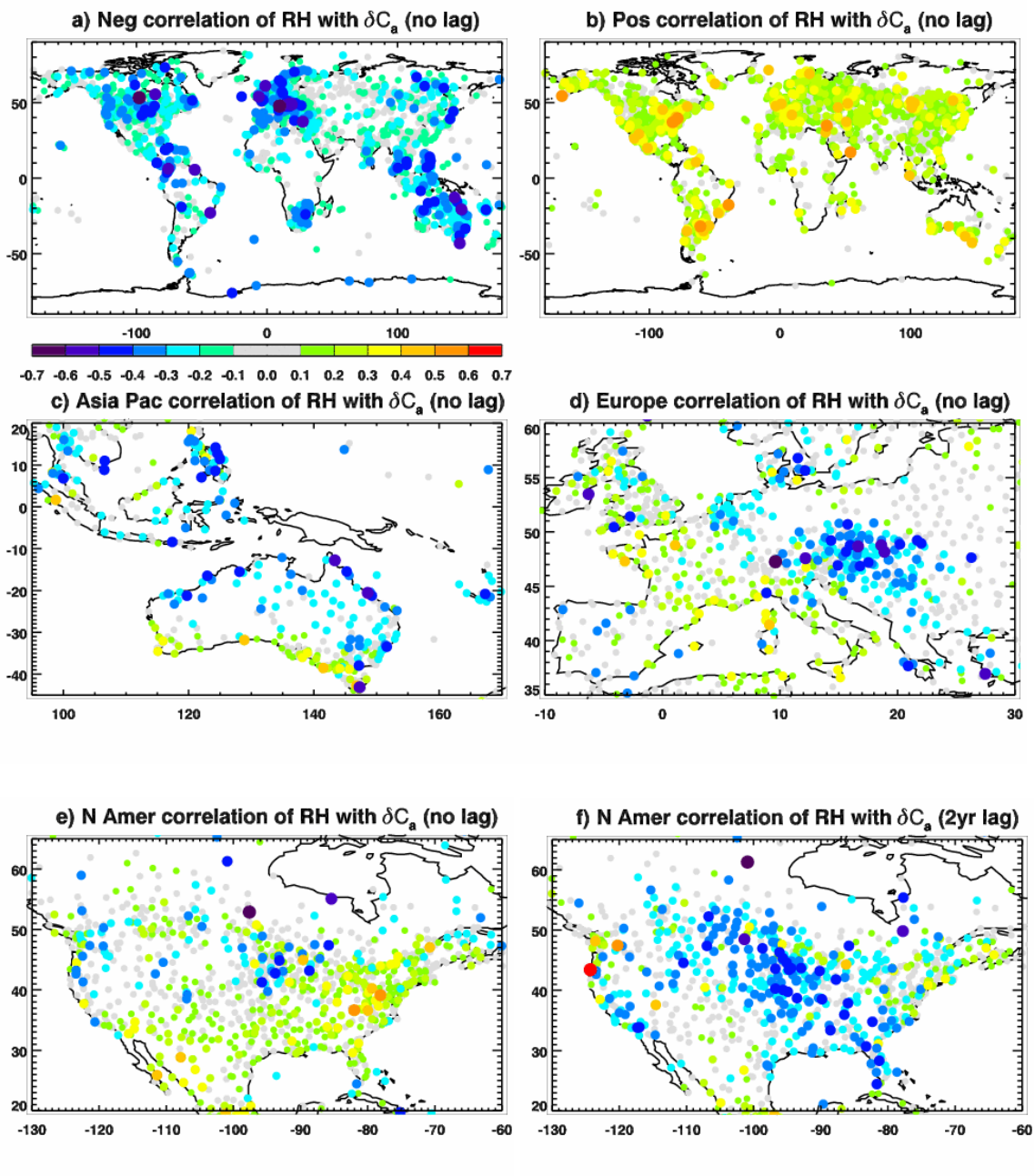

Figure 2.2. Negative (a) and Positive (b) station correlation coefficient (r) of observed relative humidity and Mauna Loa δC_a values (‰). Zoomed in correlations are shown for Southeast Asian region (c), Europe (d), and North America (e). Correlations in North America increase when a 2-year lag is applied for the North American shown in (f).

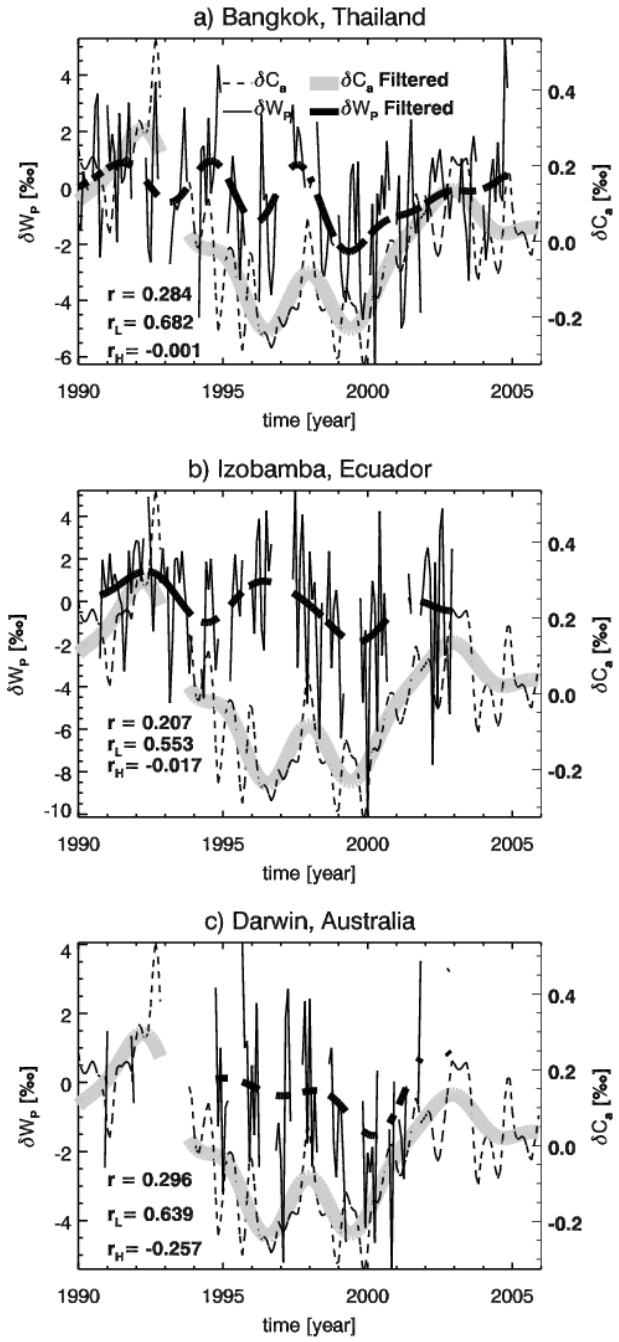

Figure 2.3. Station δW_P (‰) time-series (thin solid line) for 2 stations within the Southeast Asian region (a and c) and 1 in the tropical Americas (b). Also shown is the Mauna Loa δC_a (‰) time-series (dotted line). High frequency filtered δW_P values are shown as a thick solid line.

Assimilation of carbon by plants can be limited by a number of factors including air temperature. Temperature can also influence terrestrial $CO^{18}O$ exchanges in many ways, including changes to H_2O-CO_2 equilibrium fractionation, changes to liquid-vapor equilibrium fractionation, and influencing leaf surface relative humidity and stomatal conductance (which in turn influence C_C, F_{la}, and F_{al}) [*Still et al.*, 2009]. Negative correlations were found between observed air temperatures and δC_a over Eastern Canada and various arid regions such as the Middle East, Argentina, and the Chihuahuan Desert (Figure 2.4a). Because τ is approximately 1-2 years, correlation coefficients were also calculated with 1 and 2 year lags. The magnitude of the correlations was reduced with the lags, though with a 2-year lag robust negative correlations are found throughout much of South America (Figure 2.4c). Positive correlations with temperature are found in the same regions where negative relative humidity correlations are found (Figure 2.4b), such as central and western North America, Southeastern Africa, Central and Eastern Europe, Tropical Americas, and the Asia Pacific. Similar to the relative humidity results, correlations are stronger over North America with lags applied to δC_a (Figure 2.4d).

As discussed above, δC_a could also be influenced by a change to one of the fluxes in equation (2.3). Within the tropics, a change to assimilation could occur due to a change to either solar radiation at Earth's surface or water availability [*Nemani et al.*, 2003]. As such, and to facilitate budget calculations below, δC_a at Mauna Loa was also correlated with solar downwelling radiation and precipitation totals. Within the Asia Pacific region, positive correlations exist between solar downwelling radiation and δC_a (Figure 2.5a). No clear correlation sign was found for the Tropical Americas and the Congo. Similar to relative humidity, precipitation amount negatively correlates with Mauna Loa δC_a values in the Asia Pacific and most of the Tropical Americas, which extends across the Atlantic and into the

Western Congo (Figure 2.5b). Also the correlations for solar radiation flux and precipitation do not improve when lags are applied to δC_a.

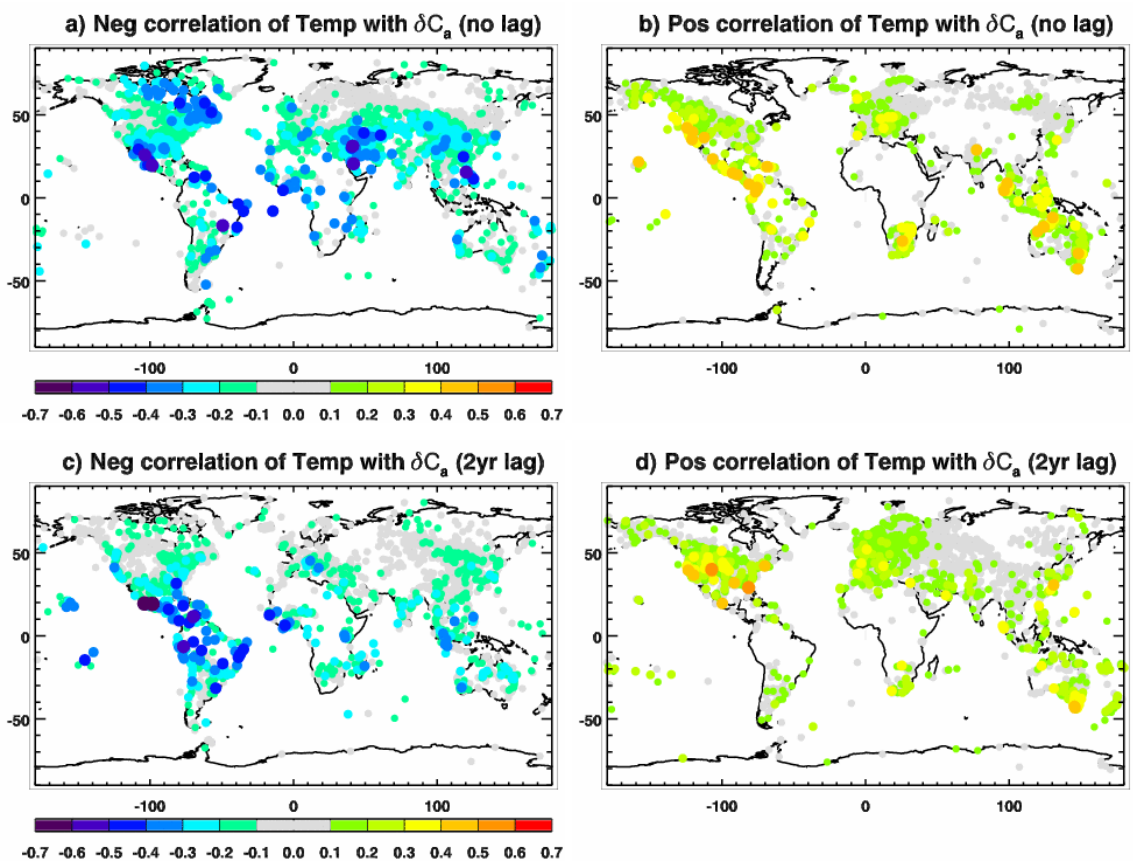

Figure 2.4. Stations with positive (a) and negative (c) correlations with observed temperature and observed Mauna Loa δC_a values (‰). Correlation coefficient (r) is represented via the color bar. Positive correlations with a 2-year lag (b) and negative correlations with a 2-year lag (d) are also shown.

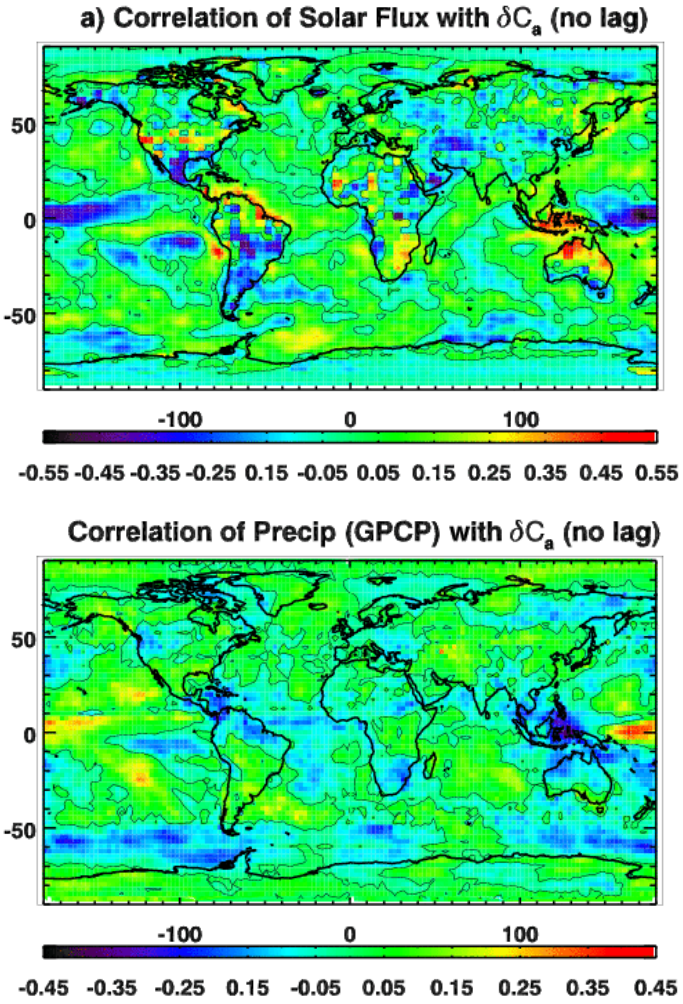

Figure 2.5 Correlation coefficients between observed monthly δC_a (‰) anomalies from Mauna Loa with solar radiation (a) and precipitation (b). Black contour line indicates the 0 contour line.

2.5 Discussion

2.5.1 Magnitude of relative humidity variations

This study seeks to reconcile the magnitude of the relative humidity variations identified by the correlation analysis with the budget and observed variations in δC_a. In particular, the focus here is on the difference in δC_a that arose from the gradual decrease during the mid-1990s. Specifically, the aim here is to determine which components contributed to the low frequency

δC_a drop of 0.5‰ over the course of the decade. Derived in Appendix 2B, the change in δC_a due to changes in the isotopic composition of a CO_2 flux F (e.g. the leaf-to-atmosphere flux) is estimated as:

$$D(\delta C_a) = D(\delta F) f_g f_R \qquad (2.7)$$

where D refers to the finite change (during the 1990s), δF is the isotopic composition of a flux F, f_g is the fraction of the global gross flux to the atmosphere from equation (2.1) (and computed in section 2.2.1), f_R is the fraction of the global flux from a particular region. The value of f_R was calculated from results of the CASA (Carnegie-Ames-Stanford) biosphere model [*Potter,* 1999; *Potter et al.*, 1999], which includes Net Primary Production (NPP) and heterotrophic respiration.

As mentioned above, high negative correlations were found for relative humidity within the tropics in the Asia Pacific and Tropical American regions, though some positive correlations were found in these regions. These high negative correlations are consistent in sign with the relationship between relative humidity and $\delta^{18}O$ values of leaf and soil water (δW_l *and* δW_S) and the subsequent effects on the isotopic composition of soil and leaf CO_2 fluxes (δF_{la} *and* δF_r). The regional average relative humidity time series is computed using all stations with 130 or more months of temperature and dew-point observations (i.e. relative humidity observations) within a particular region. The results for six regions are shown in Figure 2.6, and the longitudes and latitudes used to define each region is given in each panel in Figure 2.6. Observed δC_a anomalies at Mauna Loa are also shown with the scale reversed to reflect the expected relationship. Also shown in Figures 2.6 are humidity and δC_a variations with high frequency variations removed by applying a low-pass filter that removes periods shorter than 3 years. The time series shows that these higher correlations were largely associated with low humidity in the

early 1990s, higher humidity in the late 1990s, and decreasing relative humidity after then. Indeed, the correlations in these six regions are primarily a consequence of the low frequency variations in both relative humidity and δC_a (as is reflected in the values r, r_L, and r_H in Figure 2.6). These results suggest the potential for the low frequency tropical relative humidity variations to be a control on the inter-annual variability of δC_a.

Equation (2.7) was used to estimate the change in δC_a due to changes to the isotopic composition of leaves within the tropics induced by relative humidity variations. It was found that the regional mean increase in relative humidity during the 1990s for the stations in the Asia Pacific and Tropical America regions was 4.0% and 3.0% (respectively) when high frequency variations were removed (Figures 2.6a and 2.6b). Weighting these two numbers by regional NPP (from CASA) results in an average increase in relative humidity of 3.3%. Assuming $\partial(\delta W_l)/\partial h$=0.36‰%$^{-1}$ (section 2.2.2), a 3.3% increase in relative humidity would drive a 1.2‰ decrease in δW_l and the $\delta^{18}O$ value of fluxes from leaves, resulting in $D(\delta F)$ = 1.2‰. Furthermore, results from the CASA model suggest that the two regions in Figure 2.6a and 2.6b comprise about 19% of the global annual NPP (i.e., f_R = 0.19). From equation (2.7), these numbers result in an estimated change in δC_a of 0.12‰ due to the influence of tropical relative humidity variations on the isotopic composition of tropical leaf water (i.e,. 1.2‰ × 0.52 × 0.19 = 0.12‰). This is less than half of the 0.5‰ observed during the 1990s.

The increase in relative humidity in these two tropical regions would also cause changes in other variables that would affect δC_a. For example, increases in humidity would decrease soil evaporative enrichment and cause the isotopic composition of soil respiration to decrease, thus enhancing the 0.12‰ change from tropical leaf fluxes. On the other hand, an increase in humidity would likely drive an increase in photosynthesis (due to an increase in stomatal

conductance), which would tend to enrich the atmosphere, opposing any decrease in δC_a. This latter issue will be addressed further in subsection 2.5.3.

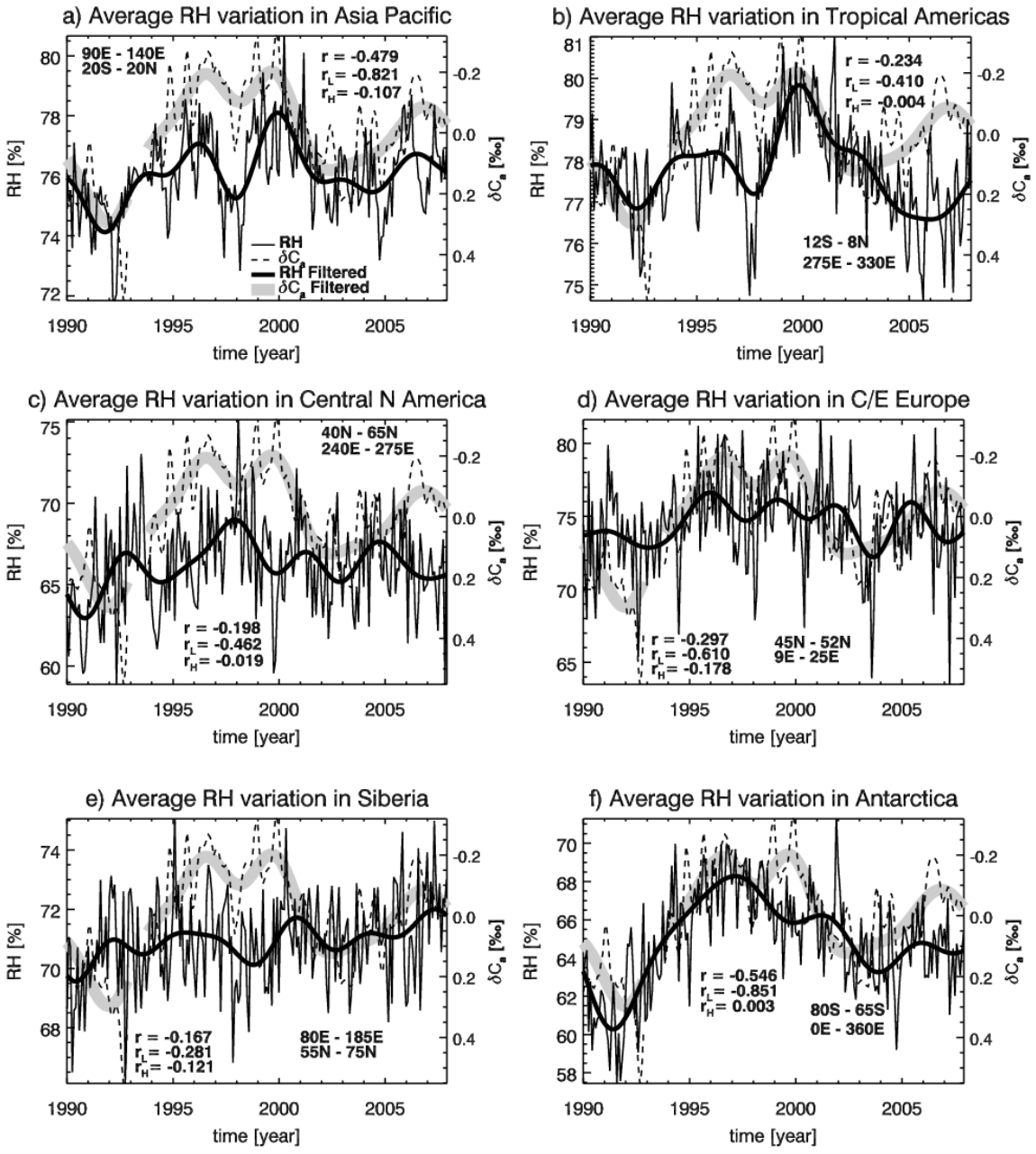

Figure 2.6. Station relative humidity (%) time-series (thin solid line) averaged over the Asian Pacific (a), Tropical Americas (b), Central North America (c), Central and Eastern Europe (d), Siberia (e), and off the Antarctic coast (f).. High frequency filtered time-series is shown as a thick solid line. Observed δC_a values from Mauna Loa are also shown (dotted line and thick gray line) and the scale is reversed for better comparison.

In the northern middle to high-latitudes, high negative correlations are found in Central and Eastern Europe, Central North America, and a region within Siberia. Figures 2.6c through 2.6e shows the average relative humidity variations for these three regions. The increase in relative humidity during the mid-1990s is most prominent in central North America, where the low frequency component increases by 6.0%. The regional average humidity in Europe and Siberia only increased by 3.3% and 1.6%, respectively. Weighting these values by regional NPP resulted in an average 3.2% increase in relative humidity, which would yield a 1.2‰ decrease in δW_l values (assuming steady-state). The estimated change to δC_a due to relative humidity variations in these northern regions are computed assuming $D(\delta F)$ = 1.2‰, f_g = 0.52, f_R = 0.12 (from the CASA model), yielding a δC_a change of 0.075‰. This estimated value indicates that relative humidity in the middle and high-latitudes did contribute to the decrease in δC_a during the 1990s.

Figure 2.2b reveals that Mauna Loa δC_a positively correlates with relative humidity for some regions: France, Eastern U.S., Mexico, the Middle East, and Argentina. However, it was found that there was little to no decrease in relative humidity over the Eastern U.S. and the Middle East during the 1990s, rather the positive correlations were mostly related to variations after the 1997/1998 El Niño. For the other regions it was found that NPP-weighted relative humidity decreased by 4.1% during the 1990s. Using the same reasoning as before would imply that $D(\delta F)$ has a value of 1.5‰. Results from CASA reveal that these regions contribute 6.9% to the global total NPP (f_R = 0.069). With these values and f_g equal to 0.52 results in an estimated increase of 0.054‰. Thus, the overall change in δC_a from relative humidity variations outside of the Asia Pacific and Tropical Americas is relatively small (0.021‰).

Relative humidity values in coastal Antarctica increased during the 1990s (Figure 2.6b). Considering only low frequency variations, it was found that the regional average relative humidity increased by 8.0% from 1991 to 1997. This is a region where ocean fluxes are high and tend to enrich the atmosphere with $CO^{18}O$. It is not likely that the relative humidity variations would affect either ocean fluxes or the isotopic composition of the ocean-to-atmosphere fluxes. However the relative humidity increase could be a result of changes in boundary layer conditions. For example, the increase in relative humidity could be a result of less mixing with dry mid-atmosphere air, which could be related to reductions in wind stress, thus preventing the influence of enrichment from ocean fluxes off the coast of Antarctica to be widespread.

2.5.2 Influences from $\delta^{18}O$ of precipitation

It is likely that variations in relative humidity and the isotopic composition of precipitation are related. In the tropics, there is a well-known statistical relationship between precipitation amount and its isotopic composition (δW_P) such that δW_P values typically decrease as precipitation rates increase (the so-called amount effect [*Dansgaard*, 1964]). Furthermore, studies [*Lu and Zeng*, 2005; *Lu and Takle*, 2010] have found tight positive relationships between precipitation and relative humidity, which are related to changes in water vapor and/or temperatures. Indeed, regional monthly precipitation anomalies were correlated with regional relative humidity anomalies for the Asia-Pacific and Tropical Americas, resulting in r equal to 0.661 and 0.546, respectively. With this reasoning an increase in precipitation during the 1990s would be consistent with a decrease in δW_P for the decade, and thus δW_P would positively correlate with the observed δC_a variations.

Correlations at Bangkok, Izobama, and Darwin were consistent with this (amount effect) relationship during the 1990s. At Bangkok and Darwin, δW_P decreased during the 1990s followed by an increase after 2000, which correlates well with the low frequency variations in observed δC_a, as is reflected in the values of r_L (section 2.4). Also, δC_a anti-correlated with precipitation amount throughout the Asia Pacific, most of the Tropical Americas, and parts of the Congo (Figure 2.5b). These results suggest that observed δW_P variations at these three GNIP stations were not unique to these three stations alone, but likely extended to most tropical land masses. Precipitation increased in the Asia Pacific and Tropical America regions during the 1990s (with the exception of the 1997/1998 El Niño event) (Figure 2.7), and like relative humidity, the negative correlations in these two regions were primarily due to low frequency variations (as is suggested by the values of r, r_L, and r_H in Figure 2.7). Low frequency precipitation increased during the 1990s for the Asia Pacific and Tropical Americas by 2.3mm d^{-1} and 1.3mm d^{-1}, respectively. Using the amount effect "slope" quoted by Bony et al. [2008] of 0.6‰ mm^{-1} d would imply that δW_P in these regions decreased by 1.4‰ and 0.78‰ in the Asia Pacific and Tropical Americas, respectively. However, the low-frequency decrease in δW_P was greater for the stations shown in Figure 2.3. Nonetheless, this increase in precipitation suggests a decrease in δW_P during the mid-1990s, which would likely drive changes in δC_a values of the same sign as those observed.

Stewart [1975] showed through a set of experiments that that vapor near the surface can potentially reach isotopic equilibrium with falling liquid precipitation. Similarly *Lee et al.* [2006] and *Wen et al.* [2010] found positive temporal correlations between measured isotopic

composition of vapor and measured δW_P. As such, variations in the ^{18}O composition of water vapor are assumed to follow that of precipitation.

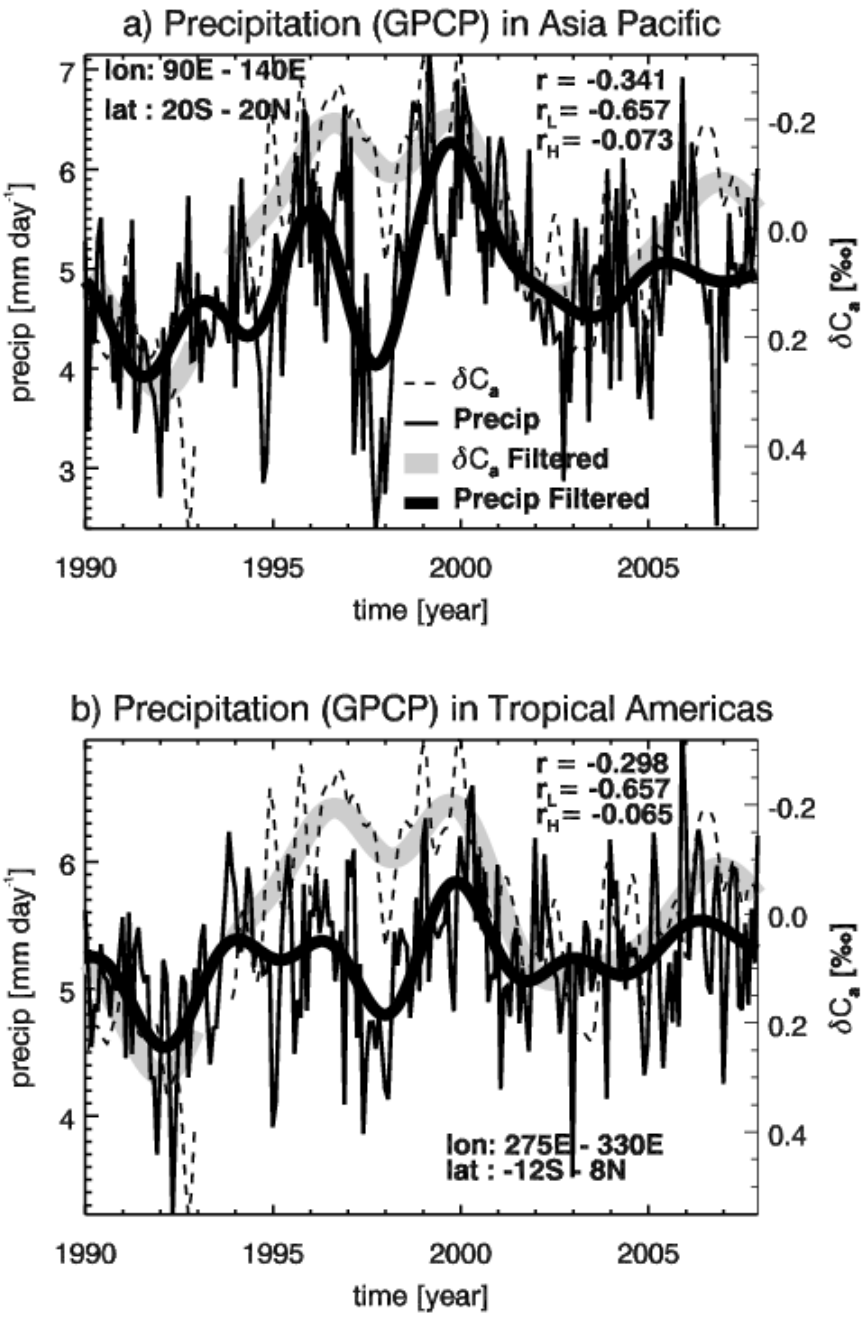

Figure 2.7. Averaged interannual precipitation variations (mm day^{-1}) for the Asian Pacific (a) and Tropical Americas (b). The thick solid line shows the low frequency component of the radiation anomalies. Observed δC_a values from Mauna Loa are also shown (dotted line and thick gray line) and the scale is reversed for better comparison.

At steady state, a change in the ^{18}O composition of precipitation and water vapor will result in the same change to the ^{18}O composition of leaf (via equation 2.6) and soil water [*Farquhar et al.*, 1993], as these are the primary sources of water to land and plants. Calculated from the low frequency curves on Figure 2.3, δW_P decreased from the early 1990s to the end of the decade by 3.1‰ at Bangkok and 3.3‰ at Izobamba. Assuming δW_P decreased in the same regions where relative humidity and precipitation amount was observed to increase (Asia Pacific and Tropical Americas), it was estimated that regional δW_P decreased by 3.2‰ (weighting the two regions by NPP). The ^{18}O composition of soil respired CO_2 (and the leaf-to-atmosphere flux) is primarily determined by δW_S (δW_l) [*Ciais and Mejier*, 1999; *Yakir and Sternberg*, 2000], and δW_S is primarily (but not solely) determined by δW_P [*Welker*, 2000]. As such, it is assumed that the 3.2‰ decrease in δW_P caused the same decrease in the isotopic composition of soil respiration. From section 2.2.1 it was estimated that 26% of the total surface-to-atmosphere global CO_2 flux comes from respiration, and results from CASA suggest that 19% of global respiration comes from these two regions. With these values, equation 2.7 estimates that δC_a decreased by 0.16‰ during the 1990s due to the influence of δW_P on the ^{18}O composition of tropical respiration.

Tropical values of δW_l will also be affected by the decrease in δW_P through the isotopic composition of xylem water in equation 2.6. For reasons stated above, it is assumed that δW_{AV} follows the δW_P variations [*Stewart*, 1975; *Lee et al.*, 2006; *Wen et al.*, 2010]. The 3.2‰ decrease in δW_P and δW_{AV} would have caused a 3.2‰ decrease in δW_l (equation 2.6) during the 1990s, which in turn caused the same change to δF_{la}. Using f_g = 0.52 and f_R = 0.19 as in the previous subsection, the estimated change in δC_a (equation 2.7) would be 0.32‰. Thus, the total

influence from changes to δF_{la} and δF_r due to isotope hydrology variations would be ~0.48‰. This finding is based on a very small dataset (3 viable station records), however, and a better characterization of the processes influencing δC_a requires more thorough measurements of the ^{18}O content of precipitation and vapor, especially near the major tropical rain forests.

2.5.3 Controls on ecosystem fluxes

Nemani et al. [2003] showed regions where water availability, light, and temperature limit assimilation, and found that the limitation by each variable largely depends on latitudinal zones. For instance, assimilation is most dependent on temperature and radiation in the middle and high-latitudes, on water in most arid subtropical regions, and on radiation in the tropical rain forests. In this section, the 1990s variations of these meteorological variables are examined, and the potential influence of the variations on assimilation and subsequently δC_a will be assessed. An estimate of changes to δC_a due to assimilation is used here, accounting for one-way fluxes into and out of the leaves, is:

$$D(\delta C_a) = f_A f_R \left[(\delta C_l + \varepsilon_l - \delta C_a) f_{la} - \varepsilon_l f_{al} \right] \qquad (2.8).$$

where f_A is the fractional change in assimilation, f_{al} is the fraction of global atmosphere-to-leaf flux relative to the total atmosphere-to-surface flux (equal to 0.80 from section 2.2.1), f_{la} is the fraction of global leaf-to-atmosphere flux relative to the total atmosphere-to-surface flux (0.52 from section 2.2.1). Equation (2.8) takes into account kinetic fractionation from diffusion of CO_2 and $CO^{18}O$ into and out of the stomtal pore (ε_l, taken to be –7.4‰ [*Cuntz et al.*, 2003a]). δC_l is calculated from an estimate of zonal mean δW_l [*Hoffmann et al.*, 2004] and an equilibrium fractionation equation (ε_{eq}, [*Brenninkmeier et al.*, 1983]) (i.e., $\delta C_l = \delta W_l + \varepsilon_{eq}$, relative to SMOW). Knowing that other variables might be limiting photosynthesis, equation (2.8) is used

to estimate how a change in one photosynthesis-limiting variable (e.g. temperature) influenced photosynthesis during the 1990s (all other limiting variables assumed constant) to ultimately approximate a change in δC_a.

As shown above, precipitation and relative humidity increased from 1993 to 1997 for the Asian Pacific and Tropical American regions. Leaf fluxes in these regions normally enrich the atmosphere of $CO^{18}O$, and the increase in precipitation (and thus water availability) would cause fluxes to increase and further enrich the atmosphere. However, this assumes that tropical vegetation is water stressed, which without a land surface model or adequate soil moisture data cannot be confirmed unambiguously.

Assimilation depends on the leaf stomatal conductance. *Ball et al*. [1987] proposed a model that estimates stomatal conductance based on its observed relationships with leaf temperature, photon flux density (though indirectly through the assimilation rate), C_C, and leaf surface relative humidity. This model is given by:

$$g_s = mF_A \frac{h_l}{C_C} + g_0 \qquad (2.9)$$

where m is the stomatal sensitivity factor [*Harley and Tenhunen*, 1991] and g_0 is the residual stomatal conductance as assimilation goes to zero. This relationship shows that stomatal conductance depends linearly on relative humidity, and therefore equation (2.9) predicts assimilation would increase as a response to the relative humidity increase discussed in section 2.5.1. Assuming the same 3.3% increase in relatively humidity during the 1990s as in section 2.5.1, and that assimilation increases linearly with relative humidity, f_A in equation (2.8) is estimated to be 0.033. From section 2.2.1 f_{la} and f_{al} are estimated to be 0.52 and 0.84, respectively, and from section 2.5.1 f_R is approximately 0.19. The tropical mean value of δC_a is

estimated to be 0.5‰, which is the mean value at Mauna Loa [*White and Vaughn*, 2009]. To estimate δC_l, the mean value of δW_l within the tropics is assumed to be 7‰ [*Hoffmann et al.*, 2004] and a temperature of 300K would yield δC_l equal to 6.0‰. Given these estimates, equation (2.8) predicts an increase in δC_a of 0.037‰. This is a smaller magnitude change than that associated with either humidity driven changes to the isotopic composition of ecosystem fluxes or changes to the direct water isotope forcing (-0.14‰ and -0.48‰, respectively), though it would slightly oppose the effect of a decrease in leaf water enrichment on δC_a during the 1990s.

This estimate however does not factor in the dependence of stomtal conductance on photosynthesis in equation (2.9). This dependency implies that f_A could be larger than 0.033. However, model results from Chapter 3 reveal that a 3.3% global increase in atmospheric relative humidity caused 2.0% increase in flux-weighted leaf surface relative humidity, which yielded a 2.7% increase in assimilation (and in close agreement with the estimate used here). Similarly, within the tropics *Nemani et al.* [2003] estimated that a 7.4% increase in photosynthesis occurred over an 18-year period that spanned all of the 1990s (1982-1999). Assuming this trend was linear implies a 4.1% increase over the 1990s, which is also consistent with the 3.3% estimate used here. However, their estimated photosynthesis increase may have been influenced by light level changes (discussed below), as many tropical forests are radiation-limited.

The tropical regions with the largest (positive) correlation between δC_a and radiation are those where correlation coefficients between relative humidity and δC_a were high and negative: the Asia Pacific and, to a lesser extent, the Tropical Americas. These radiation correlations are consistent with the relative humidity variations, as any increase in relative humidity will likely

accompany an increase in cloud cover and a decrease in surface solar downwelling radiation [*Still et al.*, 2009], thus providing a consistent check for the opposite signs of the correlations between the variables in these regions. Figure 2.8 shows the time series of average solar downwelling for the Asian-Pacific and tropical American region, along with δC_a variations. Considering the low-pass-filtered time series, both regions show a decrease in solar radiation during the 1990s by 11 Wm^{-2} for the Asia Pacific region and 7.8 Wm^{-2} for the Tropical Americas. For the Asia Pacific and Tropical Americas, early 1990s radiation levels were 240 Wm^{-2} and 233 Wm^{-2}, which corresponds to a 4.6% and 3.3% reduction for the two regions, respectively. The parameterization in the CASA model uses a linear dependence of radiation on NPP [*Potter et al.*, 1999], and results of *Nemani et al.* [2003] suggested that photosynthesis in most tropical regions is light limited. As such, it is assumed here that photosynthesis is light limited and linearly dependent on radiation for these two regions. Thus, f_A values are taken as -0.046 and -0.033 for the Asia Pacific and Tropical Americas (NPP-weighted average of -0.036). Using the same values for f_{la}, f_{al}, f_R, δC_a and δC_l as above (i.e. 0.52, 0.80, 0.19, 0.5‰ and 6.0‰, respectively), and evaluating equation 2.8 results in an estimated -0.040‰ change in δC_a. This small change suggests that interannual δC_a variations are not direct responses to fluxes constrained by solar radiation. This estimate is of opposite sign and similar magnitude to photosynthetic changes induced by the increase in relative humidity. Thus, the overall change to δC_a due to changes to CO_2 fluxes in the Asia Pacific and Tropical Americas is likely relatively small.

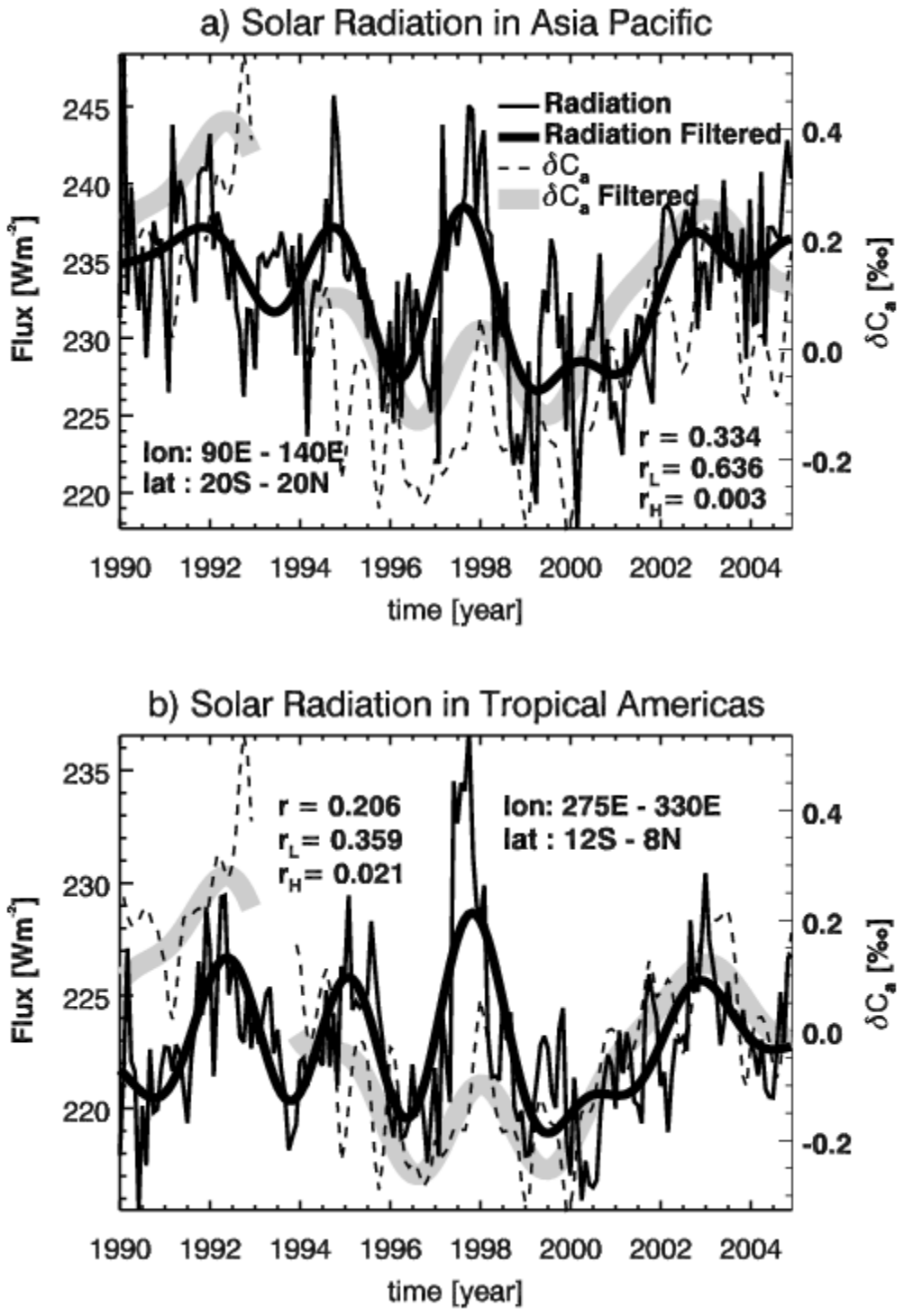

Figure 2.8. Averaged interannual solar radiation variations (thin solid line in units of Wm^{-2}) the Asian Pacific (a) and Tropical Americas (b) The thick solid line shows the low frequency component of the radiation anomalies. Observed δC_a anomalies from Mauna Loa are also shown (dotted line and thick gray line).

These small estimated changes from land ecosystem CO_2 fluxes were largely related to small values of f_A. Considering equation (2.8) it was found that the value of f_A would have to be 0.11 (i.e. an 11% change in assimilation) to cause a 0.1‰ change to δC_a, which would still be smaller than the observed change in δC_a during the 1990s. Results from *Nemani et al.* [2003] suggest that tropical assimilation changes were much less than 11% during the 1990s. Hence, there was very little evidence found here that the 1990s decrease in δC_a was related to assimilation changes in the Tropical Americas and/or the Asia Pacific.

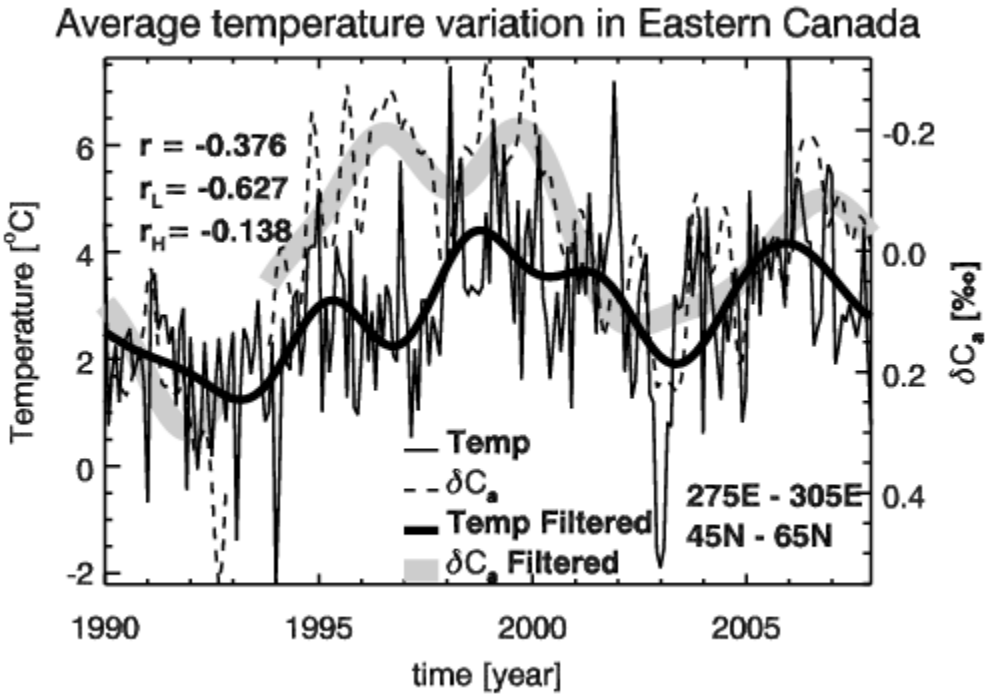

Figure 2.9. Averaged interannual temperature variations (ºC) in Eastern Canada. The thick solid line shows the low frequency component of the temperature anomalies. Observed δC_a anomalies from Mauna Loa are also shown with the scale reversed for an easier comparison (dotted line).

Temperature has been found to constrain assimilation in many regions in the northern middle and high-latitudes [*Nemani et al.*, 2003]. From Figure 2.4, the most robust temperature correlation with δC_a outside of the tropics is in eastern North America, especially within the

Canadian providence of Quebec. Eastern Canada experienced a large increase in temperature during the 1990s of about 2K (Figure 2.9). Because ecosystem fluxes become trivial when ground and vegetation temperatures drop below freezing, the increase in temperatures would cause a longer growing season (Figure 2.10) [*Menzel and Fabian*, 1999; *Kafaki et al.*, 2009] and subsequent increases in annual photosynthesis and respiration [*Baldocchi et al.*, 2001]. Furthermore, *Richardson et al.* [2009] showed how an earlier spring onset increased annual GPP for this region. Taking the annual growing season length as defined by the number of days that average observed daily temperatures are above freezing, and using only years that have at least 364 days of reported observations are considered in the calculation, it is found that in 1992 the average growing season was ~219 days and by 1996 it reaches ~232 days (an increase of 13 days). *Richardson et al.* [2009] found that GPP increased by 7.3 gC m^{-2} for each day increase in growing season length, implying a 94.9 gCm^{-2} increase in GPP for a 13 day increase in the growing season. Furthermore, results from *Hollinger et al.* [2001] revealed that the gross ecosystem production from a nearby forest (northeastern United States) was about 1339 gC m^{-2}, which would suggest that photosynthesis in this eastern North American region increased by 7.2%.

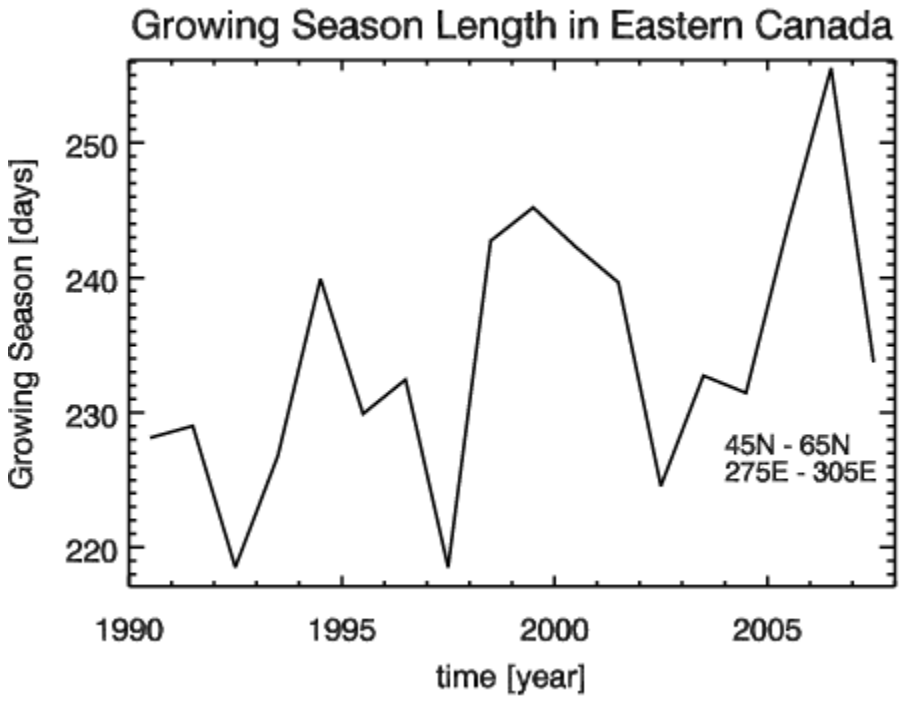

Figure 2.10. Variations in growing season length (number of days) in Eastern Canada.

Results from the CASA model indicate that photosynthesis in this North American region contributes ~1.8% to global photosynthesis (i.e. f_R = 0.018). The mean δC_a, calculated for the NOAA station closest to this region (Argyle, Maine), was -0.5‰. From *Hoffmann et al.* [2004], Northern middle latitude values of δW_l are typically about -5‰, which at 280K would result in a δC_l of -1.3‰. Using the same values for f_{la} and f_{al} as above (0.52 and 0.80, respectively) results in an estimated 0.0022‰ decrease in δC_a. This estimation remained small even when using different values of δC_l (ranging from -15‰ to 15‰ resulting in a $D(\delta C_a)$ range of -0.0072‰ to 0.013‰). Because these estimates included a small value of f_R, another growing season length time series (like the one shown in Figure 2.10) was computed for all of the northern middle and high-latitudes (north of 40ºN). The resulting time series (not shown) did not have any increase in growing season length during the early and mid-1990s (no increase until 1997, well after δC_a had

decreased considerably). These results suggest that it is unlikely that the influence of temperature on ecosystem fluxes caused much of a change to δC_a over the 1990s.

2.6 Conclusion

Using WMO station observations, observed δC_a from Mauna Loa was found to be negatively correlated with relative humidity over a broad geographic range in the Asian Pacific region and parts of the Tropical Americas. Because the two regions were not completely devoid of stations that positively correlated with Mauna Loa δC_a, regional average time series of relative humidity were computed (factoring in all station regardless of correlation sign), and it was found that relative humidity in the two regions do indeed negatively correlate with δC_a in the mean. It was estimated that relative humidity variations contributed ~0.14‰ (0.12‰ from the tropics and 0.021‰ from the middle and high-latitudes) to the observed 0.50‰ decrease in δC_a during the 1990s, and changes in the isotopic composition of precipitation and water vapor may have contributed another ~0.48‰ to the decrease. This overestimation is likely due to the uncertainty in the contribution from δW_P, as there are very few stations that measured this quantity during the 1990s. The results suggest that variations in precipitation, radiation, and temperature were not large enough and do not span a large enough geographic area to alter ecosystem CO_2 fluxes enough to explain the interannual δC_a variations.

The results suggest that about 20% of the 1990s δC_a variations were due to the influence of relative humidity on the isotopic composition of leaf water, and about 80% of the signal was due to isotopic changes to the hydrological cycle (i.e., δW_P and δW_{AV}). The suggestion that interannual δC_a variations are linked to hydrological changes via the isotopic composition of leaf

and soil water is in contrast to other studies that point to land ecosystem flux anomalies as the driver of interannual variability in δC_a [*Gillon and Yakir*, 2001; *Stern et al.*, 2001; *Ishizawa et al.* 2002; *Flanagan* 2005]. Some of these studies suggested land ecosystem flux anomalies as the mechanism for the mid-1990s decrease, though it was not the central focus of those works. The present study provides evidence from the observational record for a potential dominant role of hydrology in influencing δC_a, and for a much smaller role of land ecosystem CO_2 fluxes. Previous modeling studies sought to better understand the spatial structure and seasonality of δC_a [*Farquhar et al.*, 1993; *Ciais et al.*, 1997a, 1997b; *Peylin et al.*, 1999; *Cuntz et al.*, 2003a, 2003b]. To better understand the mechanisms influencing δC_a variations, future modeling work should focus on understanding interannual variations in the observations. If modeling studies can confirm the proposed hydrological mechanisms presented here, then observed δC_a could be used as an indicator of recent hydrological changes. Thus, observations of δC_a may become a powerful integrative tool in the coming decades for monitoring large scale changes in the hydrological cycle should it accelerate under a warming climate, as predicted [*Meehl et al.*, 2007].

Appendix 2A: Notation

C_a	CO_2 mixing ratio in the atmosphere (mole fraction).
C_C	CO_2 mixing ratio at the surface chloroplast within leaf stomata (mole fraction).
F_{al}	CO_2 flux into leaves (PgC y^{-1}).
F_{ao}	CO2 flux from the oceans to the atmosphere (PgC y^{-1})
F_f	CO_2 flux due to fossil fuel consumption (PgC y^{-1}).

F_{la}	CO_2 flux out of leaves (PgC y^{-1}).
F_A	Gross Primary Product minus leaf respiration (PgC y^{-1}).
F_o	net flux of CO_2 from ocean water (PgC y^{-1}).
F_{oa}	CO2 flux into the oceans (PgC y^{-1})
F_r	CO_2 flux from soil respiration (PgC y^{-1}).
F_u	CO_2 flux due to land use changes (PgC y^{-1}).
f_A	fractional change in assimilation
f_{al}	the fraction of global atmosphere-to-leaf flux relative to the total atmosphere to surface flux
f_g	fraction of the global gross flux to the atmosphere from equation (2.7)
f_{la}	the fraction of global leaf-to-atmosphere flux relative to the total surface-to-atmosphere flux
f_R	fraction of the global flux from a particular region that observes the change
g_s	stomatal conductance
g_0	residual stomatal conductance
h_l	relative humidity at leaf surface (range of 0 – 1.0)
M	the stomatal sensitivity factor
M	Mass to concentration conversion factor (2.122 PgC ppm^{-1}).
T	Surface Temperature of either soil or vegetation (K).
Δ_F	Apparent discrimination from fossil fuel consumption and land use changes

Δ_o	Apparent discrimination from net ocean fluxes
Δ_A	Apparent discrimination from assimilation
Δ_r	Apparent discrimination from respiration
δC_a	δ^{18}O-CO_2 value of free air (‰ versus VPDB-CO_2).
δC_l	δ^{18}O-CO_2 value of CO_2 equilibrated with leaf water (‰ versus VPDB-CO_2).
δC_S	δ^{18}O-CO_2 value of CO_2 equilibrated with soil water (‰ versus VPDB-CO_2).
δF_{la}	δ^{18}O-CO_2 value of leaf-to-atmosphere CO_2 flux (‰ versus VPDB-CO_2).
δF_r	δ^{18}O-CO_2 value of soil respiration (‰ versus VPDB-CO_2).
δW_{AV}	δ^{18}O value of atmospheric water vapor (‰ versus VSMOW-H_2O).
δW_{CV}	δ^{18}O value of canopy water vapor (‰ versus VSMOW-H_2O).
δW_l	δ^{18}O value of leaf water (‰ versus VSMOW-H_2O).
$\delta W_{l\text{-}CG}$	δ^{18}O value of leaf water (‰ versus VSMOW-H_2O) using the Craig-Gordon estimation.
δW_P	δ^{18}O value of precipitation (‰ versus VSMOW-H_2O).
δW_S	δ^{18}O value of root-weighted soil water (‰ versus VSMOW-H_2O).
ε_{eq}	temperature dependent CO_2 equilibration factor (‰ versus VSMOW)
ε_k	$H_2{}^{18}O$ kinetic fractionation factor for molecular diffusion (‰ versus VSMOW-H_2O)
ε_l	Effective kinetic fractionation factor for $CO^{18}O$ diffusion in and out of the stomata (‰ versus VPDB-CO_2)

ε_{LV} the temperature dependent equilibrium fractionation of $H_2{}^{18}O$ during the liquid-vapor phase transition (‰ versus VSMOW-H_2O)

ε_S Effective kinetic fractionation factor for $CO^{18}O$ diffusion out of soil (‰ versus VPDB-CO_2)

T residence time of oxygen in atmospheric CO_2

Appendix 2B: Derivation of equation 2.7

At steady-state δC_a equation 2.3 becomes:

$$C_a M \frac{d(\delta C_a)}{dt} = \sum_i (F_i \Delta_i) = 0 \qquad (2B.1)$$

where subscripts i refers to a particular component of the carbon cycle (e.g., respiration). In equation (2B.1), δC_a refers to the global mean, Δ_i is the flux-weighted global mean, and F_i is the global total:

$$F_i = \sum_j^{Globe} F_{i,j} \qquad (2B.2)$$

where subscript j accounts for fluxes in particular regions. In general, apparent discrimination is defined as:

$$\Delta_i = (\delta F_i - \delta C_a) \qquad (2B.3).$$

Expanding the summation of equation (2B.1) results in:

$$\sum_i (F_i \Delta_i) = F_1(\delta F_1 - \delta C_a) + F_2(\delta F_2 - \delta C_a) + ... + ... = 0 \qquad (2B.4).$$

Solving for δC_a gives:

$$\delta C_a = \delta F_1 \frac{F_1}{\sum_i F_i} + \delta F_2 \frac{F_2}{\sum_i F_i} + \ldots = \sum_i \delta F_i f_i \qquad \text{(2B.5)},$$

where f_i is defined as the fraction of a given CO_2 surface flux relative to the total surface-to-atmosphere flux. (F_{sa}). From equation (2B.5), a small finite change in the global mean δC_a, $D(\delta C_a)$, could be brought upon by a small (linear) change to the isotopic composition of any flux, $D(\delta F_i)$, or a change to the f_i, values $D(f_i)$:

$$D(\delta C_a) = D(\delta F_i) f_i + \delta F_i D(f_i) \qquad . \qquad \text{(2B.6)}.$$

Because the total surface-to-atmosphere flux is large relative to the individual components, it is assumed that the values of $D(f_i)$ are small. Considering the summation of equation (2B.2), equation (2B.6) would then be written as:

$$D(\delta C_a) = \sum_j D(\delta F_{i,j}) \frac{F_{i,j}}{F_{sa}} \qquad \text{(2B.7)}.$$

The summation in equation (2B.7) need not be global. If the summation were evaluated over a particular region (R), then the equation becomes:

$$D(\delta C_a) = D(\delta F_{i,R}) \frac{F_{i,R}}{F_{sa}} = D(\delta F_{i,R}) \frac{F_{i,R}}{F_i} \frac{F_i}{F_{sa}} \qquad \text{(2B.8)}.$$

Defining $f_R = F_{i,R}/F_i$, then equation (2B.8) can be rewritten as:

$$D(\delta C_a) = D(\delta F_{i,R}) f_i f_R \qquad \text{(2B.9)}.$$

Chapter 3

Modelling the Response of the Terrestrial Biosphere and $\delta^{18}O$ of Atmospheric CO_2 to Changes in Atmospheric Conditions

3.1 Introduction

Land use changes and rising levels of industrial activity have increased the atmospheric CO_2 concentration over the past several decades [*Denman et al.*, 2007]. Nevertheless, terrestrial photosynthesis and respiration still play a dominant role in the seasonal cycling of CO_2, annually exchanging 20% of the atmospheric stock [*Sarmiento and Gruber* 2002]. A number of approaches have been developed to attribute observed atmospheric CO_2 concentrations to its various sources, including inversions [*Guerney et al.*, 2003, 2004], bottom up approaches [*Denman et al.*, 2007], and isotopic tracers (^{13}C, ^{14}C, and ^{18}O [*Quay et al.*, 1992; *Fung et al.*, 1997; *Peylin et al.*, 1999; *Ogée et al.*, 2004; *Naegler et al.*, 2007; *Rayner et al.*, 2008]). In this chapter I focus on the sensitivity of the ^{18}O composition of atmospheric CO_2 (δC_a) to changes in climate forcing. Since δC_a is believed to be sensitive to respiratory and photosynthetic fluxes and the ^{18}O content of water pools in the soil and plants [*Francey and Tans*, 1987; *Farquhar et al.*, 1993], it is a potentially valuable atmospheric tracer of global interactions between the hydrologic and carbon cycles.

Farquhar et al. [1993] concluded through a global model analysis that the land ecosystem fluxes largely impact the spatial structure of δC_a. Studies using more complex models have concluded that both the north-south gradient and the seasonal cycle in δC_a are almost entirely determined by land ecosystem fluxes and atmospheric transport [*Ciais et al.*, 1997a, 1997b; *Peylin et al.*, 1999; *Cuntz et al.*, 2003a, 2003b]. However, *Still et al.* [2009] showed

through observations and an isotopic land model the possible linkage between δC_a and the hydrological cycle (such as humidity and cloud cover variations). Similarly, Chapter 2 presented empirical evidence of a connection between interannual δC_a variations and changes within the hydrological cycle. In this chapter I apply a similar (global) version of the model used by *Still et al.* [2009] (and described in detail by *Riley et al.* [2002]) to evaluate the sensitivity of δC_a to meteorological changes. Large variations in δC_a were observed during the 1990s (Figure 1.1), though the scope of this chapter is to better understand how δC_a responds to changes in climatic forcing and not on modeling the interannual variations (which is addressed in Chapter 4).

In Chapter 1, the observed interannual δC_a variations were presented, which showed a consistent decrease in δC_a during the mid-1990s, followed by an increase after 1999 and then another decrease after 2004. The causes of these variations have not been determined, though some studies [*Gillon and Yakir*, 2001; *Stern et al.*, 2001; *Ishizawa et al.* 2002; *Flanagan* 2005] have suggested that the variations are due to changes in ecosystem CO_2 fluxes. Examining the δC_a budget equation revealed possible influences from assimilation (F_A) and respiration (F_R) and the isotopic composition of leaf water (δW_l) and soil water (δW_S). The two ecosystem fluxes are primarily dependent on solar radiation, temperature and water availability (i.e. precipitation and relative humidity). δW_S is set by the isotopic composition of precipitation (δW_P), which can be further enriched in ^{18}O via soil evaporation.

The *Craig and Gordon* [1965] model adjusted for leaf water can be examined to understand the influences on δW_l:

$$\delta W_{l-CG} = \varepsilon_{LV} + (1 - h_l)(\delta W_X - \varepsilon_k) + h_l \delta W_{CV} \qquad (3.1).$$

In equation (3.1), ε_{LV} is the temperature dependent equilibrium fractionation of $H_2{}^{18}O$ during the liquid-vapor phase transition, ε_k is the kinetic fractionation of $H_2{}^{18}O$ during the diffusion of vapor across the stomata and leaf boundary layer, h_l is relative humidity at the leaf surface, δW_X is the isotopic composition of the xylem water, and δW_{CV} is the isotopic composition of the canopy vapor (a complete list of the variable notation is provided in Appendix 3.A). The simple mass balance equation shows that the isotopic composition of leaf water (δW_l) is related to that of stem/xylem water (δW_X) and canopy vapor (δW_{CV}), the relative humidity at the leaf surface, and temperature (through equilibrium fractionation). Other factors can influence δW_l, including the Péclet effect [*Farquhar and Lloyd* 1993] and leaf water levels. δW_X reflects a convolution of the vertical profiles of soil water ^{18}O and root water uptake, thus δW_X is determined by δW_S (which is set by δW_P).

In Chapter 2 I looked for empirical evidence of possible influences by the variables mentioned above on δC_a. It was found that the interannual δC_a variations were negatively correlated with observed relative humidity in certain tropical regions. Positive correlations were found between δC_a and δW_P in the same tropical regions, though δW_P data was limited. By examining the magnitude of the relative humidity and δW_P variations, it was estimated that the mid-1990s decrease in δC_a was primarily driven by decreases in δW_P within the tropics, with a smaller contribution from an increase in relative humidity in the same tropical regions.

Motivated by those estimations, the work of this chapter involves the construction of a global model to simulate CO_2 and $CO^{18}O$ (and thus δC_a) and perform experiments to explore how meteorological changes can affect δC_a. Land simulations were performed using an isotope version of the National Center for Atmospheric Research (NCAR) Land Surface Model

(ISOLSM) [*Bonan*, 1996; *Riley et al.*, 2002, 2003]. The simulations used predicted surface to atmosphere fluxes from ISOLSM as input to the NCAR Community Atmosphere Model (CAM) to estimate δC_a. This model configuration is intermediate in approach between the original off-line global simulations of *Farquhar et al.* [1993], *Ciais et al.* [1997a and 1997b] and *Peylin et al.* [1999] and the interactive model of *Cuntz et al.* [2002a and 2003b]. I first present a comparison between a control simulation and observed δC_a variations to demonstrate model performance. I then apply this model framework to determine how changes in humidity, temperature, light levels, and the δ^{18}O value of precipitation and water vapor can affect δC_a via changes in gross CO_2 fluxes and the isotopic composition of leaf and soil water.

3.2 Model and Experiments

3.2.1 The land surface model (ISOLSM)

LSM simulates the exchanges of energy, momentum, H_2O, and CO_2 between the atmosphere and the terrestrial biosphere. *Riley et al.* [2002] developed integrated modules within LSM1.0 (together called ISOLSM) to compute the exchanges of $C^{18}O$ and $H_2{}^{18}O$ to and from the terrestrial biosphere. The model calculates canopy water vapor, vertically resolved soil water, and shaded and sunlit leaf water, as well as the ^{18}O isotopic composition of each pool. ISOLSM accounts for ^{18}O in water and carbon exchanges by including various fractionation processes. The leaf water model in ISOLSM employs a time-dependent mass balance that includes a transpiration-dependent leaf turnover time-scale to calculate δW_l [*Dongman*, 1974; *Still et al.*, 2009]. The model uses an advective transport model, non-fractionating root water uptake estimate, and surface boundary layer resistance to predict the soil water isotopic ratio. The $\delta^{18}O$ value of soil gas CO_2 is predicted considering gaseous diffusion, surface boundary

layer resistance, and temperature-dependent equilibration between gaseous CO_2 and water [*Brenninkmeijer et al.*, 1983]:

$$\alpha_{eq}(T_s) = 1 + \left(\frac{17604}{T_s} - 17.93 \right) \times 10^{-3} \qquad (3.2a)$$

$$\varepsilon_{eq}(T_s) = \frac{17604}{T_s} - 17.93 \qquad (3.2b)$$

where T_s (K) is surface temperature (i.e., ground or leaf temperature). Kinetic isotopic fractionation associated with CO_2 diffusion through the leaf boundary layer is used to calculate isotopic leaf fluxes. While the details of the fractionation schemes for H_2O and CO_2 are given in detail by *Riley et al.* [2002], I note here that kinetic effects account for diffusion during transport of gas phase CO_2 through the soil and during transport from the chloroplast during leaf respiration through the leaf boundary layer. Similarly, the isotopic water vapor kinetic fractionations are dependent on near-surface turbulent intensity as well as the ratio of $H_2{}^{18}O$ diffusivity to H_2O diffusivity [*Mathieu and Bariac*, 1996].

The model computes gross CO_2 leaf fluxes from the atmosphere-to-leaf, F_{al} (mol m^{-2} s^{-1}), and from leaf-to-atmosphere, F_{la} as [*Ciais et al.*, 1997a]:

$$F_{al} = \left(\frac{C_a}{C_a - C_i} \right) F_A \qquad (3.3)$$

$$F_{la} = \left(\frac{C_i}{C_a - C_i} \right) F_A \qquad (3.4)$$

where C_i is the CO_2 concentration inside the stomatal pores. The $CO^{18}O$ fluxes from leaves are calculated as:

$${}^{18}F_{la} = \alpha_l R_l F_{la} \qquad (3.5)$$

where α_l is the diffusive fractionation factor across the laminar leaf boundary layer and through the stomata and R_l is the $CO^{18}O$ to CO_2 ratio within the leaves. The non-leaf CO_2 and $CO^{18}O$ respiration fluxes (F_r and ${}^{18}F_r$, respectively) are calculated as the sum of microbial, growth, and root and stem maintenance respiration.

ISOLSM simulations are forced with two sets of meteorological data: radiation, precipitation, height, and sea-level and surface pressure from the reanalysis of *Qian et al.* [2006]; and temperature, relative humidity, and wind speed from the Global Summaries of the Day, which was obtained through the World Meteorological Organization and the National Climatic Data Center Climate Services Branch. A method similar to *Cressman* [1959] objective analysis was used to interpolate the station observations onto the model grid, and a detailed description of this dataset is given in Appendix 3.B. The $\delta^{18}O$ value of precipitation (δW_P) is prescribed from a dataset that is discussed in Chapter 5, which was constructed using a regression/Fourier Transform approach and constrained by global observations [*Isotope Hydrology Section*, 2006]. The isotopic composition of atmospheric vapor (δW_{AV}) is prescribed using calculated precipitation and vapor offsets modeled by the Melbourne University General Circulation Model [*Noone and Simmonds*, 2002].

3.2.2 Ocean and Anthropogenic Fluxes

The global distribution of net CO_2 fluxes between the ocean and the marine atmosphere, F_o (mol m^{-2} s^{-1}), and sea-air CO_2 partial pressures, p_o and p_a (Pa), were taken from a dataset produced by the Takahashi CO_2 Group [*Takahashi et al.*, 2002; *Gurney et al.*, 2002]. However, the two one-way CO_2 fluxes (atmosphere-to-ocean (F_{ao}) and ocean-to-atmosphere (F_{oa})) must be considered independently (like the leaf fluxes), as their isotopic compositions differ. To calculate

the two one-way fluxes (equations 3.7 and 3.8), the air-sea gas exchange coefficients, K_{ex} must first be calculated (equation 3.6):

$$F_o = K_{ex}\left(p_o - p_a\right) \tag{3.6}$$

$$F_{ao} = K_{ex} p_a \tag{3.7}$$

$$F_{oa} = K_{ex} p_o \tag{3.8}$$

The ocean-to-atmosphere $CO^{18}O$ flux (mol m^{-2} s^{-1}), ${}^{18}F_{oa}$, is given by

$${}^{18}F_{oa} = \alpha_w R_o F_{oa} \tag{3.9}$$

where R_o is the $^{18}O/^{16}O$ ratio of dissolved CO_2 and α_w is the fractionation associated with CO_2 crossing the air-sea interface, using the value *Vogel et al.* [1970] measured at 0ºC of +0.8‰ ($\alpha_w = 1 + \varepsilon_w / 1000$, $\varepsilon_w = +0.8‰$). The ratio R_o is calculated as

$$R_o = \alpha_{eq}(T_s) R_{ow} \tag{3.10}$$

where α_{eq} is the temperature dependent equilibrium fractionation factor, T_s is sea surface temperature, and R_{ow} is the $^{18}O/^{16}O$ ratio of ocean surface water. Using reconstructed sea-surface temperatures, T_s, from the NOAA_ERSST_V3 (data provided by the NOAA/OAR/ESRL PSD; *Smith et al.* [2007]), the value of $\alpha_{eq}(T_s)$ was calculated using equation (3.2a). The values of R_{ow} were obtained via data generated by *LeGrande and Schmidt* [2006].

Emissions from fossil fuel combustion, F_f, were acquired from the dataset produced by *Andres et al.* [1996]. Also included in the model are fluxes from biomass burning F_f, using the Global Fire Emissions Database version 2 (GFEDv2) [*Van der Werf*, 2006]. Both of the anthropogenic fluxes are assumed to not fractionate and take on the isotopic ratio of atmospheric oxygen, R_{O2} (where δ_{O2} = -17‰). Thus, the $CO^{18}O$ fluxes from both fossil fuel emissions and biomass burning are calculated as:

$$^{18}F_f = R_{O2}F_f \tag{3.11}$$

$$^{18}F_b = R_{O2}F_b \tag{3.12}$$

3.2.3 Atmospheric transport model (CAM)

Atmospheric concentrations of CO_2 and $CO^{18}O$ are simulated using the NCAR Community Atmosphere Model, CAM [*Collins et al.*, 2006]. Taking into account the processes of the terrestrial biosphere, the ocean, and anthropogenic sources, the temporal changes of CO_2 and $CO^{18}O$ can be written as:

$$\frac{dC_a}{dt} = \frac{1}{M_a}\left[F_{la} + F_r + F_{oa} + F_f + F_b - (F_{al} + F_{ao})\right] \tag{3.13}$$

$$\frac{d^{18}C_a}{dt} = \frac{1}{M_a}\left[F_{la}^{18} + F_r^{18} + F_{oa}^{18} + F_f^{18} + F_b^{18} - (\alpha_l F_{al} + \alpha_w F_{ao})R_a\right] \tag{3.14}$$

where R_a is the instantaneous ratio of atmospheric $CO^{18}O$ to CO_2 ($^{18}C_a/C_a$) and M_a is a conversion factor (with units of moles of air m^{-2}). While all fluxes in equation (3.13) are computed by either ISOLSM or calculated from datasets, the atmosphere-to-surface fluxes of $CO^{18}O$, and thus R_a, are found by integrating equation (3.14) with the atmospheric transport model CAM. Specifically, only by allowing the atmosphere to interact with the surface fluxes will a steady state δC_a be found (i.e., simulated local annual mean δC_a stays relatively constant). Moreover, to resolve the 3-dimensional δC_a field, account needs to be made for the advection tied to the material evolution on the left hand side, which again is a task for which CAM is well suited.

ISOLSM simulations ran twice through the 1979-2004 period and the twelve (January through December) monthly mean fluxes of CO_2 and $CO^{18}O$ were computed using the last

twenty six years of the simulation (i.e., the 2nd cycle through the 1979-2004 period). To ensure a realistic rise in atmospheric CO_2 over the long-term, a correction was used to adjust the (non-leaf) respiratory fluxes so that the surface ecosystem CO_2 fluxes were close to being balanced for every grid point in a manner similar to *Denning et al.* [1996] and *Riley et al.* [2005] (i.e., a method similar to the so-called "R*" approach). Global respiration was slightly adjusted even further such that simulated CO_2 concentrations gradually rose at a rate consistent with observations during the 1990s (3.2 GtC yr^{-1} [*Denman et al.*, 2007] implying a slight ecosystem uptake of CO_2. These fluxes along with the fluxes described in section 3.2.2 were then used as input for CAM. CAM simulations ran for 30-years with the last 10 years used for the analysis.

3.2.4 Experiments

Eleven experiments were performed to examine the influence of atmospheric relative humidity, light levels, temperature, and the $\delta^{18}O$ value of precipitation and water vapor on δC_a. Table 3.1 gives a brief explanation of each experiment along with the experiment name, which is used hereafter. The magnitude of some of the perturbations for these sensitivity experiments were based on the observed variations discussed in Chapter 2 (e.g., a 3.3% increase in relative humidity in the Asia Pacific and Tropical Americas). The sensitivity of δW_l, δW_S, and δC_a to relative humidity was investigated by performing experiments that increased the prescribed relative humidity at each grid point by 3.3% units globally (RH) and only within the tropics (equatorward of 20°N and 20°S, RHTROP). To examine the influence of isotope hydrology on δC_a, a global 3.2‰ reduction was applied to the prescribed $\delta^{18}O$ value of precipitation (PREC). To examine how much of the response was from the tropics another experiment was performed in which the reduction is only applied within the tropics (PRECTROP). The same specifications

were applied to the $\delta^{18}O$ values of water vapor (WV and WVTROP) and to both $\delta^{18}O$ values of precipitation and water vapor (PRECWV and PREC/WVTROP) to further deduce the role of hydrological isotopic forcing on δC_a. To estimate the influence of light levels on δC_a, 7.5% of the prescribed direct radiation is repartitioned to diffuse radiation (a 15% total change), while lowering the total radiation by 4% (denoted LIGHT). The sizes of these anomalies were chosen to be comparable to those following the eruption of Mount Pinatubo, as implied by *Gu et al.* [2003]. The eruption of Mount Pinatubo also affected global air temperatures, and the role of temperature changes on δC_a is evaluated through an experiment in which global temperatures are increased by 1K (TEMP). In the TEMP experiment relative humidity is unchanged; thus there will also be a slight increase in specific humidity. To evaluate how a change to the assimilation/respiration partitioning may influence δC_a, an experiment was conducted where photosynthetic leaf fluxes were increased globally by 3.6% (offline from both ISOLSM and CAM) without any change to non-leaf respiration (ASSIM). This size of the increase is reflective of the increase in radiation discussed in chapter 2. Another experiment was conducted that increased non-leaf respiration globally by 3.6% without any change to photosynthetic leaf fluxes (RESP).

Table 3.1. List of the experiment names with a brief description.

Experiment Name	Description
RH	Global relative humidity is increased by 3.3%.
RHTROP	Relative humidity is increased by 3.3% between 25°S and 25°N
PREC	Reduced the prescribed $\delta^{18}O$ of precipitation by 3.2‰ globally
PRECTROP	Reduced the prescribed $\delta^{18}O$ of precipitation by 3.2‰ between 25°S and 25°N
WV	Reduced the prescribed $\delta^{18}O$ of atmospheric water vapor by 3.2‰ globally
WVTROP	Reduced the prescribed $\delta^{18}O$ of atmospheric water vapor by 3.2‰ between 25°S and 25°N
PRECWV	Reduced the prescribed $\delta^{18}O$ of precipitation and atmospheric water vapor by 3.2‰ globally
PRECWVTROP	Reduced the prescribed $\delta^{18}O$ of precipitation and atmospheric water vapor by 3.2‰ between 25°S and 25°N
LIGHT	Repartitioning 7.5% of the direct radiation to diffuse and a 4% reduction in global downwelling solar radiation
TEMP	Global temperatures are increased by 1K
ASSIM	Global 3.6% increase in F_{la} and F_{al} without any change to F_r
RESP	Global 3.6% increase in F_r without any change to leaf fluxes

3.3 Simulated CO_2 and $CO^{18}O$

To facilitate later discussion I first present results from an unperturbed control simulation. The global annual average quasi-steady state δC_a at the lowest level in the model (about 50 meters above the surface) was found to be 0.5‰ (V-PDB), which agrees well with the observed value of about 0.9‰ (e.g., NOAA/GMD data presented by *Cuntz et al.*, 2003b). Figure 3.1a shows observed and modeled zonal mean δC_a at the ground level as well as the contributions from the five components of the budget equation (1.1). Recognizing that the model results were slightly lower than the observed values, δC_a in Figure 3.1 was normalized such that the South Pole value is the observed 1.20‰ as is conventional in previous model studies (e.g., *Ciais et al.* [1997b]; *Cuntz et al.* [2002b]). The model simulated a north-south δC_a gradient that agrees well with observations, as is reflected in the correlation coefficient in Figure 3.1a (correlating 20 observed annual means with simulated values from the nearest grid-cell). There is no significant change to the correlation coefficient when comparing the observations with the 4^{th} model level, though the simulated gradient was not as steep at this level (Figure 3.1b). These correlations suggest that the model is reasonably capturing the spatial variations of δC_a.

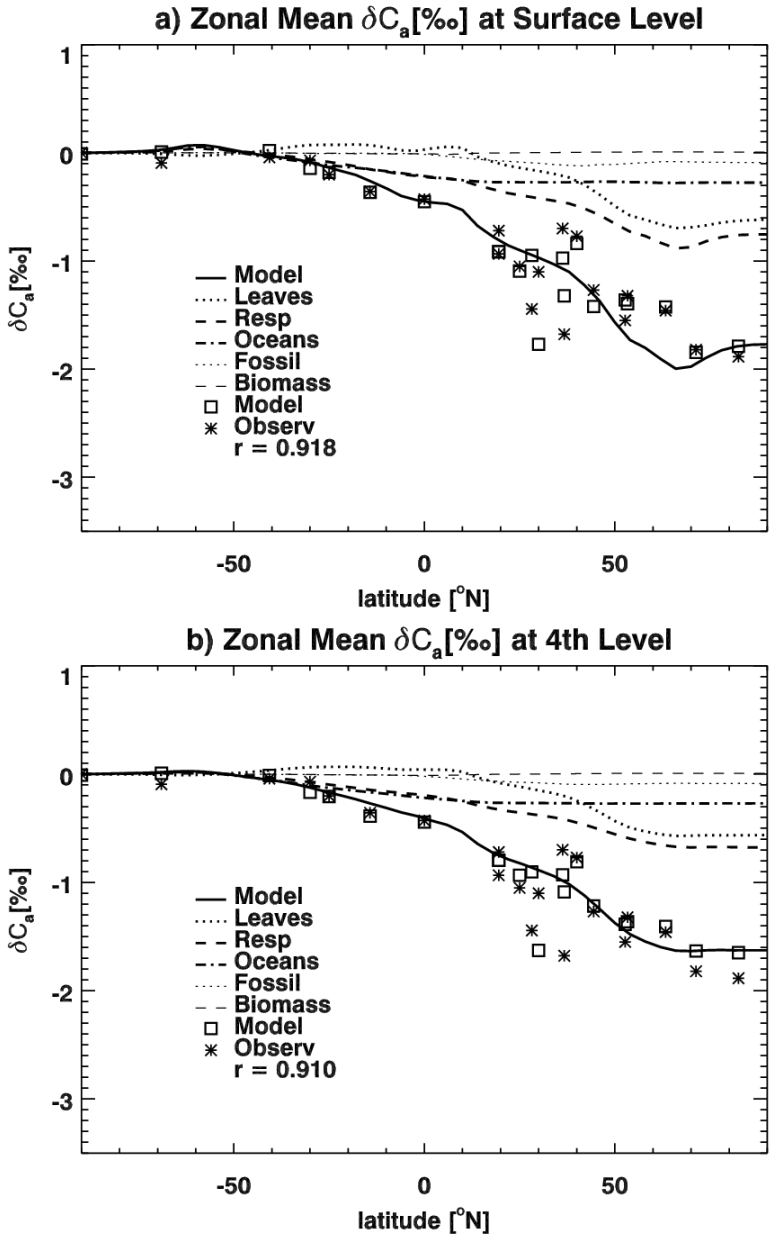

Figure 3.1. Simulated north-south gradient in δC_a (‰) (solid line) and the contributions from leaves (dark dotted), respiration (dark dashed), oceans (dash dot), fossil fuel consumption (light dotted), and biomass burning (light dashed). Asterisks represent an observed mean value, and the squares are from the closest grid-cell to each observation. Panel (a) shows the model's surface layer and the bottom panel shows the model's 4th atmospheric layer.

Similar to the results of *Ciais et al.* [1997b] and dissimilar to those of *Cuntz et al.* [2002b], the model predictions implied very small contributions to the gradient from biomass burning and fossil fuel consumption, and only about a 0.2‰ global contribution from ocean fluxes. Respiration contributed the most to the gradient, while leaf-to-atmosphere fluxes caused a stronger equator-pole gradient (i.e., not necessarily a north-south gradient). This contribution from the leaves was much like the findings of *Cuntz et al.* [2002b] and contrasts with the model results of *Ciais et al.* [1997b], whose leaf contribution acted to reduce the gradient.

In agreement with others studies, the highest annual mean surface CO_2 concentrations for the control simulation were in the northern hemisphere, specifically over the northeastern United States and Eastern Europe (Figure 3.2a) and consistent with a seasonal "rectifier effect" [*Denning et al,* 1996] (Figure 3.2b). These regions also had large seasonal amplitudes (Figure 3.2b), with high CO_2 concentrations during the northern hemisphere winter when there was little photosynthetic activity. Yet, the largest seasonal amplitudes were over western tropical Africa, primarily due to large seasonal variations in biomass burning.

The ^{18}O composition of CO_2 (Figure 3.2c) was lowest over middle to high-latitude forests where the $\delta^{18}O$ value of precipitation is relatively depleted and thus carbon fluxes deplete δC_a. These areas include the boreal forests of North America, Asia, and Eastern Europe. The simulations of *Ciais et al.* [1997b] showed high levels of depletion in the Northern Hemisphere's boreal forests, as well as in the Amazon, the Congo, and Southeast Asia, which were attributed to ecosystem fluxes; however, the simulations of *Cuntz et al.* [2003b] had slightly depleted values over the Amazon, and to a lesser extent Southeast Asia with enriched values over the Congo. The simulated tropical δC_a shown here (Figure 3.2c) agree more with the results of *Cuntz et al.*

[2003b] with slight depletion over the Amazon and Southeast Asia and enrichment over the Congo.

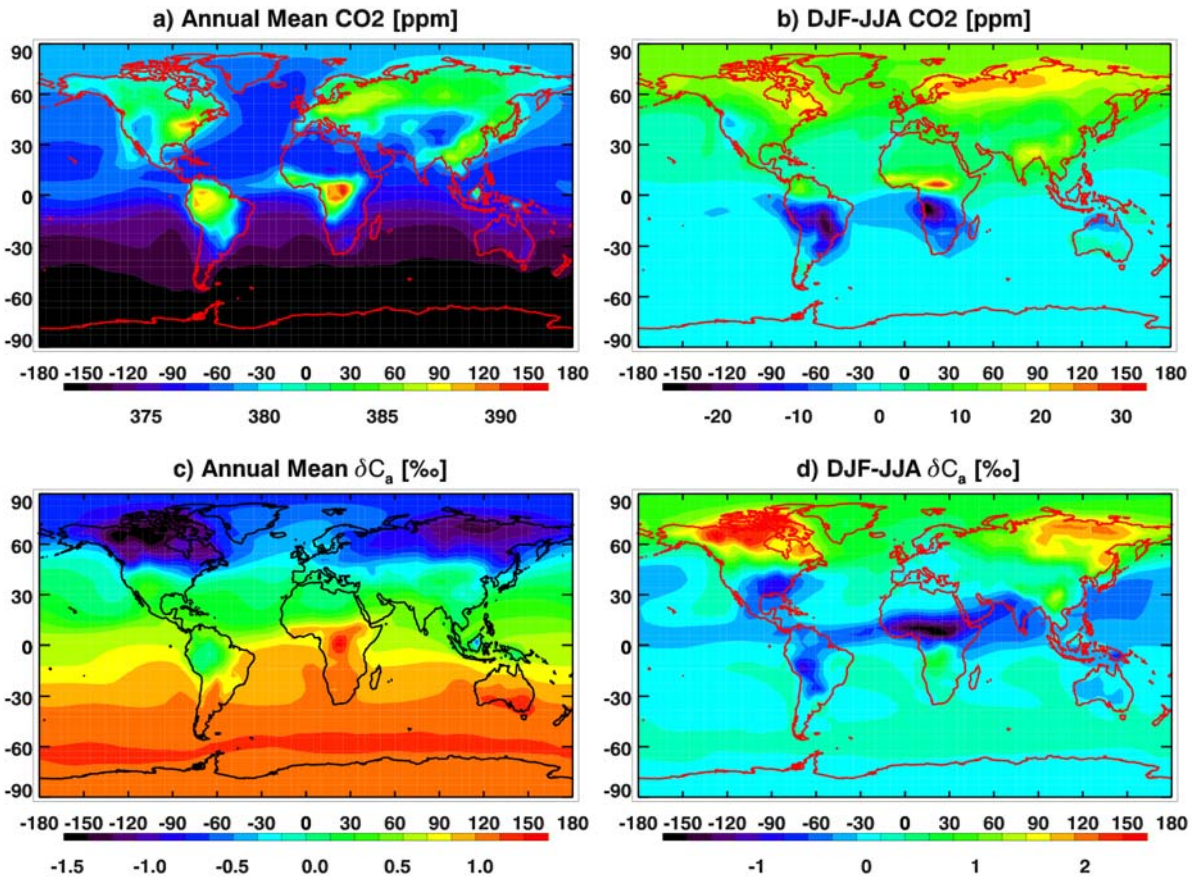

Figure 3.2. Simulated annual mean values of (a) CO_2 and (c) δC_a in units of ppm and ‰, respectively. The seasonal amplitude (December, January, February minus June, July, August) of CO_2 (b) and δC_a (d) are also shown.

The global δC_a seasonal amplitude (Figure 3.2d) was similar to that of CO_2 (Figure 3.2b) with large amplitudes over tropical Africa and the northern boreal forests. In Africa, predicted minimums in seasonal cycle of δC_a were displaced north of those for CO_2. Also, the minimum in the δC_a seasonal cycle predicted in the southern U.S. also did not correspond to a minimum in the CO_2 seasonal cycle. The model also predicted the largest δC_a seasonal amplitude in the high-

latitudes (especially in Canada. and Russia), which was due to large seasonal variations in ^{18}O depleting ecosystem CO_2 fluxes. For instance, when ecosystem fluxes were highest over North America during June, July, and August, δC_a decreased locally because local ecosystem fluxes acted to deplete the atmosphere in $CO^{18}O$ at middle and high latitudes. During winter months, ecosystem leaf fluxes are small, which allows δC_a to slowly approach the global mean of δC_a via large-scale transport, thus causing large seasonal amplitudes.

I compared the simulated seasonal cycle of CO_2 and δC_a to observed cycles at twenty sites where there are many observations for the 1990-2007 period (Figures 3.3 and 3.4). Results from the lowest, 4th and 7th model levels are shown in the figures to demonstrate the simulated seasonal cycles near the surface, the top of the boundary layer and within the free troposphere, respectively. Model results away from the surface are shown because many of the observing stations collect air samples when meteorological conditions favor a free atmosphere measurement (thus, limiting the influence of local fluxes). To quantify the model's performance, correlation coefficients were calculated for the observed monthly means and the modeled means at the model's surface, 4th, and 7th levels (corresponding to r_1, r_4, and r_7, respectively). These values are shown in Figures 3.3. and 3.4 for each station. Also, the seasonal range (maximum minus minimum) was computed at each station for both the observed and modeled values, and model-observation differences are given in Tables 3.2 and 3.3. Similarly, the phase of the first harmonic (defined as the seasonal maximum) of each seasonal time series was computed using Fourier transforms, and the first harmonic phase differences between model and observations are shown in Tables 3.2 and 3.3. For the Northern Hemisphere stations, observed values mostly fell on the curves derived from modeled surface values or in between the surface and the free atmosphere, thus accurately capturing the seasonal amplitude and phase of atmospheric CO_2. For

example, at Cape Kumakahi (Figure 3.3n) the seasonal cycle is well-captured at all three layers, as is reflected in the correlation coefficients and the low model-observation differences in Table 3.2. On the other hand, at Niwot Ridge (Figure 3.3g) simulated amplitudes and phases match up better with observations at the 4th and 7th levels (reflected in the values of r_1, r_4, and r_7 and the values in Table 3.2), as this station is at an elevation of 3475 m and the model does not resolve topography well for this region. One model weakness found here is inaccurate simulation of CO_2 amplitudes in the Southern Hemisphere (Figure 3.3p-3.3t). An additional model simulation where all ocean fluxes are set to zero revealed that this discrepancy was due to inaccurate ocean fluxes and not a problem with calculated land fluxes from ISOLSM.

Table 3.2. Model-observation differences in CO_2 seasonal cycles.

	[1]Amplitude difference			[1]Phase difference		
	Surface	4th level	7th level	Surface	4th level	7th level
Alert	9.34 ppm	7.08 ppm	0.628 ppm	-7.21 days	-3.93 days	1.34 days
Barrow	9.27	5.69	-1.06	-5.65	0.370	7.14
Storhofdi	4.41	3.04	-2.33	0.0518	2.31	10.7
Mace Head	4.67	3.53	-1.54	3.74	5.14	12.4
Shemya Island	1.03	-0.293	-4.74	11.0	13.2	14.6
Ulaan Uul	1.37	-0.648	-4.92	10.1	11.0	24.4
Niwot Ridge	-2.81	-1.59	0.00870	9.01	7.89	25.4
Tae-ahn	-1.44	-1.72	-5.38	5.79	2.50	19.8
Mt. Waliguan	2.61	1.82	-0.0562	8.37	4.71	14.3
Pacific 30N	1.16	1.05	-1.47	4.73	13.4	22.1
Midway Island	2.15	2.04	0.461	11.4	10.1	10.2
Pacific 25N	1.51	1.26	-1.16	-2.61	6.11	14.8
Mauna Loa	3.46	3.61	1.51	-17.5	-15.4	10.3
Cape Kumukahi	1.65	1.80	-0.299	-3.50	-1.37	3.72
Pacific 0N	1.21	0.721	1.16	11.5	7.68	25.5
Tutuila	1.46	2.02	2.07	-134	-158	-159
Pacific 30S	2.19	2.41	3.51	-15.8	-18.9	-46.2
Cape Grim	1.48	1.64	2.78	-5.16	3.39	2.21
Syowa	1.66	1.67	1.84	19.6	17.9	16.0
South Pole	1.47	1.45	1.53	16.3	14.4	13.4

[1]Model minus observed

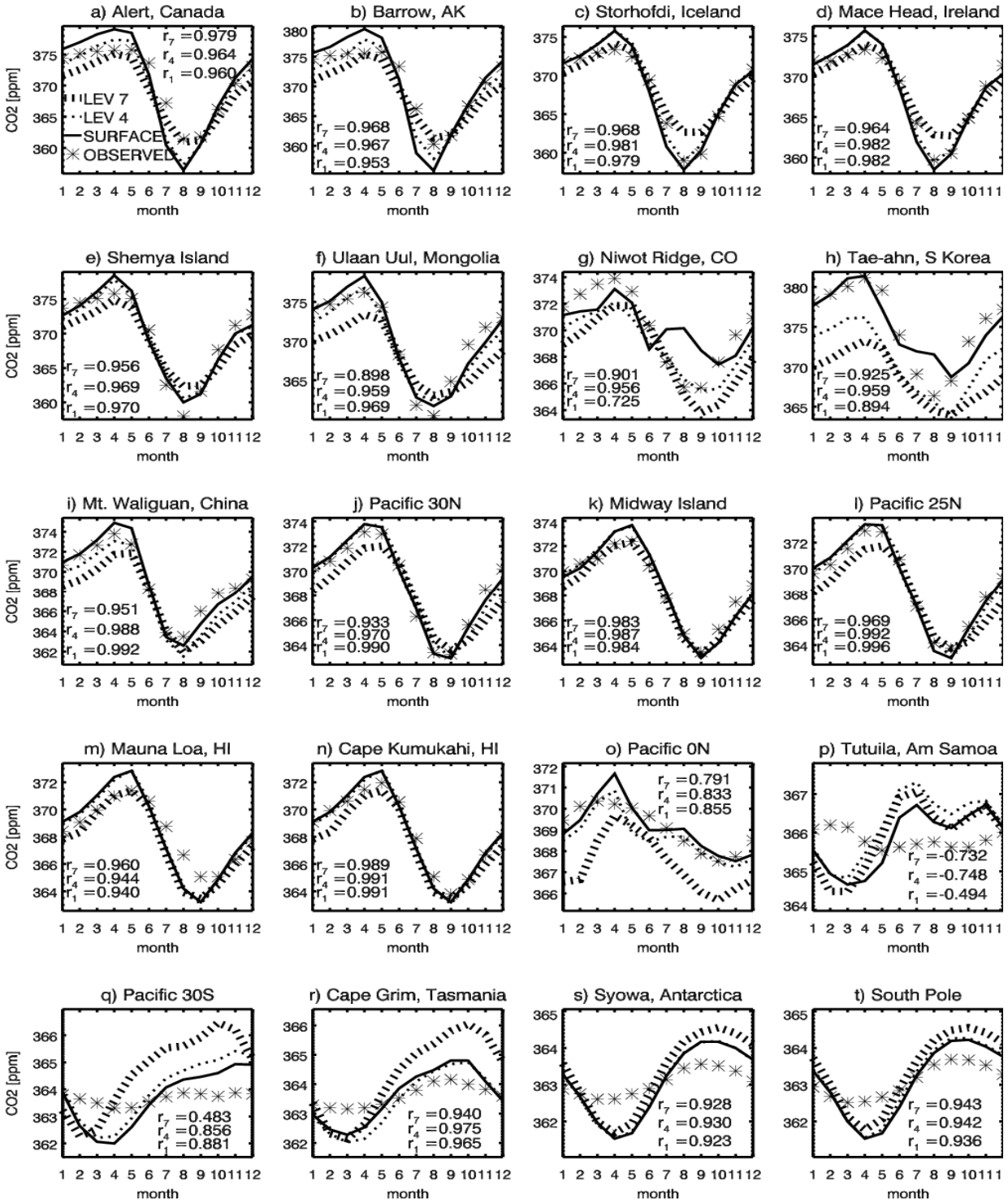

Figure 3.3. Observed seasonal cycles of CO_2 (ppm) for twenty stations around the world that have many observations on record (shown as asterisks). Solid line is the simulated seasonal cycle at the model's surface level for the closest grid-cell, while the dotted and dashed lines are the 4th and 7th model level, respectively.

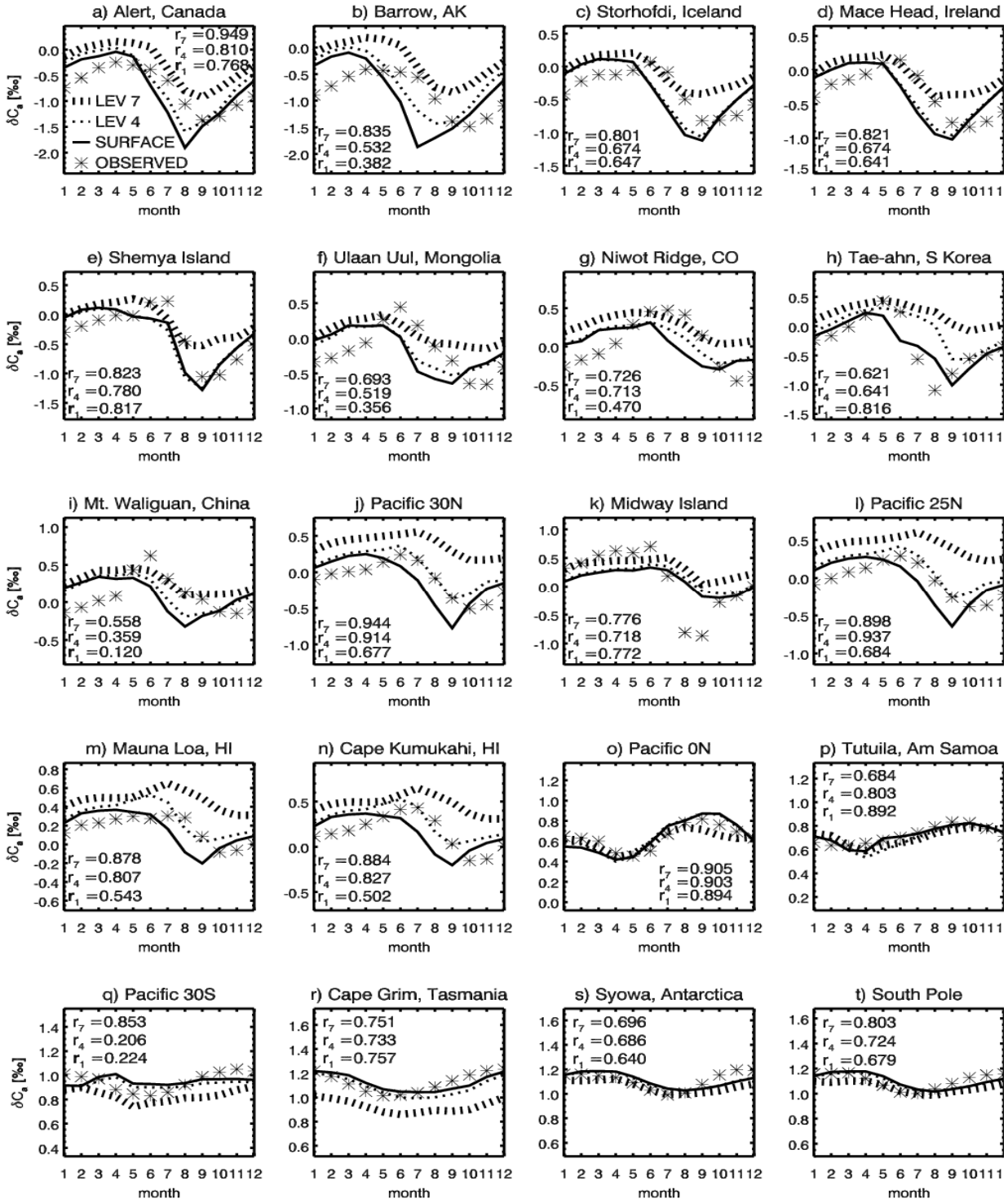

Figure 3.4. Observed seasonal cycles of δC_a (‰) for twenty stations around the world (shown as asterisks). Solid line is the simulated seasonal cycle at the model's surface level for the closest grid-cell, while the dotted and dashed lines are the 4th and 7th model level, respectively.

Examining the simulated δC_a seasonal cycle (Figure 3.4) revealed that the amplitude and phase for some stations agreed well with observations at the lowest model level (e.g., Shemya Island and Pacific Ocean 0º), while most stations agreed well at the 4th or 7th atmospheric layer (e.g., Alert, Barrow, Mauna Loa), and others were not accurately predicted at any atmospheric layer (e.g., Midway Island, Ulaan Uul, Mt. Waliguan). There was also good agreement at stations in the Southern Hemisphere like the South Pole, Cape Grim, and American Samoa, though the agreements are questionable due to inaccurate CO_2 amplitudes at these stations. Alternatively, at Barrow and Alert the modeled surface amplitude was too large and the phase leads the observations by about 2 months (63.5 days for Barrow) when comparing with the model surface level, but there was much better agreement at higher levels in the atmosphere (30.3 days). Based on the correlation coefficients in Figure 3.4 and the amplitude and phase differences in Table 3.3, the station where the model performed the worst is at Mt. Waliguan, where both the amplitude and phase were inaccurately simulated. It was found that the model performs better when comparing the observations with levels further up in the atmosphere beyond the 7th level, which would suggest that the model/observation mismatch is likely due to the model not resolving certain topographic features well for this region. Nonetheless, these results suggest that the model adequately predicted δC_a at most of the observing stations around the world. Furthermore, the results shown in this section give confidence in the model's ability to accurately predict the global mean, the north-south gradient, and the seasonal cycle of δC_a.

Table 3.3. Model-observation differences in δC_a seasonal cycles.

	[1]Amplitude difference			[1]Phase difference		
	Surface	4th level	7th level	Surface	4th level	7th level
Alert	0.673‰	0.443‰	-0.772‰	-36.6 days	-34.9 days	-16.8 days
Barrow	0.628	0.310	-0.0803	-63.5	-56.2	-30.3
Storhofdi	0.307	0.249	-0.282	-47.4	-45.2	-30.2
Mace Head	0.108	0.0494	-0.392	-49.1	-46.6	-31.5
Shemya Island	0.0639	0.0142	-0.514	-36.4	-38.0	-23.3
Ulaan Uul	-0.298	-0.408	-0.633	-60.1	-57.0	-39.5
Niwot Ridge	-0.334	-0.394	-0.529	-60.7	-45.2	-45.0
Tae-ahn	-0.332	-0.667	-1.02	-3.76	26.8	36.7
Mt. Waliguan	-0.138	-0.220	-0.429	-89.3	-72.8	-56.5
Pacific 30N	0.239	-0.040	-0.381	-43.7	-18.8	13.0
Midway Island	-1.05	-1.07	-1.11	29.9	36.4	28.2
Pacific 25N	0.218	-0.0160	-0.312	-45.4	-16.5	19.5
Mauna Loa	0.167	0.100	-0.0596	-47.6	-19.1	25.7
Cape Kumukahi	-0.0283	-0.0947	-0.255	-55.7	-27.2	17.6
Pacific 0N	0.0700	0.0877	-0.854	-19.0	-18.7	13.2
Tutuila	0.0259	0.0735	-0.0102	13.2	29.3	42.0
Pacific 30S	-0.125	-0.113	-0.0612	32.4	34.8	22.7
Cape Grim	-0.0553	-0.0269	-0.0766	41.5	43.8	40.2
Syowa	-0.0538	-0.0552	-0.0808	51.4	47.6	46.3
South Pole	-0.0125	-0.0219	-0.0559	48.4	45.1	36.3

[1]Model minus observed

3.4 Sensitivity of δC_a

3.4.1 Sensitivity to Relative Humidity

Transpiration is driven by the diffusion of vapor from leaves, and that rate is driven by the difference between the vapor pressure in the interior of plant leaves and the vapor pressure of the surrounding air (which is largely in balance with energy budget constraints). As such, transpiration (and latent heat exchange in general) is expected to change when atmospheric relative humidity increases, as has been seen in observations during the mid-1990s for some

high-flux regions (Chapter 2). Indeed, when relative humidity was increased by 3.3% units, the global mean transpiration decreased by 3.6% (Table 3.4) due to a decrease in the vapor pressure gradient.

Table 3.4. Changes in the global annual means of Transpiration (Q_T), Evaporation (Q_E), photosynthesis (PSN), F_{la}, F_r, δW_l, δW_s, and δC_a.

	^1Q_T	^1Q_E	^1PSN	$^1F_{la}$	^1F_r	$^2\delta W_l$	$^2\delta W_S$	$^2\delta F_{la}$	$^2\delta F_r$	$^2\delta C_a$
RH	-3.6	-2.9	2.7	4.2	2.3	-0.38	-0.081	-0.33	-0.096	-0.21
RHTROP	-2.4	-1.1	1.3	1.9	1.1	-0.14	-0.0045	-0.10	-0.0029	-0.073
PREC	-	-	-	-	-	-2.1	-2.7	-1.8	-3.8	-1.8
WV	-	-	-	-	-	-1.4	-0.065	-1.3	-0.054	-0.78
PRECWV	-	-	-	-	-	-3.5	-3.0	-3.2	-3.9	-2.6
PRECTROP	-	-	-	-	-	-1.0	-0.91	-0.89	-1.9	-0.92
WVTROP	-	-	-	-	-	-0.67	-0.0010	-0.64	-0.0048	-0.37
PRECWVTROP	-	-	-	-	-	-1.7	-0.91	-1.5	-1.9	-1.3
TEMP	0.89	-0.63	0.25	-1.8	-0.44	-0.19	-0.055	-0.22	-0.17	-0.16
LIGHT	-0.059	-1.6	3.0	4.4	2.8	-0.19	-0.013	-0.16	0.019	-0.048
ASSIM	-	-	3.6	3.6	-	-	-	-	-	0.10
RESP5	-	-	-	-	3.6	-	-	-	-	-0.10

[1] Units are in %
[2] Units are in ‰

A similar result also occurred for soil water where the increase in humidity causes a 2.9% reduction in evaporation and a slight increase (1.4%) in soil moisture. These changes in latent heat fluxes likely caused a change to the $CO^{18}O$ isoforcing to the atmosphere from the leaves (I_{la}) and respiration (I_r), which can be quantified by:

$$I_{la} = F_{la}(\delta F_{la} - \delta C_a) \qquad (3.15)$$

$$I_r = F_r(\delta F_r - \delta C_a) \qquad (3.16)$$

It can be seen from equations (3.15) and (3.16) that the isoforcings are dependent on both the magnitude and the isotopic composition of the fluxes. Because the isotopic composition of the flux is strongly related to the isotopic composition of leaf and soil water, changes to δW_l and δW_S are first evaluated and then fluxes from leaves and soils (F_{la} and F_r).

The predicted decrease in transpiration is consistent with a reduction in kinetic fractionation (equation 3.1). This change reduced leaf water ^{18}O enrichment, resulting in a reduced enrichment of the CO_2 molecules upon equilibration within the stomatal cavity. The global changes in the isotopic compositions of leaf and soil water were -0.38‰ and -0.081‰, respectively. Differentiating equation (3.1) with respect to humidity gives an upper limit to the expected relationship between leaf water ^{18}O content and humidity; for typical values of δW_S, δW_{CV}, and the fractionation coefficients, $\partial \delta W_{l\text{-}CG} / \partial h \approx$ -0.36‰/1%. ISOLSM predicted that the 3.3% increase in relative humidity only caused a 2.0% increase in photosynthesis-weighted h_l. This change in h_l caused a global reduction in photosynthesis-weighted δW_l to be slightly over half the theoretical value expected from the Craig-Gordon [1965] steady-state model. This difference was partially due to the fact that ISOLSM used the time-dependent leaf water model rather than the steady-state model. The non-steady-state model reduced the diurnal amplitude of leaf water enrichment, and in particular restricted the otherwise extreme enrichment during early afternoon.

Predicted changes in leaf and soil CO_2 fluxes are shown in Table 3.4. The increase in relative humidity caused a global increase in predicted assimilation, which in turn increased the leaf-to-atmosphere flux globally by 4.2%, and thereby increased the isoforcing to the atmosphere. However, this effect will be partially balanced by the reduction in δF_{la}. The RH

experiment also showed similar changes to the soil respired CO_2 fluxes, which for many regions depletes the atmosphere of $CO^{18}O$. Growth respiration is related to both the leaf area index and assimilation, and because assimilation increased, growth respiration also increased, which led to an overall increase in total respiration. For regions where soil respiration depletes δC_a values, the combination of more depleted soil water (and thus decreased δF_r) and an increase in respiration both act to increase the depleting isoflux, I_r. Thus, it was not clear if the changes to leaf fluxes caused δC_a to go up or down from equation (3.15) alone, though the changes to respiratory fluxes should cause δC_a to decline (through equation 3.16), which highlights the need to use a full energy balance model like ISOLSM.

To disentangle the two effects (the leaf flux increase and the isotopic depletion) the RH and RHTROP sensitivity experiments (where relative humidity was increased by 3.3% globally and only within the tropics, respectively) were examined. Globally, the RH experiment depleted δC_a by 0.21‰, and results from RHTROP indicate that 0.073‰ of this response was from the tropics. Thus, most of the response to the relative humidity change was from regions outside of the tropics. The largest changes to δC_a were in the Northern high-latitudes and in particular over northern Canada and Siberia (Figure 3.5a). When the relative humidity anomaly was only applied to the tropics the change in δC_a over the Northern regions was greatly diminished, an indication that the large response was largely locally driven. These two Northern regions have strong depleting isofluxes from both leaf and soil components, and the relative humidity increase not only further depleted the isotopic composition of fluxes, but also increased the fluxes themselves. This response was not the case for regions within the subtropics and parts of the middle latitudes where leaf fluxes do not always deplete the atmosphere of $CO^{18}O$. These results

suggest that small changes in global relative humidity could have an influence on δC_a, and potentially explain some of the decrease observed in the mid-1990s (Chapter 2).

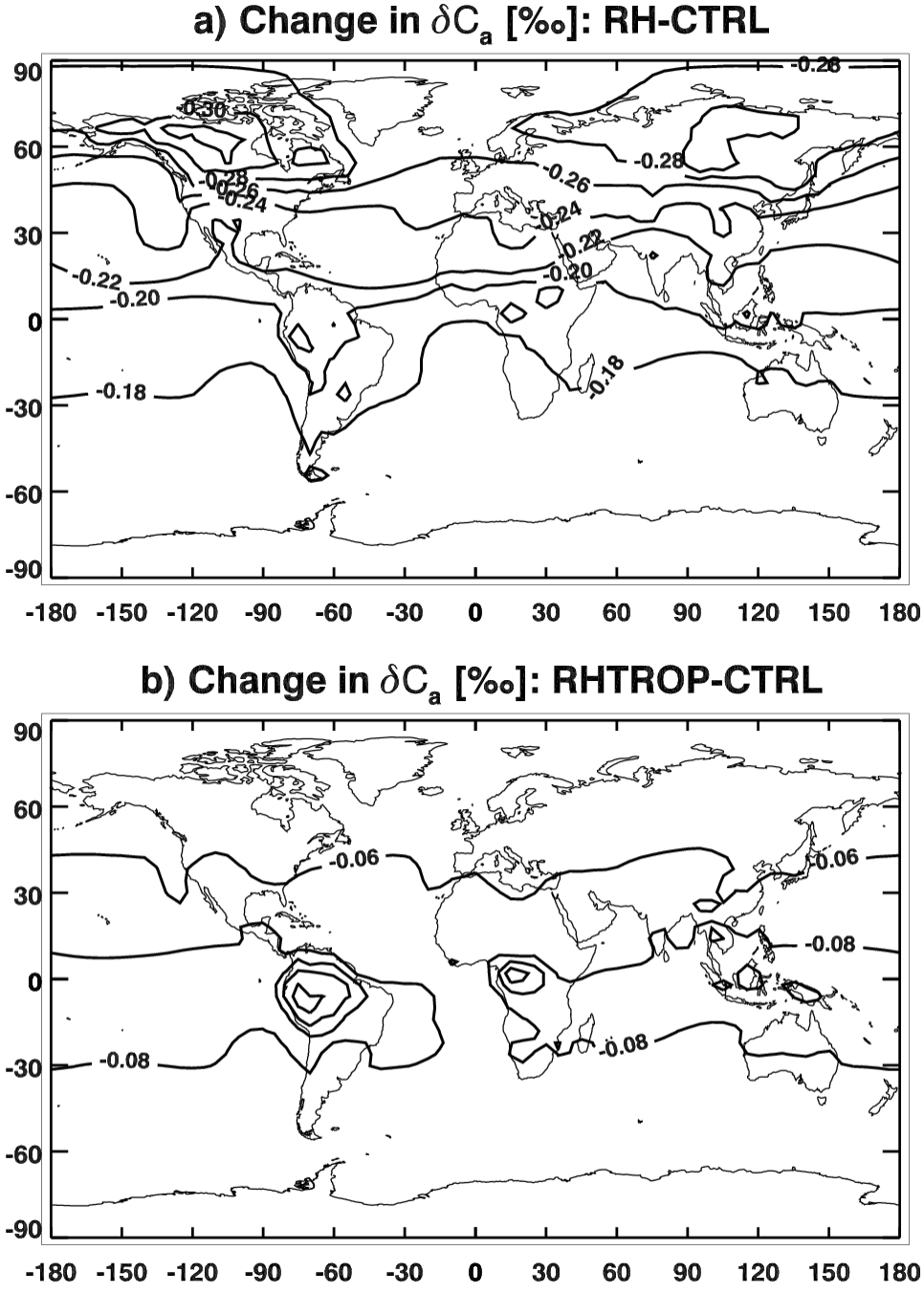

Figure 3.5. Global distribution of the change in annual mean δC_a (‰) for the RH (a) and RHTROP (b) experiments. Contour intervals are 0.02‰, which is a different interval than Figure 3.6.

3.4.2 Sensitivity of δC_a to $\delta^{18}O$ Values of Precipitation and Water Vapor

The isotopic compositions of leaf and soil water depend on the $\delta^{18}O$ values of precipitation and atmospheric water vapor (δW_P and δW_{AV}). The soil water ^{18}O content should be closely linked with δW_P, and δW_l depends on the $\delta^{18}O$ values of soil water (via root uptake without fractionation; equation 3.1) and the $\delta^{18}O$ values of canopy vapor. Therefore, it is hypothesized here that decreases in δW_P will reduce both δW_l and δW_S, which would ultimately reduce δC_a.

As described in section 3.2.3, two experiments were constructed to examine the effects of changes in δW_P: 1) an overall 3.2‰ decrease in δW_P (PREC) and 2) a 3.2‰ decrease in δW_P in only the tropics (PRECTROP). The reduction of δW_P by 3.2‰ caused δW_l and δW_S to decrease globally by 2.1‰ and 2.7‰, respectively (Table 3.4). Results from the PRECTROP simulation reveal that the tropics contributed about half of the change in photosynthesis-weighted δW_l, (i.e. the tropics make up about half of global photosynthesis).

To examine the impact of the $\delta^{18}O$ value of atmospheric water vapor (δW_{AV}) on the isotopic composition of leaf and soil water, the same perturbations were applied to δW_{AV}. Lowering δW_{AV} by 3.2‰ (WV) caused a global decrease in δW_l and δW_S of 1.4‰ and 0.065‰, respectively. When the change was only applied to the tropics there was approximately no change to the global mean δW_S. These results suggest that δW_l is sensitive to changes in the isotopic composition of atmospheric vapor as implied by equation 3.1, though soil water is not. Not surprisingly, these simulations revealed that δW_S is mostly dependent on the isotopic

composition of precipitation, but δW_l depends on both the isotopic composition of precipitation and vapor.

In the PRECWV simulation, where δW_P and δW_{AV} were both reduced by 3.2‰, the isotopic composition of soil water only decreased by 3.0‰. The small discrepancy between the perturbation and the response was a result of bottom layer recharge when the soil column dried out. In the model, the recharged water carries the same isotopic composition of the bottom soil layer, so the recharge of bottom layer water is only indirectly affected by the isotopic forcing. The isotopic composition becomes even less dependent on precipitation if the rate of recharge is greater than the infiltration rate. Results from the PRECWVTROP simulation showed that 1.7‰ of the change in δW_l comes from the tropics, which again is a consequence of about half of global photosynthesis coming from the tropics.

The changes in the isotopic composition of the water pools induced similar changes to the isotopic composition of ecosystem fluxes and subsequently of atmospheric CO_2, as expected (Table 3.4 and Figure 3.6). For the experiments in which only the isotopic composition of precipitation is reduced (PREC and PRECTROP) global and annual mean δC_a decreased by 1.8‰ and 0.92‰, respectively. The reduction in δC_a was not as large when only δW_{AV} was decreased in the WV and WVTROP simulations (-0.78‰ and -0.37‰, respectively). When the isotopic composition of both precipitation and water vapor were reduced in the PRECWV and PRECWVTROP experiments, the model predicted a larger change to the global and annual mean δC_a (-2.6‰ and -1.3‰, respectively).

For all three globally perturbed experiments, the largest impacts to δC_a occurred over the continents, and as a consequence most of the change was in the Northern Hemisphere (Figure

3.6). Thus, a global decrease in δW_P or δW_{AV} would drive an increase in the δC_a latitudinal gradient, and vice versa. On the other hand, when the offset was only applied to the tropics the opposite occurred (i.e., the largest δC_a decrease occurred in the Southern Hemisphere). Hence, the tropical only change acted to decrease the δC_a latitudinal gradient.

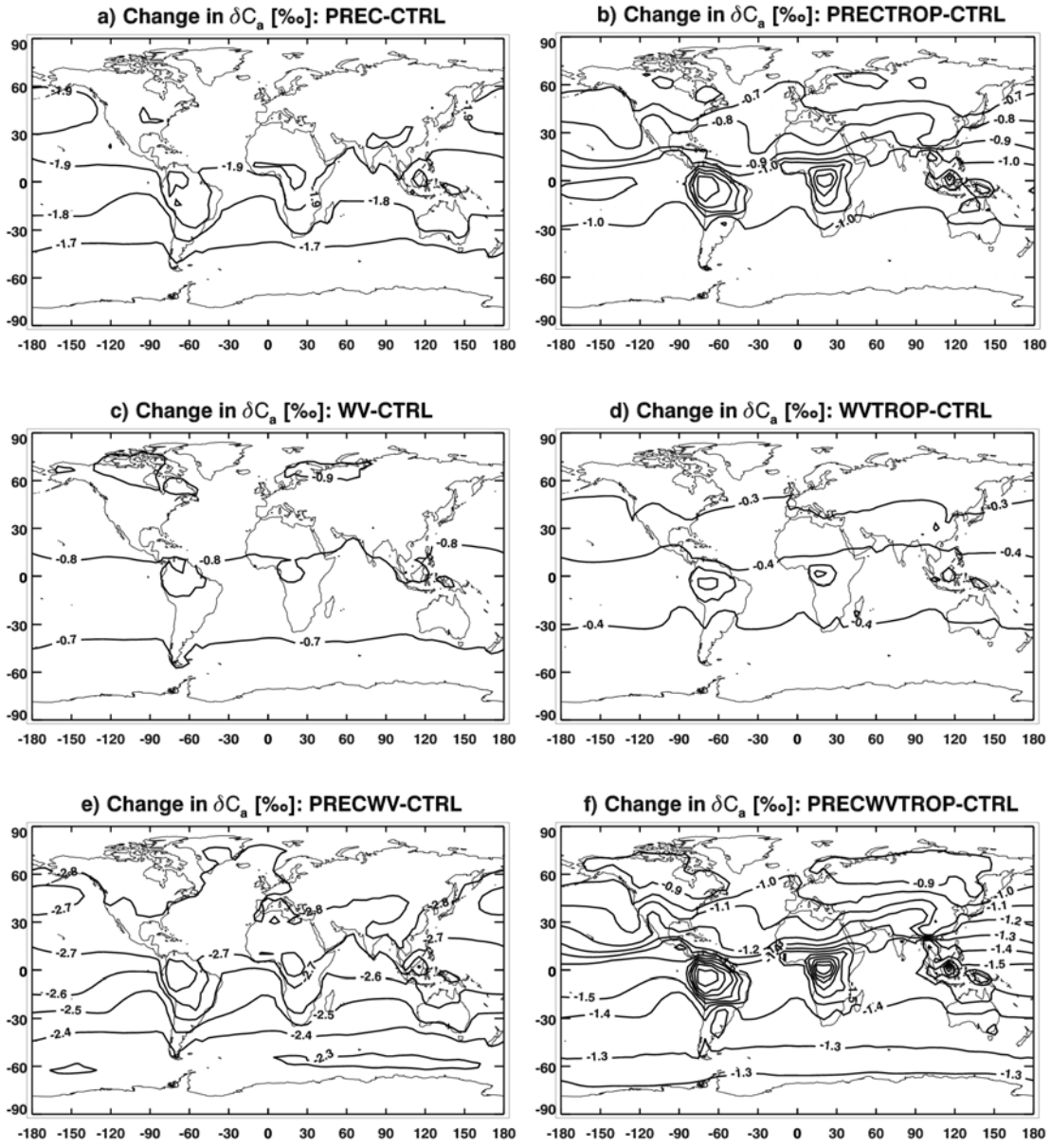

Figure 3.6. Global distribution of the change in annual mean δC_a (‰) for the PREC (a), PRECTROP (b), WV (c), WVTROP (d), PRECWV (e), and PRECWVTROP (f) experiments. Contour intervals are 0.1‰, which is different than Figures 3.5, 3.7, and 3.9.

3.4.3 Sensitivity to Radiation

The LIGHT experiment attempted to represent light levels following the eruption of Mt. Pinatubo by reducing total downwelling solar radiation by 4% and repartitioning 7.5% of the direct light to diffuse light (15% total) [*Gu et al.*, 2003]. Two additional simulations were also conducted that imposed each light level change separately to better understand which change dominates the model response. Model predictions revealed that these radiation changes caused global mean transpiration to decrease by only 0.059%. Because diffuse light is able to reach the leaves deeper within the canopy, proportionally more evaporation from shaded leaves can result, and thus more diffuse light could drive an increase in ecosystem transpiration when and where the leaf area index is high. On the other hand, the 4% reduction in total solar downwelling will cause decreases in leaf temperature and water evaporation from the mesophyll cells. Results from the additional experiments revealed that the 4% reduction caused global transpiration to decrease by 1.85%, while the repartitioning from direct to diffuse radiation caused a 1.80% increase in transpiration. Thus, the two radiation changes opposed one another and resulted in a very small change in global average transpiration.

The very small change in transpiration is not expected to impact the isotopic composition of the leaf water. However, photosynthesis-weighted δW_l was reduced globally by 0.19‰. About 0.1‰ of the change was due to a 0.3% global increase in photosynthesis-weighted values of h_l that resulted from the radiation changes. The other 0.09% was due to increases in photosynthesis, especially over the northern boreal forests where δW_l was low relative to the global mean. The 0.19‰ decrease in δW_l resulted in a 0.16‰ decrease in δF_{la}. The decrease in soil evaporation lowered δW_S by only 0.013‰, though the values of δF_r increased globally by

0.019‰. The difference in sign between these two isotopic changes was a result of a slight decrease in soil temperatures, which influenced H_2O-CO_2 equilibrium fractionation.

δC_a was most sensitive to radiation changes in the interior of northern Canada and northern Asia, the same regions where relative humidity and isotope hydrology changes caused the largest δC_a response. These responses occurred because δF_{la} was lowest for these two northern regions (Figure 3.8), and thus had the most negative isoforcing from leaves (equation 3.15) than any other continental region. Any decrease to δF_{la} (as occurred in the global sensitivity experiments shown here) will have caused the isoforcing to be even more negative and drive down regional δC_a even further. However, the light level changes only caused a 0.048‰ decrease in the global mean δC_a, which was a much smaller response compared to relative humidity and isotope hydrology changes (Table 3.4).

3.4.4 Sensitivity to Temperature

Temperature influences the isotopic composition of leaf and soil water and CO_2, partially through its impact on equilibrium fractionation *Majoube* [1971]:

$$\varepsilon_{LV}(T) = \left(\exp\left(\frac{1137}{T^2} - \frac{0.4156}{T} - 0.0020667 \right) - 1 \right) \cdot 10^3 \qquad (3.17).$$

Differentiating equation (3.17) with respect to temperature results in a sensitivity of $d\varepsilon_{LV}/dT = -0.099‰K^{-1}$ at 280K. Furthermore, in the middle and high-latitudes, temperature can also constrain ecosystem fluxes [*Nemani et al.*, 2003]. Thus, temperature influences both the isotopic composition and the magnitude of the CO_2 and H_2O fluxes.

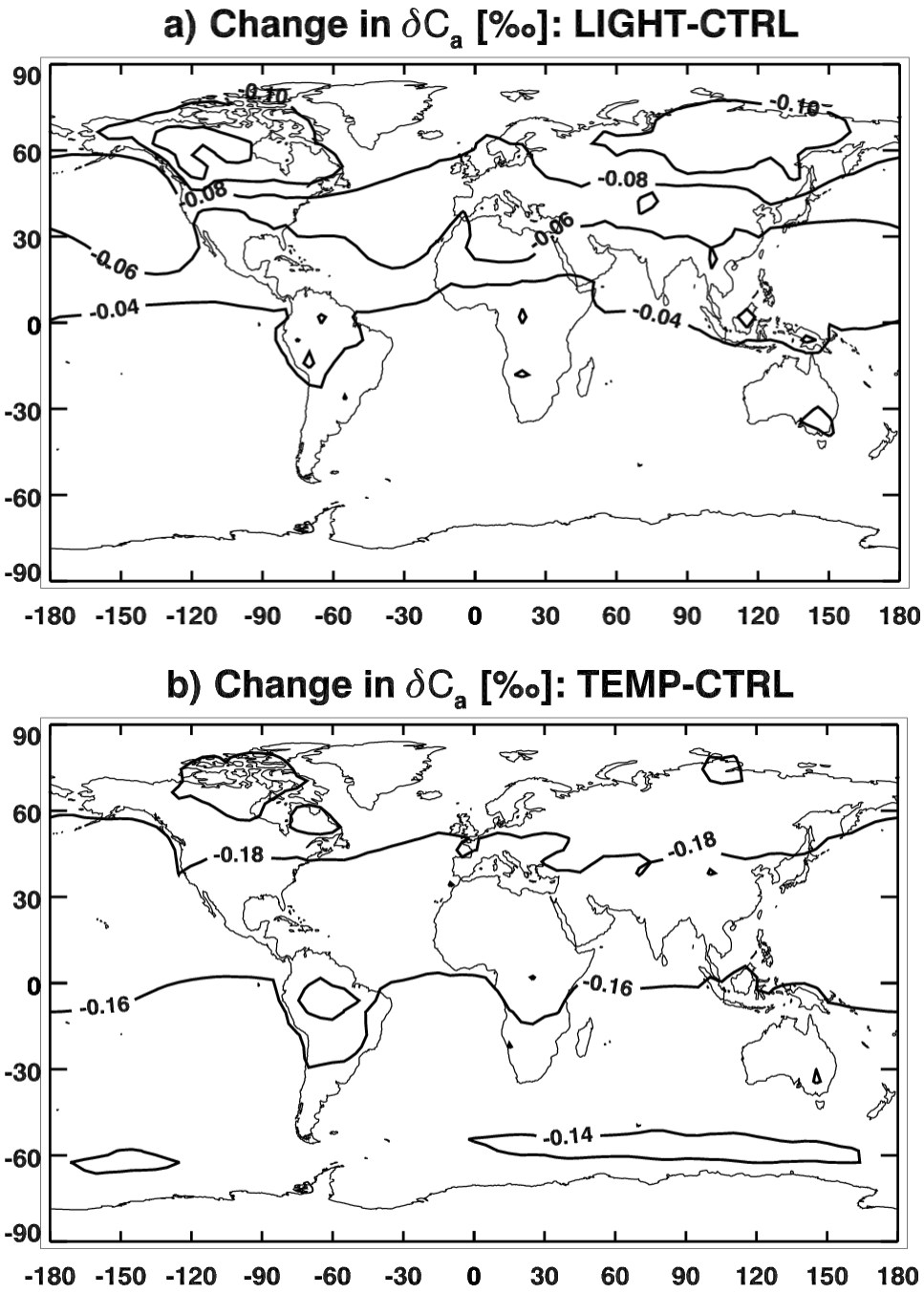

Figure 3.7. Global distribution of the change in annual mean δC_a (‰) for the LIGHT (a) and TEMP (b) experiments. Contour intervals are 0.02‰, which is different than Figure 3.6.

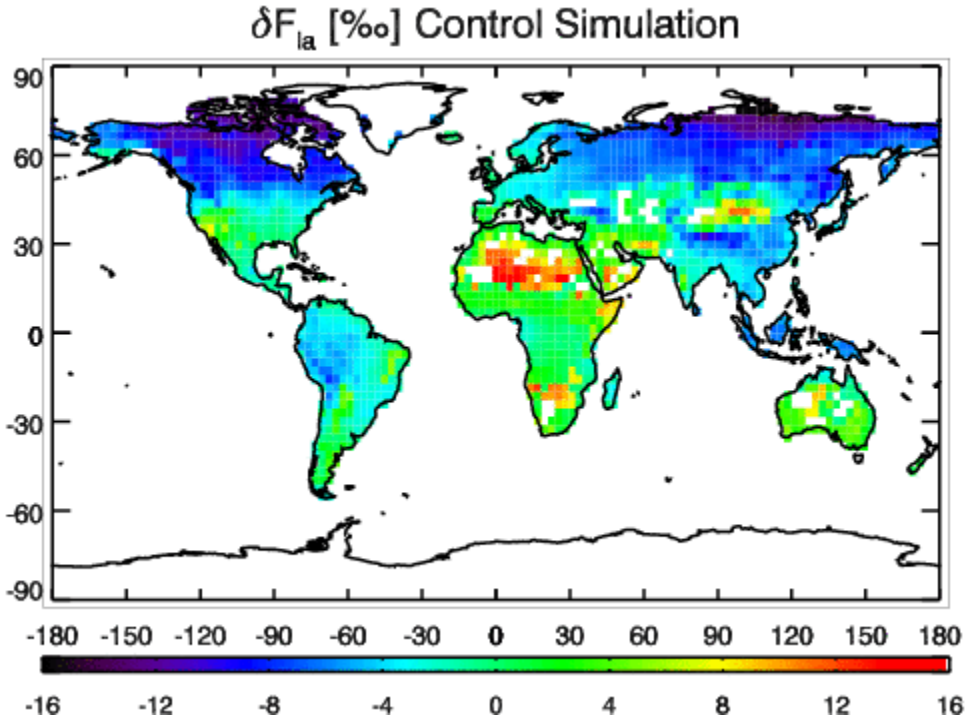

Figure 3.8. Global distribution of annual mean δF_{la} (‰) for the control simulation.

Results from the TEMP experiment showed a change in global transpiration and soil evaporation of 0.89% and -0.63%, respectively. δW_S decreased globally by 0.055‰, which was less than the theoretical sensitivity based on equilibrium fractionation. Photosynthesis-weighted δW_l decreased globally by 0.19‰. By calculating the global means of other variables (such as relative humidity and surface temperature) it was determined that 0.014‰ of the decrease due to the decrease in δW_S, 0.088‰ from the change of ε_{LV} in equation (3.1), 0.010‰ from changes to photosynthesis, and about 0.055‰ due to a slight increase in relative humidity at the surface of the leaf.

Temperature-dependent equilibrium fractionation also takes place as CO_2 interacts with leaf and soil water, $d\varepsilon_{eq}/dT$ = -0.22‰/K at 280K (equation 3.2b). Both δF_{la} and δF_r decreased

more than the isotopic composition of leaf and soil water, which was a result of the change in equilibrium fractionation due to increases in ground and leaf temperatures (both of which increased globally by about 0.89K). δC_a decreased globally by 0.16‰ (Table 3.4; Figure 3.7b). As in the other experiments, the largest response to the increase in temperature was in the northern parts of Canada and Asia where the negative isoforcing in the control simulation was the greatest. These results indicate that the influence of changes in temperature on the isotopic composition of leaf and soil water, and thereby on the isotopic composition of ecosystem fluxes, can affect δC_a. However, the imposed 1K global increase in temperature was larger than the 0.74K observed increase over the past 100 years [*Trenberth et al.*, 2007]. In fact, the model results shown here suggest that global temperatures would have to increase by 3.1K to cause the observed decrease in δC_a of 0.5‰.

3.4.5 Sensitivity to assimilation/respiration partitioning

δC_a is commonly thought of as a tracer of the partitioning between assimilation and respiration. In the ASSIM experiment, assimilation was increased globally by 3.6%, while non-leaf respiration fluxes were held unchanged relative to the control simulation. Thus, there is was no change to the isotopic composition of the fluxes for this experiment. Unlike the other experiments, the largest response of δC_a to the change in leaf fluxes was in equatorial Africa (Figure 3.9a), where assimilation is high and the isoforcing is positive. Globally, the 3.6% increase in photosynthetic fluxes caused a 0.10‰ increase in δC_a. Simulated global GPP (minus leaf respiration) was 123.9 GtC y^{-1} for the control simulation, thus the ASSIM experiment

increased F_A by 4.5 GtC y^{-1}. This implies that the sensitivity of δC_a to increases in assimilation is 0.022‰ y GtC^{-1} (assuming no change to non-leaf respiration).

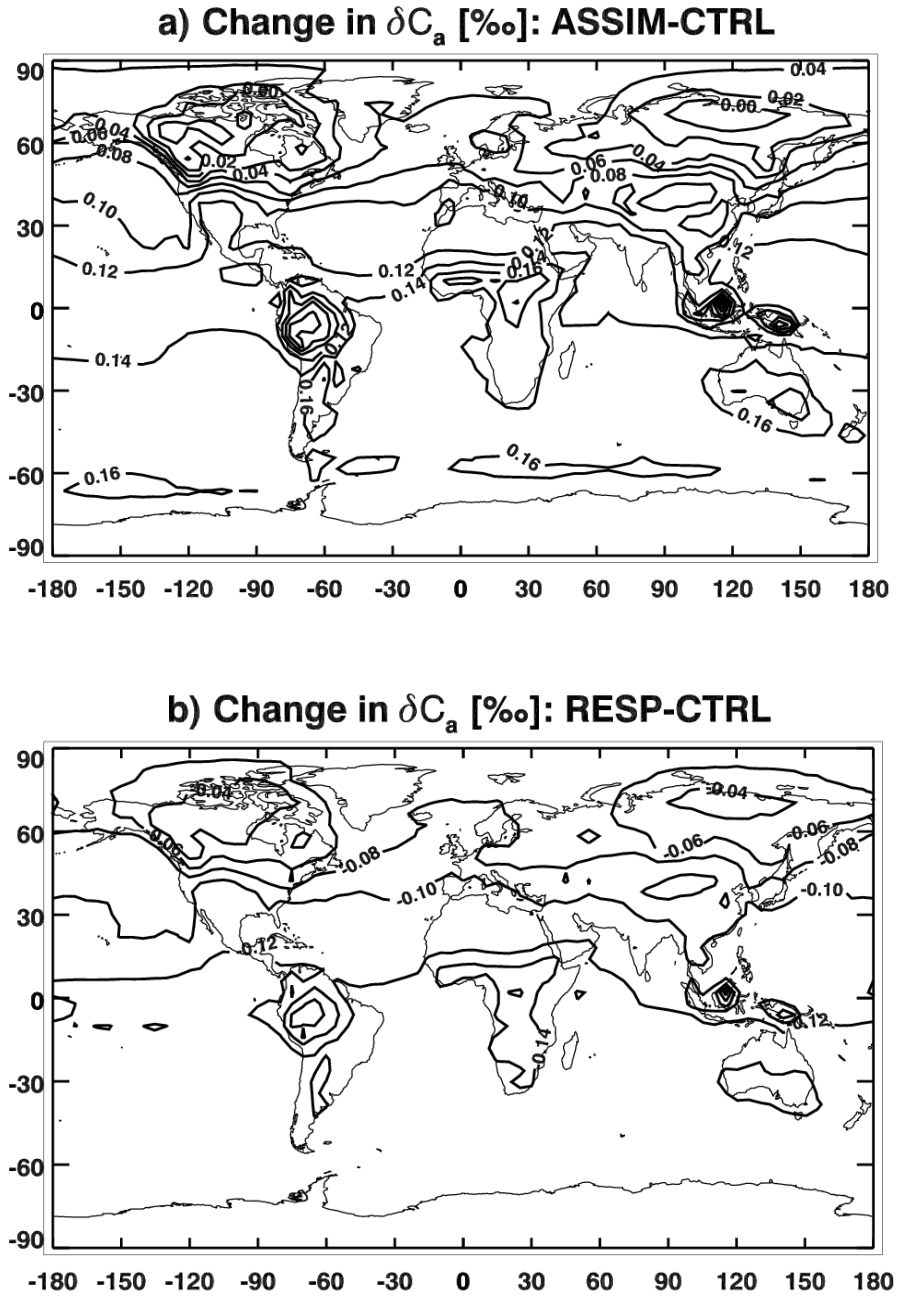

Figure 3.9. Global distribution of the change in annual mean δC_a (‰) for the ASSIM (a) and RESP (b) experiments. Contour intervals are 0.02‰, which is different than Figure 3.6.

The largest δC_a response to the 3.6% increase in non-leaf respiration (the RESP experiment) was over equatorial and southern Africa (Figure 3.9b). Globally, the RESP experiment increased respiration by 4.4 $GtCy^{-1}$. This change to respiration decreased the global mean δC_a by 0.10‰. Thus, the model results suggest δC_a decreases by 0.023‰ for every 1 $GtCy^{-1}$ increase in respiration (assuming all other fluxes remain unchanged). These results suggest that δC_a would decrease by 0.5‰ if either global assimilation decreased by 18% or non-leaf respiration increased by 18%, two scenarios that appear very unlikely.

3.5 Conclusion

A mechanistic land model (ISOLSM) was used to simulate isotopic fluxes of CO_2, which were then used in a 3-dimensional global transport model (CAM) to simulate atmospheric CO_2 and $CO^{18}O$. This framework accurately captured the global mean, north-south gradient, and to a lesser extent the seasonal cycle of δC_a. To develop an understanding of the controls on observed global-scale δC_a variations, model sensitivity experiments were performed to examine the effects of changes in humidity, $\delta^{18}O$ values of precipitation and water vapor, light levels, temperature, and assimilation/respiration partitioning on δC_a.

An imposed global 3.3% increase in relative humidity increased ecosystem fluxes and depleted the isotopic composition of leaf water and leaf $CO^{18}O$ fluxes. The increase in assimilation acted to increase δC_a, while the lighter isotopic composition of leaf and soil water caused δC_a to become lower. The overall effect was a decrease in δC_a, indicating that δC_a

responded more to changes in the isotopic composition of the water reservoirs than to changes in ecosystem fluxes.

The experiments that decreased the isotopic composition of precipitation and atmospheric vapor by 3.2‰ further demonstrated the sensitivity of δC_a to changes in the isotopic composition of leaf and soil water. Ecosystem fluxes did not change for this set of experiments, yet these perturbations resulted in the largest δC_a response. The 3.2‰ decrease in δW_P and δW_{AV} resulted in a change to δC_a that exceeded the 0.5‰ decrease observed during the mid-1990s. Model results indicate that δW_P and δW_{AV} would have to decrease by 0.62‰ globally or by 1.2‰ within the tropics to cause the observed 0.5‰ change. The results reveal the possible influence of isotope hydrology on temporal variations of δC_a.

Model results indicated that δC_a decreased by 0.16‰ for every 1K increase in global temperatures. This was primarily a result of changes to the isotopic composition of leaf and soil water and not changes to ecosystem CO_2 fluxes. However, this small sensitivity indicates that to cause the observed 0.50‰ decrease in δC_a, global temperatures would have to increase by 3.6K (and such a large change does not exist in the global temperature records).

The model was also used to simulate a post Pinatubo-like light level condition by altering direct and diffuse radiation levels and examining the effects on ecosystem CO_2 and $CO^{18}O$ fluxes and the resulting change to δC_a. The light level experiments presented here agree with other studies [*Gu et al.*, 1999; *Roderick et al.*, 2001] that argue from observations and theory that increases in diffuse light should increase global photosynthesis (and also increase the one-way leaf CO_2 fluxes). The overall effects of the light perturbations on δW_l and δW_S were small (<0.20‰). CO_2 fluxes from the leaves increased (4.4% globally) due primarily to the increased

diffuse fraction, which caused photosynthesis to increase deeper within the canopy. Respiratory fluxes also increased (globally by 2.8%) due to increased photosynthesis and subsequent increases in growth respiration. However, the changes in respiration and leaf-to-atmosphere fluxes did not substantially impact δC_a, due to minimal changes in water pool isotopic compositions.

To understand the role of assimilation/respiration partitioning, the ASSIM and RESP experiments increased assimilation and non-leaf respiration (respectively) by 3.6% globally. Model results revealed that a 3.6% increase in assimilation caused a 0.10‰ increase in δC_a, while the increase in respiration lowered δC_a by 0.10‰. These results suggest that there would need to be a large global change to either assimilation or respiration (~18%) to cause a δC_a response that is comparable to the observed change during the 1990s. Because there have been no studies that have found such a drastic change to either flux indicates that the observed δC_a variations during the 1990s were not primarily driven by changes to ecosystem CO_2 fluxes.

The results presented here suggest that δC_a is strongly dependent on hydrologic changes, such as changes to relative humidity and isotope hydrology (i.e., δW_P and δW_{AV}). Furthermore, the increase in ecosystem fluxes due to an increase in relative humidity was not large enough to outweigh the decrease in leaf water enrichment. In fact, model results shown here suggest δC_a responded mostly to changes in the isotopic composition of leaf and soil water rather than global changes to ecosystem CO_2 fluxes. This result contrasts with previous conclusions that δC_a can be interpreted primarily as a tracer of photosynthetic and respiratory fluxes [*Farquhar et al.*, 1993; *Cuntz et al.*, 2003b].

In the mid-1990s observations showed a global decrease to δC_a, which some studies have attributed to terrestrial carbon flux anomalies [*Gillon and Yakir*, 2001; *Stern et al.*, 2001; *Ishizawa et al.* 2002; *Flanagan* 2005]. The results presented here do not support this claim, but instead were consistent with the empirical work shown in Chapter 2, which suggested that the global decrease in δC_a during the mid-1990s may have been a result of decreases in δW_P and δW_{AV} and an increase in relative humidity within the tropics. In Chapter 2, empirical evidence was provided for changes to these variables during the 1990s, and the present modeling study has shown that these variables do indeed influence δC_a. It remains, however, to demonstrate (through model simulations) that the interannual variability in δC_a can be quantitatively explained by hydrologic mechanisms exposed here.

Appendix 3.A: Notation

C_a	CO_2 mixing ratio in the atmosphere (mole fraction).
${}^{18}C_a$	$CO^{18}O$ mixing ratio in the atmosphere (mole fraction).
C_C	CO_2 mixing ratio at the surface chloroplast within leaf stomata (mole fraction).
C_i	CO_2 mixing ratio inside the stomatal pores (mole fraction).
F_{al}	CO_2 flux into leaves (mol m^{-2} s^{-1}).
${}^{18}F_{al}$	$CO^{18}O$ flux into leaves (mol m^{-2} s^{-1}).
F_{ao}	CO_2 flux into the ocean surface (mol m^{-2} s^{-1}).
${}^{18}F_{ao}$	$CO^{18}O$ flux into the ocean surface (mol m^{-2} s^{-1}).
F_b	CO_2 flux from biomass burning (mol m^{-2} s^{-1}).

$^{18}F_b$	$CO^{18}O$ flux from biomass burning (mol m^{-2} s^{-1}).
F_{la}	CO_2 flux out of leaves (mol m^{-2} s^{-1}).
$^{18}F_{la}$	$CO^{18}O$ flux out of leaves (mol m^{-2} s^{-1}).
F_f	CO_2 flux due to fossil fuel consumption (mol m^{-2} s^{-1}).
$^{18}F_f$	$CO^{18}O$ flux due to fossil fuel consumption (mol m^{-2} s^{-1}).
F_A	Gross Primary Product minus leaf respiration (mol m^{-2} s^{-1}).
F_o	net flux of CO_2 from ocean water (mol m^{-2} s^{-1}).
F_{oa}	CO_2 flux from the ocean surface (mol m^{-2} s^{-1}).
$^{18}F_{oa}$	$CO^{18}O$ flux from the ocean surface (mol m^{-2} s^{-1}).
F_r	CO_2 flux from soil respiration (mol m^{-2} s^{-1}).
$^{18}F_r$	$CO^{18}O$ flux from soil respiration (mol m^{-2} s^{-1}).
h_l	relative humidity at leaf surface (range of 0 to 1.0)
I_{la}	Isoforcing from leaf-to-atmosphere fluxes (‰ mol m^{-2} s^{-1})
I_r	Isoforcing from soil respiration (‰ mol m^{-2} s^{-1})
K_{ex}	air-sea gas exchange coefficient (mol m^{-2} s^{-1} Pa^{-1})
M_a	Unit conversion factor (moles of air m^{-2}).
p_a	partial pressure of CO_2 in the atmosphere (Pa).
p_o	partial pressure of CO_2 at ocean surface (Pa).
PSN	Photosynthesis (μmol m^{-2} s^{-1}).
Q_E	Soil Evaporation (μmol m^{-2} s^{-1}).
Q_T	Transpiration (μmol m^{-2} s^{-1}).
R_{lw}	^{18}O isotopic ratio of leaf water.

R_l	^{18}O isotopic ratio of CO_2 equilibrated with leaf water.
R_o	^{18}O isotopic ratio of CO_2 equilibrated with surface ocean water.
R_{ow}	^{18}O isotopic ratio of surface ocean water.
R_{O2}	^{18}O isotopic ratio of atmospheric O_2.
R_{sw}	^{18}O isotopic ratio of root weighted soil water.
R_s	^{18}O isotopic ratio of CO_2 equilibrated with root-weighted soil water.
R_{cv}	^{18}O isotopic ratio of canopy water vapor.
R_v	^{18}O isotopic ratio of atmospheric water vapor.
R_{VPDB}, R_{VSMOW}	2.08835×10^{-3}, 2.0052×10^{-3}
T_s	Surface Temperature of either: ocean, soil, or vegetation (K).
α_{eq}	temperature dependent CO_2 equilibration factor.
α_l	Effective kinetic fractionation factor for $CO^{18}O$ diffusion in and out of the stomata.
α_w	effective kinetic fractionation factor for $CO^{18}O$ diffusion in and out of surface ocean water.
δC_a	$\delta^{18}O$-CO_2 value of free air (‰ versus VPDB-CO_2).
δC_l	$\delta^{18}O$-CO_2 value of CO_2 equilibrated with leaf water (‰ versus VPDB-CO_2).
δC_o	$\delta^{18}O$-CO_2 value of CO_2 equilibrated with surface ocean water (‰ versus VPDB-CO_2).
δC_S	$\delta^{18}O$-CO_2 value of CO_2 equilibrated with soil water (‰ versus VPDB-CO_2).
δF_{la}	$\delta^{18}O$-CO_2 value of leaf-to-atmosphere CO_2 flux (‰ versus VPDB-CO_2).
δF_r	$\delta^{18}O$-CO_2 value of soil respiration (‰ versus VPDB-CO_2).

δW_{AV}	$\delta^{18}O$ value of atmospheric water vapor (‰ versus VSMOW-H_2O).
δW_{CV}	$\delta^{18}O$ value of canopy water vapor (‰ versus VSMOW-H_2O).
δW_l	$\delta^{18}O$ value of leaf water (‰ versus VSMOW-H_2O).
$\delta W_{L\text{-}CG}$	$\delta^{18}O$ value of leaf water (‰ versus VSMOW-H_2O) using the Craig-Gordon estimation.
δW_P	$\delta^{18}O$ value of precipitation (‰ versus VSMOW-H_2O).
δW_S	$\delta^{18}O$ value of root-weighted soil water (‰ versus VSMOW-H_2O).
ε_l	Effective kinetic fractionation factor for $CO^{18}O$ diffusion in and out of the stomata (‰).
ε_w	effective kinetic fractionation factor for $CO^{18}O$ diffusion in and out of surface ocean water, equal to +0.8‰.
ε_{eq}	temperature dependent CO_2 equilibration factor in δ notation.
ε_k	$H_2{}^{18}O$ kinetic fractionation factor for molecular diffusion.
ε_{LV}	the temperature dependent equilibrium fractionation of $H_2{}^{18}O$ during the liquid-vapor phase transition

Appendix 3.B WMO Forcing Data

A Cressman-like objective analysis [*Cressman*, 1959] is used to interpolate WMO station observations onto a grid. The procedure entails finding the weighted mean value of some quantity X (e.g. relative humidity or temperature) on a grid, given a number of values X_j with irregularly distributed positions λ_j, ϕ_j. That is,

$$X(\lambda,\phi) = \frac{1}{A(\lambda,\phi)} \frac{\sum_j X_j W(d_j)\cos\phi_j}{\sum_j W(d_j)\cos\phi_j} \tag{3.B.1}$$

where A is the area of each grid cell, and included for quantities needed in per unit area. An example is where a probability distribution of observational points is desired and where X is set to one for all points j, and the resulting field has units of probability per unit area. The weight W is a function of the great circle distance (d_j) between each grid cell center and each observation,

$$W(d_j) = \frac{R_c^2 - d_j^2}{R_c^2 + \left(\gamma^{-1} - 1\right)d_j^2} \tag{3.B.2}$$

R_c is a critical radius that ensures W is positive for all d_j larger than the critical radius, R_c. The shape of the weighting is modified by the "pinching" factor (γ), such that the mean radius of the weighting is reduced with smaller values.

This method results in missing values when the critical radius is small enough. On the other hand, the spatial structure of a variable maybe compromised due to over smoothing when the critical radius is too big. To avoid these problems, the objective analysis is looped 6-times for each day, such that the critical radius goes from large to small (R_c = 5000, 1000, 800, 600, 400, 200 km), and the pinching factor starts extremely small and only gets larger for the first two loops (γ=0.0002,0.002,0.02,0.02,0.02,0.02). Thus, the previous value with the larger radius is used to fill in grid-cells with missing values. This approach ensures local-scale features are retained where data coverage is good, but provides an interpolated value where observations are sparse.

The chosen grid has a horizontal resolution given by triangular truncation of the spherical harmonic spectrum at wave number 62, which corresponds to a Gaussian grid of about 1.875

degree longitude x 1.875 degree latitude. The computational grid is the same as the reanalysis dataset of *Qian et al.* [2005], which has eight time-samples per day. For each day and for each grid-cell in the *Qian et al.* [2005] dataset, daily means are calculated and removed for each of the eight-time samples. The remaining 'anomalies' are then added to the interpolated WMO data, thus imposing a diurnal cycle onto the observed daily means.

To demonstrate that this method accurately captures the station observations, Figure 3.9 compares examples of the observed seasonal cycle with the nearest neighbor grid-cell for the interpolated dataset, the reanalysis dataset of *Qian et al.* [2005], and the NCEP reanalysis [*Kalnay et al.*, 1992]. The comparison is done for three stations in three separate regions (two tropical and one mid-latitude). The station chosen for the comparison were ones with long observational records that show clear interannual variability and seasonal cycles. For both tropical regions, the two reanalysis datasets over-predict the amplitude of the seasonal cycle, with wet-season values that are too high and close to 100%. The interpolated dataset accurately matches the station observation. In the mid-latitudes, the seasonal cycle in relative humidity is not as clear with no monsoon to bring in a dry and wet-season. Instead the variations are dominated by atmospheric waves that bring in moisture every 5 to 7 days on average. This particular mid-latitude region does observe an annually occurring dry period during the late spring/early summer. In the reanalysis data, the dry period is slightly later in the year, and thus the seasonal cycle is not accurately captured. The interpolated data again matches up well with the stations observations, and the timing of the dry period is correct. These comparisons are the reason why the interpolated dataset is preferred over the reanalysis data to force ISOLSM. Given the importance of relative humidity found here, it is particularly important to force the model with realistic relative humidity.

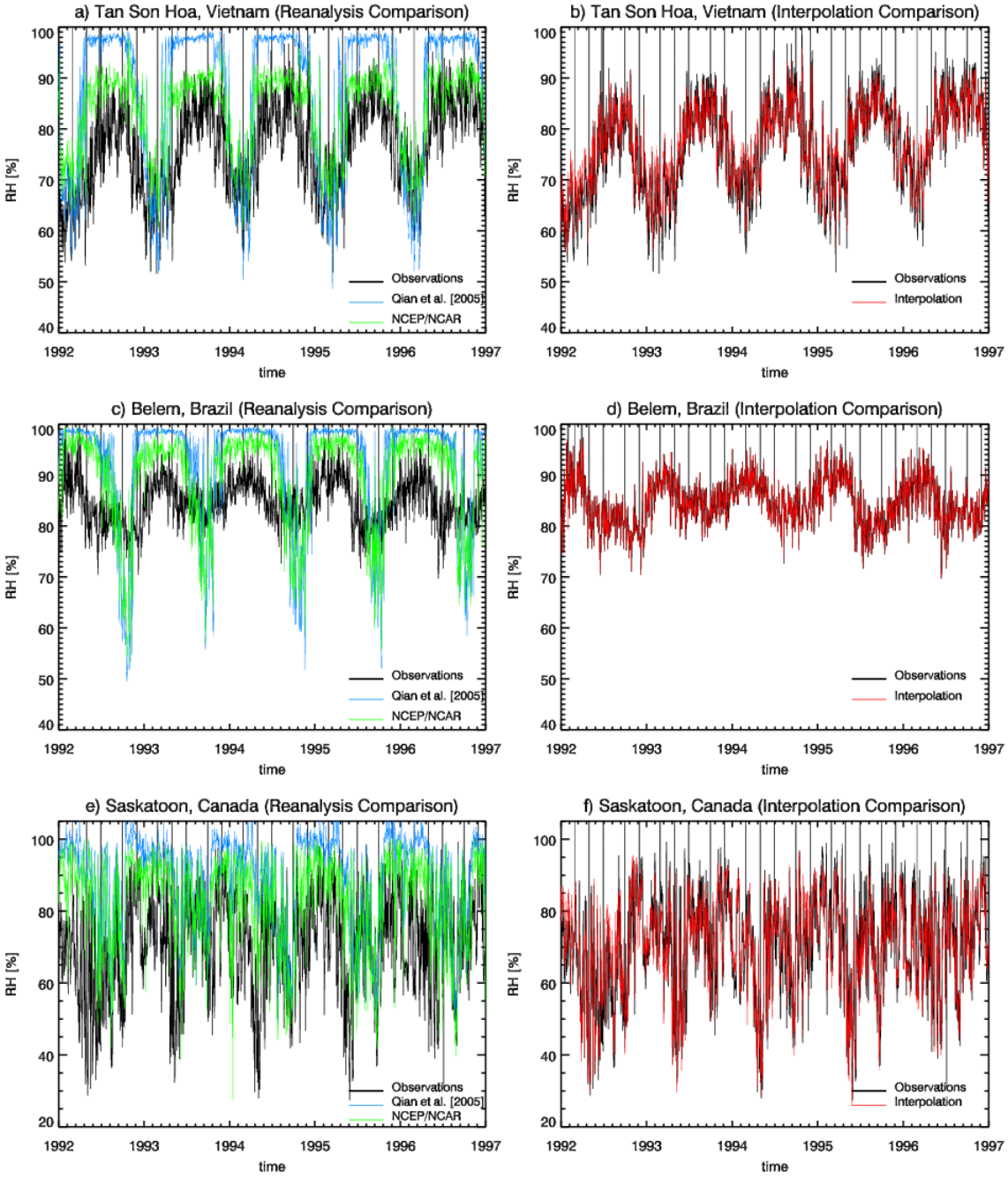

Figure 3.10. Comparison between observed variations in relative humidity and relative humidity from gridded datasets at Tan Son Hoa, Vietnam (a and b), Belem, Brazil (c and d), and Saskatoon, Canada (e and f). The black line shows the station observations, the blue line shows the reanalysis data from *Qian et al.* [2005], green line represents the NCEP Reanalysis, and the red line is the interpolated data used to force ISOLSM.

Chapter 4

Causes of the interannual variations in $\delta^{18}O$ of atmospheric CO_2 inferred from dynamical model simulations

4.1 Introduction

Carbon dioxide is believed to be the most important anthropogenic greenhouse gas in Earth's atmosphere, and its global long-term positive trend has been attributed to increases in fossil fuel consumption and biomass burning [*Keeling*, 1961; *Denman et al.*, 2007]. It is believed that increases in fossil fuel consumption and subsequent changes in ocean fluxes have contributed to the global decrease in ^{13}C content of atmospheric CO_2. However, the ^{18}O content of atmospheric CO_2 (δC_a) does not clearly show any sustained trend of increase or decrease at any of the monitoring stations. Figure 1.1 shows the observed interannual variations in δC_a at Mauna Loa, Barrow, Cape Grim, and the South Pole, and although no trend is apparent the observations show a decrease during much of 1990s followed by a slight increase after 1999.

In Chapter 1 the δC_a budget equation was examined to identify variables that could potentially drive the observed interannual δC_a variations. Considering the five major exchanges of CO_2, δC_a can be influenced by changes to either the magnitude of or the isotopic composition of a flux. Assuming the changes are related to ecosystem fluxes would suggest that the decrease in δC_a during the 1990s was due to either a change in assimilation (F_A) or respiration (F_r) or a decrease in the ^{18}O composition of leaf water (δW_l) or soil water (δW_S). Both ecosystem fluxes have potential to be influenced by temperature, solar radiation, or hydrological changes. δW_l and

δW_S can potentially be influenced by relative humidity, temperature, or isotope hydrology (i.e., changes to the isotopic composition of precipitation (δW_P) and/or vapor (δW_{AV})).

In Chapter 2 it was shown that observed interannual δC_a variations negatively correlates with relative humidity and positively with δW_P within some regions of the tropics and mid-latitudes. First order approximations suggested that the 1990s decrease in δC_a was primarily due to decreases in δW_P and/or δW_{AV} in highly productive regions. Results from Chapter 2 also revealed evidence of a smaller contribution to the δC_a decrease from increases in relative humidity in the same regions. In Chapter 3 a modeling sensitivity study showed that δC_a has a large response to global relative humidity changes as well as variations in δW_P and δW_{AV}. In particular, equilibrium model simulations showed tropical and mid-latitude relative humidity and water isotope variations were leading candidate to explain the observed interannual variations in δC_a. Motivated by these results, this study slightly modifies the model used in Chapter 3 to simulate the year-to-year changes in δC_a to examine if these mechanisms can explain interannual (or transient) δC_a variations or if the variations are a result of ecosystem CO_2 flux anomalies, as has been suggested by others [*Gillon and Yakir*, 2001; *Stern et al.*, 2001; *Ishizawa et al.* 2002; *Flanagan* 2005].

Below is a brief description of the model used to simulate the year-to-year variations in δC_a, which also includes an explanation of the experiments used with the model (a more detailed description of the model was given in Chapter 3). A control simulation is examined by assessing the ability of the model to reproduce the observed interannual δC_a variations. Experimental simulations are then conducted where one forcing variable has no interannual variations. The experiments are compared to the control simulation to evaluate how the potential driving

variables influenced the year-to-year changes in δC_a. Finally, the results found here are put into context with respect to other studies that have examined δC_a variations.

4.2 Methods

4.2.1 Control Simulation and Interannual Forcing

This study uses a similar modeling framework used in Chapter 3 to simulate δC_a. This framework uses an atmospheric transport model along with fluxes from the various components of equation 1.1 to simulate CO_2 and $CO^{18}O$ concentrations. A land surface model [*Bonan*, 1996; *Riley et al.*, 2002] was employed to calculate CO_2 and $CO^{18}O$ ecosystem fluxes. The exchange rates to and from the ocean are derived from various datasets [*Vogel et al.*, 1970; *Takahashi et al.*, 2002; *LeGrande and Schmidt*, 2006], as are fluxes from fossil fuel consumption [*Andres et al.,* 1996] and biomass burning [*Van der Werf et al.*, 2006]. The specific details about how these datasets are used in the model can be found in Chapter 3, though certain specifics about the forcing of the land model are given below.

Photosynthetic and respiratory fluxes come from an isotopic version of NCAR's Land Surface Model (ISOLSM). ISOLSM is forced with a combination of meteorological and isotope datasets. Solar downwelling, precipitation rate, wind speed, and air pressure forcing data is taken from the daily reanalysis dataset of *Qian et al.* [2005]. Relative humidity and surface air temperature are derived from the World Meteorological Organization's Global Summary of the Day, which consists of a network of over 24,000 weather stations. Observations from each day are placed onto a grid by a method similar to *Cressman* [1959] objective analysis, which is described in detail elsewhere (Appendix 3.B). The meteorological data contains interannual variations, and can thus potentially drive year-to-year changes in F_A, F_r, δC_l and δC_S.

ISOLSM is forced with the $\delta^{18}O$ value of precipitation (δW_P) from the Global Network for Isotopes in Precipitation (GNIP) database. GNIP is a joint project of the International Atomic Energy Agency and the WMO [Isotope Hydrology Section, 2006], and the station data includes monthly means of δW_P, temperature, precipitation amount, and vapor pressure. The methods used to place long-term monthly means of δW_P onto a grid is discussed Chapter 4. Within the tropics (equatorward of 25°), interannual δW_P variations were calculated using the isotope-precipitation relationship found by *Risi et al.* [2008]: 0.6‰ mm^{-1} d. Outside of the tropics, the temporal isotope-temperature relationship found by *Jouzel et al.* [2000] (0.6‰ K^{-1}) is used for interannual δW_P variations. The precipitation and temperature variations used for the interannual regression come from the Global Precipitation Climatology Project [*Adler et al.*, 2003] and the National Center for Environmental Prediction [*Kalnay et al.*, 1996], respectively. The isotopic composition of atmospheric water vapor is computed by first calculating the offset between modeled δW_P and δW_{AV} values from the Melbourne General Circulation Model [*Noone and Simmonds*, 2002], and then applying the offset to values of δW_P. This methodology provides a consistent dataset for interannual variations in monthly δW_P and δW_{AV}, though the offset between the two will not change from year-to-year.

ISOLSM simulations are forced with data that span 1979 to 2004. The simulations go through two cycles of the 26-year period, using the last of the two cycles as input into CAM. CAM simulations were performed with a perpetual 1985 for the first 6 years, after which the interannual variability in ecosystem fluxes begins (starting with 1985).

Ocean fluxes were also employed into CAM, though no interannual variations are applied to the ocean CO_2 and $CO^{18}O$ fluxes. The isotopic composition of fossil fuel and biomass

burning fluxes maintain a constant value of -17‰, the $\delta^{18}O$ value of atmospheric oxygen. There were no interannual variations applied to biomass burning or fossil fuel consumption fluxes.

4.2.2 Interannual Experimental Simulations

Along with a control simulation that includes all variations described above, experimental model runs were conducted to examine which variables are causing the variations in δC_a. These simulations do not include interannual variations to one of the potential drivers in δC_a, thus the influence from the potential driver can be inferred when compared to the control simulation. With the name of the individual simulations in parenthesis, the potential drivers that were held constant include relative humidity (RHCON), δW_P (PRECCON), δW_{AV} (WVCON), temperature (TEMPCON), and radiation (RADCON). A complete list of the experiments is given in Table 4.1.

4.3 Model Simulation Results

4.3.1 Control Simulation

Figure 4.1 shows the global mean δC_a from the ALLVAR simulation; also shown are observed δC_a from Mauna Loa. The seasonal cycle for each time-series is removed by applying a 12-month running mean. Results are shown for the 7th model level to show mid-tropospheric values. Model results are correlated with the Mauna Loa time-series, and *r* values are also shown in Figure 4.1. The control simulation reasonably matches the observed δC_a values, with a global correlation coefficient of 0.679 (when compared to Mauna Loa). The model is able to capture the

decrease in δC_a during the 1990s and (to a lesser extent) the increase after the year 1999 (i.e. it captures the low frequency variability). Also, the model captures some high frequency features such as the strong 1997/1998 El Nino event that resulted in an increase in δC_a.

Table 4.1. Name and description of each model experiment.

Experiment Name	Description
ALLVAR	Includes interannual variations in all atmospheric forcing.
RHCON	No interannual variations in relative humidity.
ISOCON	No interannual variation in $\delta^{18}O$ of precipitation and water vapor.
ISOPCON	No interannual variation in $\delta^{18}O$ of precipitation.
ISOVCON	No interannual variation in $\delta^{18}O$ of water vapor.
TEMPCON	No interannual variations in temperature.
RADCON	No interannual variations in solar radiation.

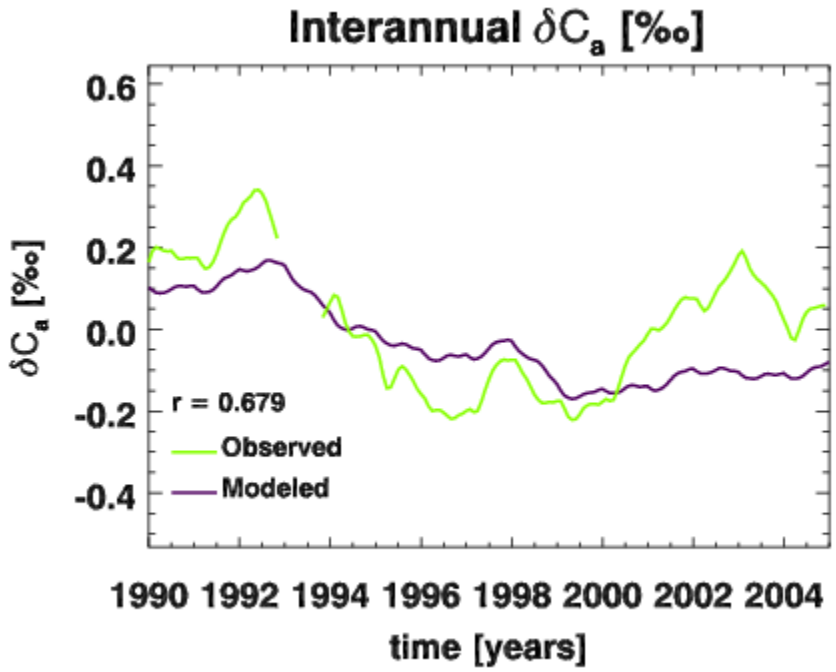

Figure 4.1. Modeled interannual global variations of δC_a (‰). The green line represents the observed values at Mauna Loa and the black line represents the simulated values.

The magnitude of the simulated variations was smaller when compared to the observed variations. For example, at Mauna Loa, observed δC_a decreased by 0.50‰ from 1992 to 1997, while the model simulates a decrease of only 0.34‰. The increase in δC_a after 1999 was also much smaller (about 0.3‰) when compared to observations. These model shortcomings could be a result of no interannual variability in factors unrelated to ecosystem fluxes, such as fluxes to and from oceans, fluxes from biomass burning and fossil fuels, or atmospheric transport variations. The shortcomings could also be due to inaccuracies in the atmospheric forcing data.

4.3.2 Experimental simulations

The RHCON simulation included no interannual relative humidity variability, and the results of the simulation are shown in Figure 4.2. To quantify the influence of relative humidity on interannual δC_a variations, δC_a from the RHCON simulation is subtracted from the results of the ALLVAR simulation. These residuals are then correlated with the observed interannual variations to quantify the influence of relative humidity on interannual δC_a variations (r_{RH}). The relative humidity variations caused the simulated δC_a to decrease during the 1990s and to slightly increase after 2000, as was observed (r_{RH} = 0.577). However, the magnitude of the induced variations was smaller than that for the ALLVAR simulation. The differences between the two simulations indicate that relative humidity contributed about 0.10‰ to the simulated 0.34‰ decrease during the 1990s. This is in good agreement with Chapter 2, which estimated that the increase in relative humidity during the 1990s caused a ~0.14‰ decrease in δC_a during the 1990s. In general, these results indicate that relative humidity contributed about 25% to the simulated decrease in δC_a during the 1990s.

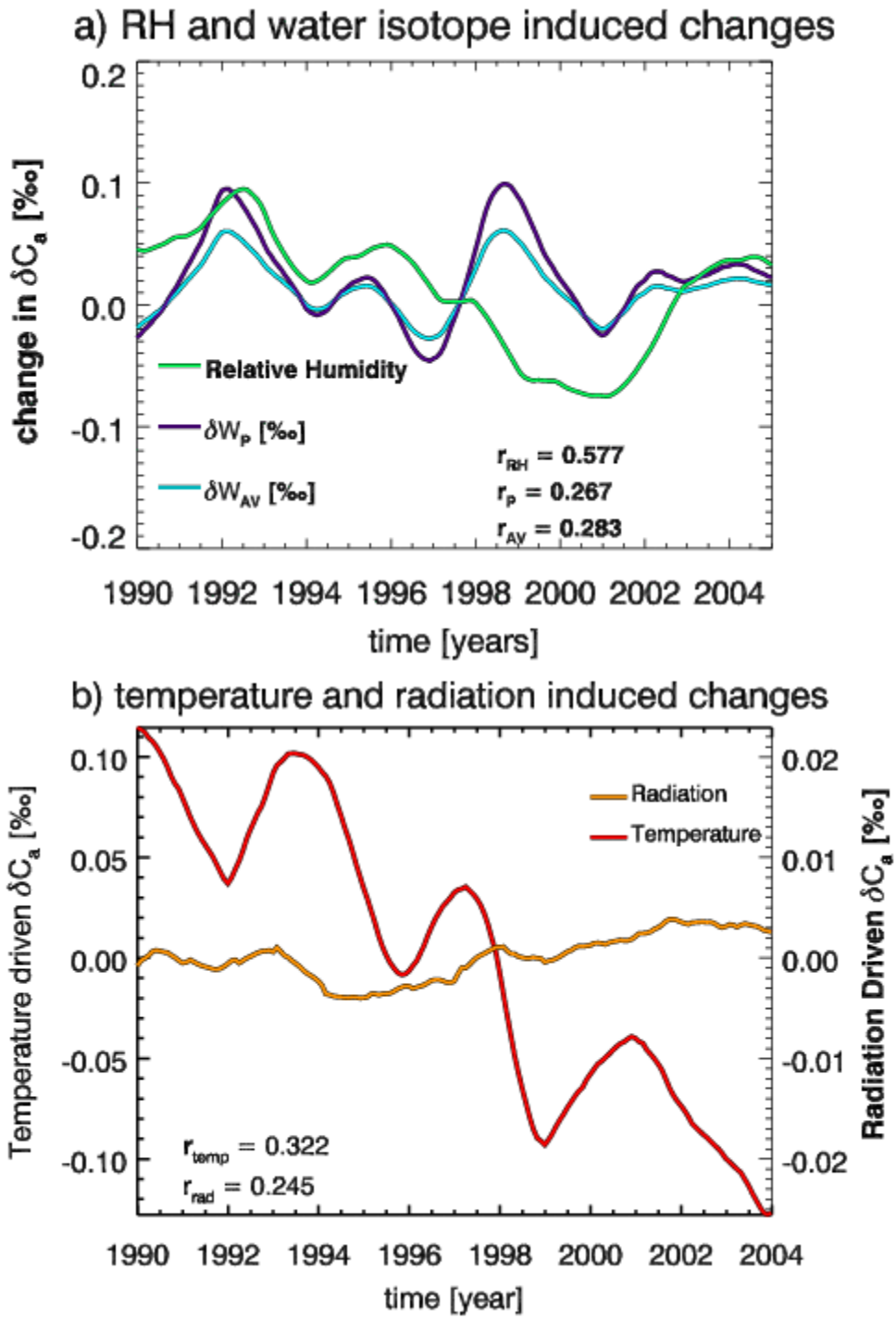

Figure 4.2. Global model results from the sensitivity experiments. The contribution from relative humidity is shown as the ALLVAR simulation (Purple line in Figure 4.1) minus the δC_a results from the experimental simulations. Correlation coefficients are found by comparing each contribution time-series with observations from Mauna Loa.

As stated above, relative humidity can affect δC_a in a number of ways that include changes to the isotopic composition of leaf and soil water and changes to ecosystem fluxes. The relative humidity variations caused the global annual photosynthesis-weighted mean of δW_l to decrease during the mid-1990s (Figure 4.3a), while global photosynthesis increased during that time period (Figure 4.3b). This is an indication that the response to relative humidity was due changes in δW_l and not increases in photosynthesis, which usually enriches atmospheric CO_2 in ^{18}O.

In the PRECCON and WVCON simulations there were no year-to-year changes in the isotopic composition of precipitation and water vapor, respectively. The simulated δC_a was subtracted from the results of the ALLVAR simulation, and the contribution from δW_P and δW_{AV} are shown in Figure 4.2a. Both δW_P and δW_{AV} contributed to the simulated decrease in δC_a during the 1990s; by 0.13‰ and 0.080‰, respectively (Figure 4.2a). These results are consistent with the magnitude estimates given in Chapter 2 and the model results presented in Chapter 3, both of which suggested that the decrease in δC_a during the 1990s was largely driven by changes to δW_P and/or δW_{AV}. Because there was no change in ecosystem CO_2 fluxes for either experiment, it can be certain that the response was completely driven by changes to the isotopic composition of leaf and soil water and subsequently δF_{la} and δF_r. Thus, these results suggest that ecosystem CO_2 fluxes may not have as large of influence on interannual δC_a variations as previously suggested [*Gillon and Yakir*, 2001; *Stern et al.*, 2001; *Ishizawa et al.* 2002]. Similar to the equilibrium results presented in Chapter 3, the model results presented here suggest that the isotopic composition of precipitation contributed more to the decrease in δC_a during the 1990s than the isotopic composition of water vapor (Figure 4.2a). Nonetheless, it is clear that the ^{18}O

content of both precipitation and water vapor can potentially have large impacts on the ^{18}O content of atmospheric CO_2.

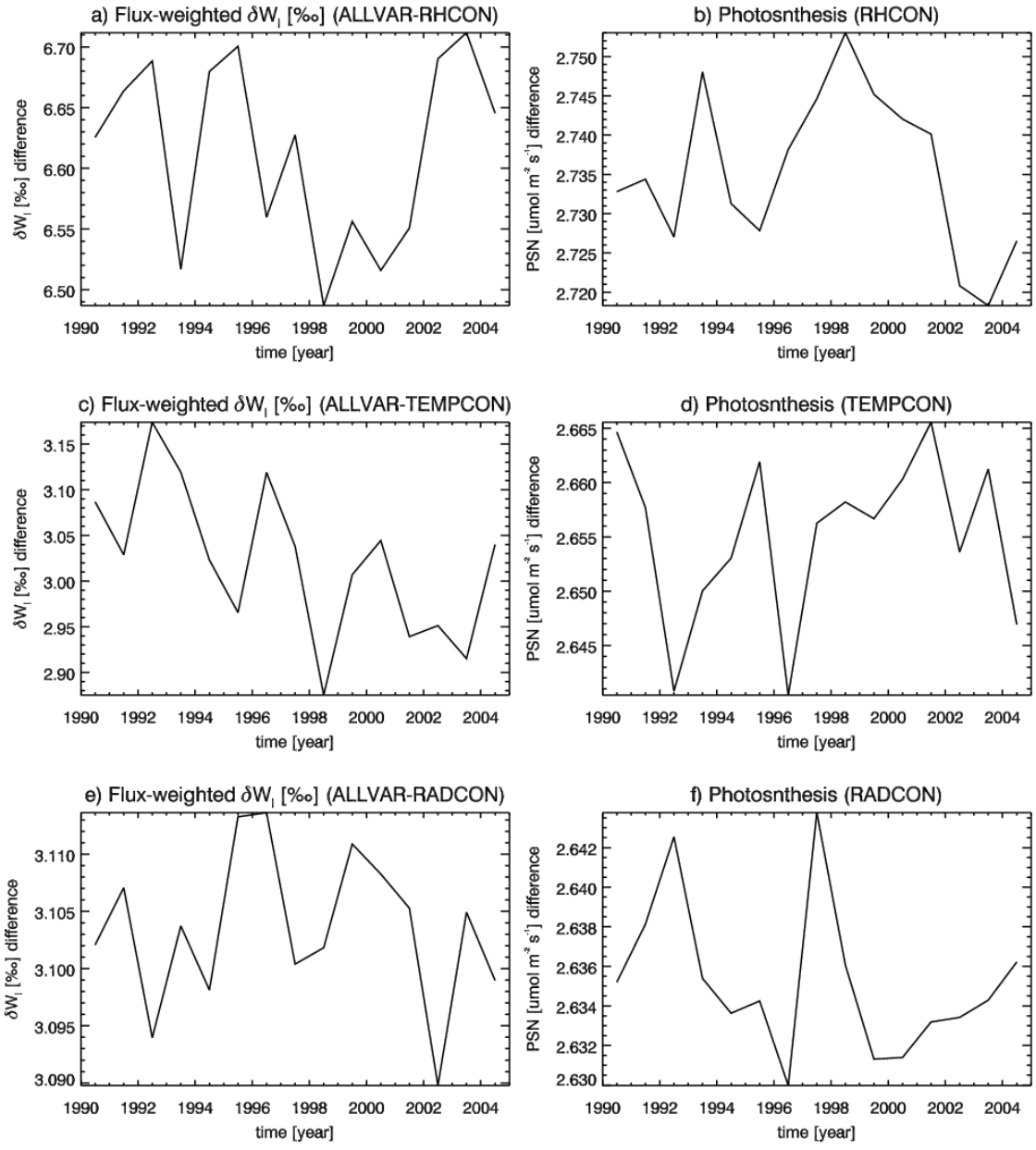

Figure 4.3. The influence of relative humidity (a and b), temperature (c and d), and radiation (e and f) on photosynthesis weighted global mean δW_l and global mean photosynthesis. Results are presented as NOVAR minus experimental simulation.

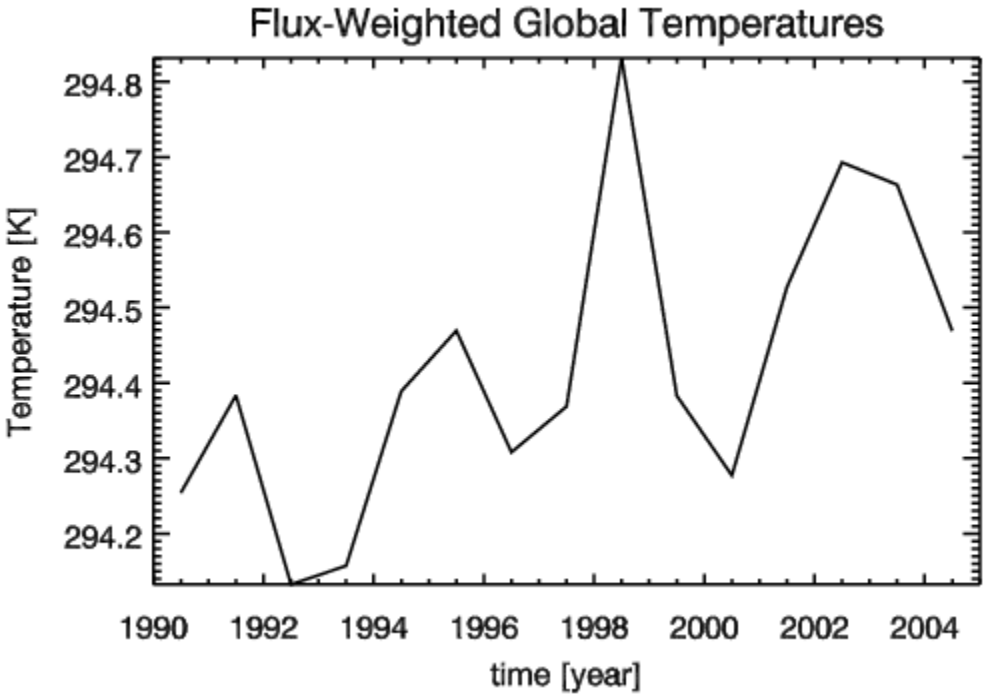

Figure 4.4. Variations in the photosynthesis-weighted global mean temperatures (K) from ISOLSM results and interpolated station data.

From 1992 to 1998, model global photosynthesis-weighted temperatures increased by about 0.70K (Figure 4.4). Results from the TEMPCON simulation suggest that the temperature increase caused a 0.30‰ decrease in global flux-weighted mean δW_l (Figure 4.3c) for the same period. As discussed in Chapter 3, this leaf water response is due to a combination of factors, such as changes to water-vapor equilibrium fractionation and increases in temperature-limited photosynthesis in the middle and high-latitudes. The temperature variations did not cause global mean photosynthesis to increase or decrease from 1992 to 1998 (Figure 4.3d), though it does increase by 0.80% from 1992 to 1995 as a result of the temperature increase. On average, temperature caused a gradual decrease in δC_a during the 1990 to 2004 period of about -0.014‰ y^{-1}, though from 1994 to 1999 temperature caused δC_a to decrease by 0.19‰. The temperature

induced changes were correlated with observed δC_a variations from Mauna Loa, and the resulting r values are shown in Figure 4.2b (r_{temp} = 0.322). The correlation was relatively low mostly because increases in temperature have caused a gradual decrease in δC_a. This result suggests that temperature was likely not the primary driver of interannual δC_a variations, though temperatures likely contributed partially to the decrease of δC_a during the mid-1990s, particularly from 1994 to 1996 (Figure 4.5).

Results from the RADVAR simulation suggest that radiation variations caused flux-weighted global mean δW_l to increase by 0.020‰ from 1992 to 1997 (Figure 4.3e). Also, the radiation variations caused a global decrease in photosynthesis of 0.048% for the same time period (Figure 4.3f). These small changes resulted in δC_a variability that was both small and inconsistent with observed δC_a variability (as is shown and reflected in the low r_{rad} value in Figure 4.2b). These results indicate that the overall influence of radiation on δC_a was small, and the observed decrease in δC_a during the 1990s was not likely a result of radiation changes (which is consistent with the previous two chapters).

4.4 Conclusion

The present study simulated the interannual δC_a variations with moderate success. The model presented here was able to accurately simulate the decrease in δC_a during the 1990s, but the increase after the year 1999 was greatly under simulated. In general, the magnitude of the simulated interannual δC_a variations was smaller than what was observed. In particular, the

simulated global decrease in δC_a during the 1990s was 0.34‰, which was about 0.16‰ lower than what was observed at Mauna Loa.

This study focused on explaining the modeled variability with sensitivity tests. If the underlying causes for the variability were similar to that of the real world, then the sensitivity tests could provide insight into the causes of the observed δC_a variations. Results from sensitivity experiments demonstrate the strong influence of the isotopic composition of precipitation and water vapor, relative humidity, and temperature on simulated interannual δC_a variations. Model results reveal that approximately 0.21‰ of the simulated decrease in δC_a during the 1990s was due to δW_P and δW_{AV}, and about 0.10‰ was due to relative humidity. Temperature may have also contributed 0.19‰ to the decrease, though the temperature induced decrease in δC_a was found to begin in 1994 (i.e., after observed δC_a began to decrease). The strong influence of the ^{18}O content of precipitation and water vapor on the ^{18}O content of atmospheric CO_2 is qualitatively consistent with the results of Chapters 2 and 3.

The results presented in this chapter reveal that the observed interannual δC_a variations were very likely a result of changes to the hydrological cycle. In particular, the model simulations suggest that interannual δC_a variations are mostly caused by interannual δW_P and/or δW_{AV} variations. This is in contrast to other studies [*Gillon and Yakir*, 2001; *Stern et al.*, 2001; *Ishizawa et al.* 2002; *Flanagan* 2005] that have suggested that interannual δC_a variations were caused by changes to ecosystem CO_2 fluxes. This work suggests that δC_a can be used as an indicator for changes in the hydrological cycle. Specifically, this work suggests that interannual δC_a variations track flux- (photosynthesis-) weighted changes in relative humidity and precipitation. For example, when the tropics go through periods of high relative humidity and

precipitation (like it did during the late 1990s), δC_a values will decrease as a result of a decrease in the ^{18}O content of leaf and soil water. Should this be the case δC_a may prove to be a powerful metric for monitoring changes in tropical hydrology.

Chapter 5

An evaluation of annual mean and seasonal timing of local and non-local processes controlling the isotopic composition of precipitation from observations and comprehensive models

5.1 Introduction

Stable isotopes in precipitation (in particular oxygen-18 and deuterium) are commonly used in studies of hydrology [e.g., *Lee et al.*, 1999; *Kendall and Coplen*, 2001; *Vachon et al.*, 2007] and past climate variability [e.g., *Dansgaard*, 1964; *Dansgaard et al.*, 1969; *Lorius et al.*, 1979; *Grootes et al.*, 1993; *Thompson et al.*, 1995]. Such studies make use of the statistical features that that precipitation becomes isotopically heavier with increasing temperature (the temperature effect) and lighter with increasing precipitation amount (the amount effect). The physical basis for the so-called temperature effect comes from the influence of temperature on the saturation vapor pressure, and preferential rain-out of the heavier isotopologue. The amount effect comes about due to the diffusive exchanges of re-evaporated precipitation with the background vapor and the recycling of vapor within convective fluxes [*Worden et al.*, 2007; *Lee et al.*, 2007; *Risi et al.*, 2008]. However, the emergence of the "effect" correlations in time-mean data need not be simple and often arises due to variations in the timing and spatial characteristics of moisture advection [e.g., *Werner et al.*, 1999; *Brown and Simmonds*, 2005; *Noone*, 2008].

These relationships between isotopic composition (hereafter denoted as δ, where $\delta = R/R_{VSMOW} - 1$, R is the heavy to light isotope ratio, and R_{VSMOW} is the Vienna Standard Mean Ocean Water ratio) and temperature or precipitation amount have been exploited by studies that aim to map the isotopic composition of precipitation from spatial data networks [*Farquhar et al.*,

1993; *Bowen and Wilkinson*, 2002; *Bowen and Revenaugh*, 2003]. *Bowen and Wilkinson* [2002] identified regions where a regression based on latitude and altitude failed to predict δ values and suggested that for some regions the misfit was due to zonal variations in vapor advection. The present study aims at expanding on this work to identify to what degree isotope equipped General Circulation Models (GCMs) are able to accurately capture the role of vapor advection on the isotopic composition of precipitation and thus determining the role of non-local processes on both δ values and deuterium excess values (d, defined as: $d = \delta D - 8\ \delta^{18}O$). This analysis aims to demonstrate the use of isotopic information to evaluate how GCMs simulate the balance of local and non-local (advective) processes within their hydrological cycles, and thereby detect shortcomings in the model hydrology via agreement with observed isotopic compositions.

In the following section, both the observational data and GCM output used for the present study are described. The balance between local and non-local influences on the isotopic composition of precipitation is evaluated by developing an empirical model and calculating the misfit with data, which is taken as a measure of the importance of non-local processes. The empirical model makes use of regressions and Fourier Transforms (hereafter, referred as the RT approach) to predict $\delta^{18}O$ and d values. Justification for the RT approach and the details of the development are given and show that in addition to providing a diagnostic tool in this study, the RT approach is useful for gap-filling spatial isotopic data to a more regular dataset. To evaluate the performance of three GCMs, the RT approach is applied to both the observational data and the model output, and the differences in the RT misfit is argued to provide a measure of the ability of GCMs to represent the role of non-local processes. The magnitude and phase of the seasonal cycle in the $\delta^{18}O$ values is evaluated and is compared to the phase of temperature and precipitation seasonal cycles, such that the misfit in time provides another measure of non-

local/or transport effects. The analysis of the seasonal cycles here will extend the work of *Bowen* [2008] and *Feng et al.* [2009], by comparing the observed cycles with those from isotope equipped GCMs. This study aims to use the isotopic simulations to offer insight as to with which components of the hydrological cycle the GCMs accurately simulate and what components need improvements.

5.2 Data and GCM simulations

5.2.1 Observational data

The observed isotopic data used here comes from the Global Network for Isotopes in Precipitation (GNIP) [Isotope Hydrology Section, 2006], a project run by both the International Atomic Energy Agency (IAEA) and the World Meteorological Organization (WMO). The GNIP database is composed of monthly mean δD and $\delta^{18}O$ measurements from about 850 stations around the globe. Along with geographic position and station altitude, the dataset also reports precipitation amount, surface air temperature, and vapor pressure. Long-term mass weighted monthly means are calculated for the 1961-2005 period, and the stations that are included in the means have at least one-year of measurements on record. The latest release of the GNIP data includes many more stations in regions where records had previously been sparse, especially in Siberia and Antarctica. The density of the stations is shown in Figure 5.1 as a probability distribution, and with most of the stations located on continents. In particular, many of the stations are located in Europe, and to a lesser degree Southeast Asia, Canada, and Central/South America. It should be noted that a regression model based on these data will, in turn, be biased towards these continental regions. Furthermore, certain stations report some values that are

unreasonable ($\delta^{18}O$ values lower than -80‰, and d values outside the range -20‰ to 35‰), which are excluded, as are records that do not include temperature and precipitation data.

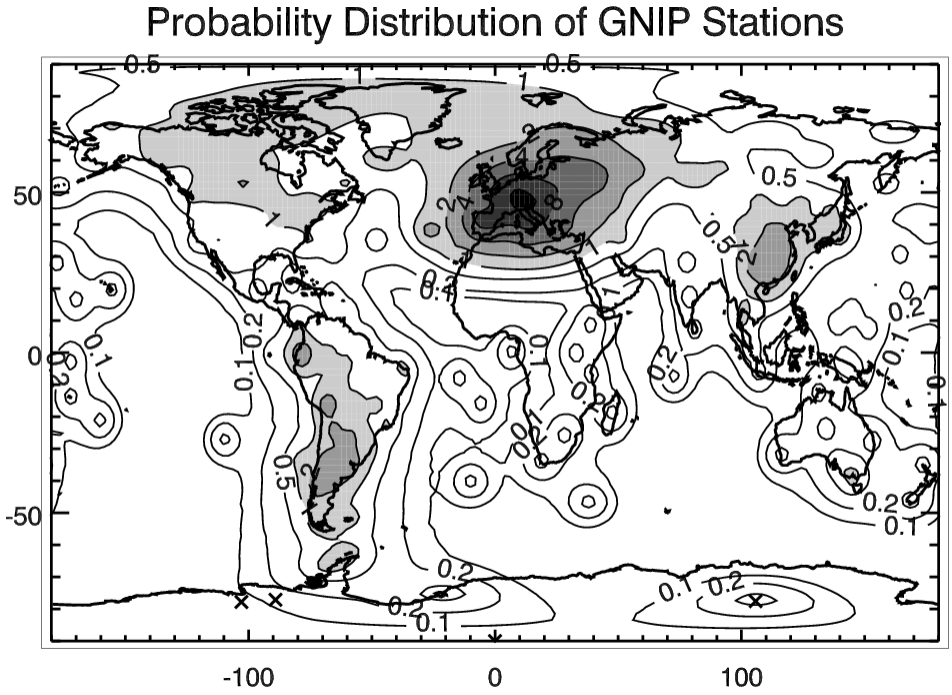

Figure 5.1. Probability density of GNIP stations derived as the total weights from equation (B1) in units of station probability per 10^6 km^2. The global integral equals the number of stations and is 298. Contours are given at 0.1, 0.2, 0.5, 1, 2, 4, 8, and 16×10^6 km^{-2}. Stations added to the GNIP archive for the analysis here are shown as an "X".

Four Antarctic ice cores are added to the dataset that are not part of the GNIP database (indicated by an 'X' in Figure 5.1). These are located near the South Pole [*Mayewski and Whitlow*, 2000], one in east Antarctica [*Mirny and Vostok* B37; *Ekaykin et al.*, 2001; *Lipenkov et al.*, 1998] and two in west Antarctica [ITASE 2001-2 and 2001-5; *Steig et al.*, 2005], and each has sub-annual resolution. Although many more values from Antarctic ice cores exist [e.g., *Schneider and Noone*, 2007; *Masson-Delmotte et al.*, 2008], I choose to include only four so that the global regression model is not unfairly biased toward the polar region. The addition of these ice cores results in a total of 298 stations used in the analysis below.

The regression models presented here require gridded datasets of elevation, temperature, and precipitation, interpolated onto the nominal working grid (2° longitude x 2° latitude). Elevation data were taken from a revised version of terrain height data originally prepared at the Scripps Institute of Oceanography [*Gates and Nelson*, 1975]. The National Center for Environmental Prediction (NCEP) and National Center for Atmospheric Research (NCAR) Reanalysis [*Kalnay et al.*, 1996] were used to obtain the spatial and temporal distribution of surface air temperature (data provided by the NOAA/OAR/ESRL PSD, Boulder, Colorado, USA, http://www.cdc.noaa.gov/). Long-term mean precipitation data were taken from the Climate Prediction Center Merged Analysis of Precipitation (CMAP) [*Xie and Arking*, 1997].

5.2.2 General Circulation Model results

To evaluate the fidelity of isotope simulations, three GCMs with isotope tracers are used in both the regression analysis and the seasonal cycle evaluation. These models include the Melbourne University General Circulation Model (MUGCM), the European Centre Hamburg Model (ECHAM), and the Goddard Institute for Space Studies model (GISS) [*Joussaume et al.*, 1984; *Jouzel et al.*, 1987; *Hoffmann et al.*, 1998; *Noone and Simmonds*, 2002]. These models participated in the first isotope intercomparison experiment of the IAEA/GEWEX Stable Water Isotope Intercomparison Group (SWING) [Werner et al., 2004; Noone, 2006].

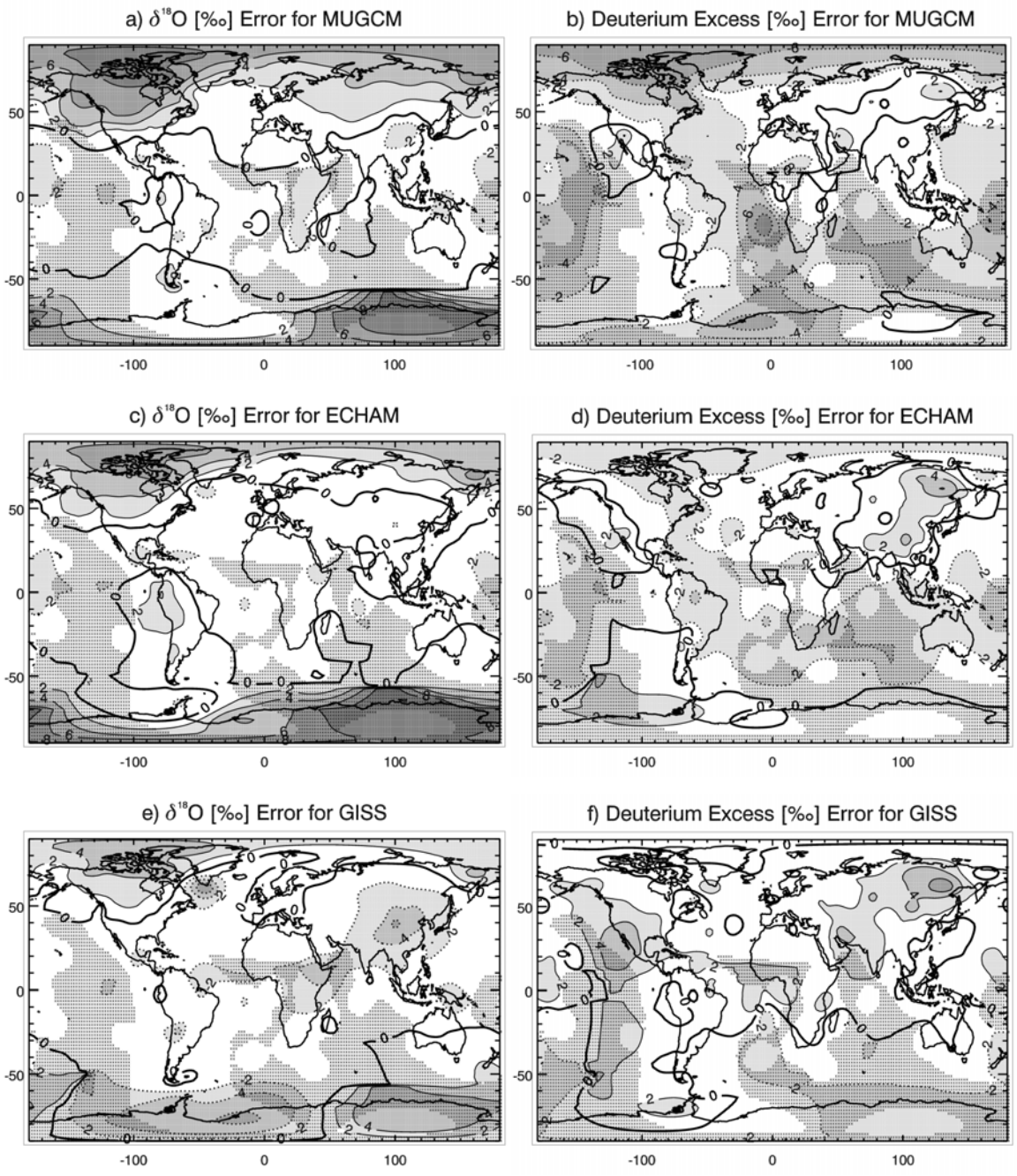

Figure 5.2. GCM simulated error in annual mean values of $\delta^{18}O$ (a, c, and e) and *d* (b, d, and f), using the closest grid cell to each station and interpolated onto a 2° x 2° grid. The models are MUGCM (a and b), ECHAM (c and d), and GISS (e and f). Units are in ‰ and contour intervals are 2‰. Solid lines indicate positive values and dotted lines indicate negative values. Gray shading indicates region where the absolute value of the error is above 2‰, and stippling indicates regions where observational data are sparse (station probability is less than 0.1×10^{-6} km $^{-2}$).

It is useful to point out the skill with which GCMs reproduce δ and d values. The GCM error is calculated by choosing the closest grid cell for each GNIP station, taking the difference, and interpolating the difference onto a grid for visualization of results (see Appendix B). Figure 3.2 shows the GCMs perform fairly well at predicting δ values in the tropics and subtropics (particularly over oceans), but begin to diverge from the observations in the mid to high-latitudes where simulated δ values are not low enough. The MUGCM has the largest error in the high northern latitudes, and GISS has the lowest. However, GISS predicts the values to be too depleted throughout the southern high latitudes, unlike ECHAM which simulates values that are not depleted enough in the high latitudes of both hemispheres. All three GCM results generally simulate d values that are too high in the Southern Ocean and western North America and values that are too low over much of the Asia. Given these errors, this study will use regressions to test if the models are simulating the correct hydrological influences (i.e. those correlated with local temperature and precipitation, and non-local processes) that ultimately dictate the distribution of the isotopes.

5.3 Construction of a regression/transform approach

The spatial and temporal variations in $\delta^{18}O$, δD, and d, are represented by an empirical fit that is composed of three components: the annual mean, seasonal anomaly, and model bias. At each position on some grid, denoted by longitude and latitude positions (λ, ϕ), the final values (δ_f) are computed as a function of time (t, months) and are found via the summation of three independent components:

$$\delta_f(\lambda,\phi,t) = \left[\delta_a(\lambda,\phi) + \delta_m(\lambda,\phi,t)\right] - \varepsilon_1(\lambda,\phi,t) \qquad (5.1)$$

where δ_a is the stationary annual mean (predicted by a regression), δ_m is the monthly variation for a climatological year, and ε_1 is a bias correction that captures physics not explained by the regression and is the mismatch between the regression and the observations (i.e. the regression residual also used by *Bowen and Wilkinson* [2002]).

The annual mean term in (1) is calculated as a spatial regression, such that

$$\delta_a = a_1 T + a_2 T^2 + a_3 \sqrt{P} + a_4 P^2 + a_5 Z + a_6 |\phi| + a_7 , \qquad (5.2)$$

where T (K) is annual mean temperature, P (mm month^{-1}) is annual mean monthly precipitation, Z (m) is elevation, and a values are regression coefficients used to fit the station data. These particular variables were chosen via a stepwise multiple regression approach (see Appendix A). The mean seasonal cycle, δ_m, is evaluated by taking a Fourier transform of the data at each GNIP station, interpolating the first four harmonic coefficients (cf. two harmonics used by *Feng et al.* [2009]) onto a grid, and finally performing the inverse transform. This Fourier fitting method is found to produce more reliable predictions of the annual cycle in data sparse regions because it retains the out-of-phase relationships with temperature and precipitation that are lost in a regression approach.

There is some bias (full model residual) associated with the model misfit, and evaluated as

$$\varepsilon_1 = (\delta_a + \delta_m) - \delta_O , \qquad (5.3)$$

where δ_O is the observed monthly mean at each station. The bias term is then interpolated onto a grid, so that an estimate of the bias field exists for each month of the 12 months. The physical significance of the bias terms is that it measures the variability in isotopic composition not associated with physics captured by the predictors (particularly local temperature and

precipitation), and is a quantity of intrinsic interest in the analysis below because it is dominated by non-local influences.

5.4 Evaluation of the biases in the annual mean

The regression fits the spatial distribution of the annual mean station observations of $\delta^{18}O$ values remarkably well, with a fitting correlation value of $r_{fit} = 0.932$. Cross-validation is done by removing each station when calculating regression coefficients; the coefficients are then used to predict the observed value of the removed station. This method generates another set of correlation coefficients that measures the regression's predictive capability [*Michaelson*, 1987]. The predictive correlation for the RT approach is $r_{predict} = 0.917$ (or 84% of the variance), which is only slightly less than the r_{fit} fitting value, and a reminder that there is clear spatial structure in the isotope fields. Removing the zonal means (taken in 10° latitude bins) gives much smaller correlation coefficients: $\acute{r}_{fit} = 0.765$ and $\acute{r}_{predict} = 0.747$ (or 56% of the variance), which indicates that much of the predictive skill comes from the very strong latitudinal gradient poleward of the subtropics. For deuterium excess (d) the correlations show significantly less skill ($r_{fit} = 0.410$ and $r_{predict} = 0.368$) and show that the controls on the kinetic fractionation that yields d values are more complicated.

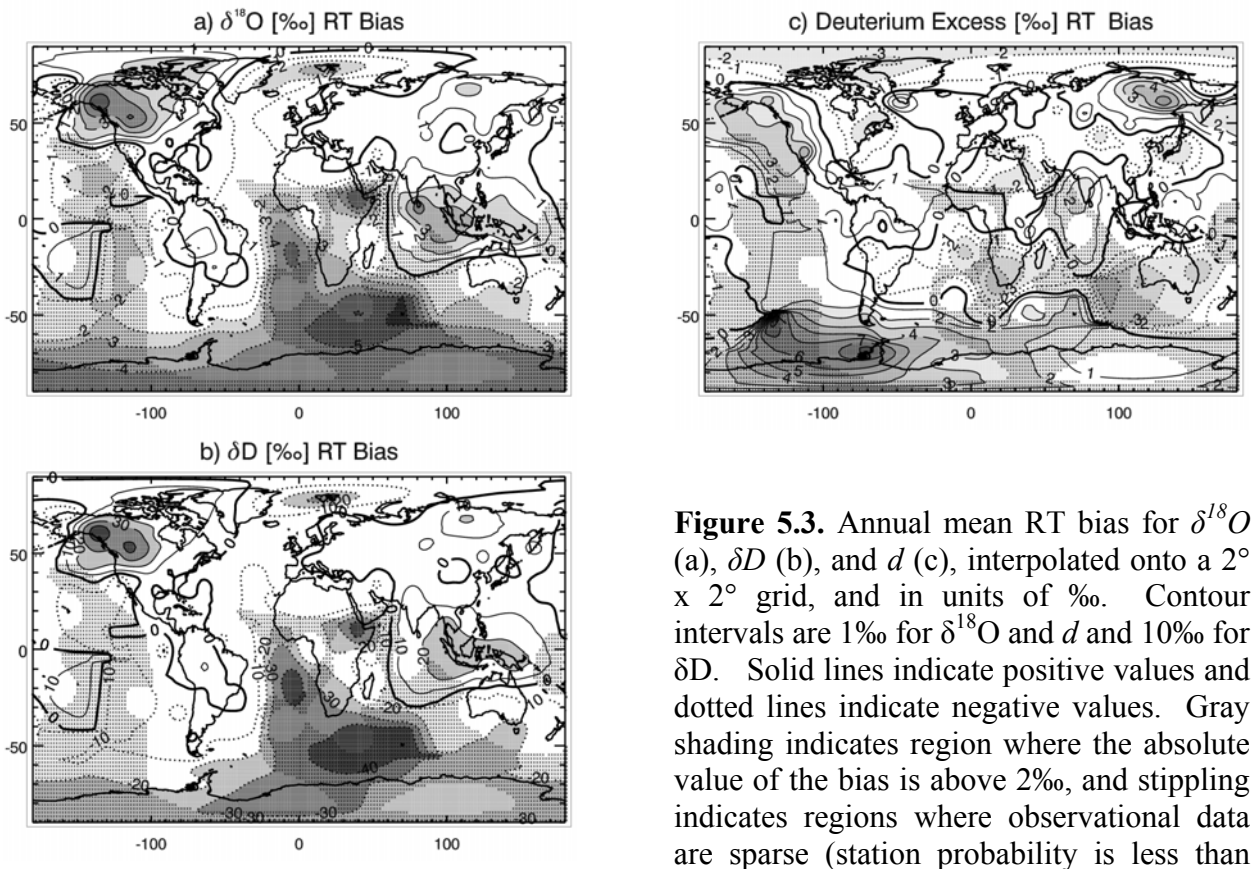

Figure 5.3. Annual mean RT bias for $\delta^{18}O$ (a), δD (b), and d (c), interpolated onto a 2° x 2° grid, and in units of ‰. Contour intervals are 1‰ for $\delta^{18}O$ and d and 10‰ for δD. Solid lines indicate positive values and dotted lines indicate negative values. Gray shading indicates region where the absolute value of the bias is above 2‰, and stippling indicates regions where observational data are sparse (station probability is less than 0.1×10^{-6} km^{-2}).

Figure 5.3 shows the annual mean of the bias term (ε_1) in the RT approach for $\delta^{18}O$, δD and d values (found independently of the two δ values). The model bias has a root mean square value of 2.20‰ for $\delta^{18}O$, 18.2‰ for δD, and 2.89‰ for d; however, the regression performs poorly at certain locations and results in large magnitude biases. The $\delta^{18}O$ and δD patterns largely reaffirm the similar work of *Bowen and Wilkinson* [2002], and are presented here to facilitate discussion of the bias derived from the GCM-based regressions. The RT bias is large where there is a strong influence associated with non-local processes (i.e. largely affected by transport as described by *Bowen and Wilkinson* [2002]) not captured by local predictors and thus

I define this as a measure of non-local influences. The regression predicts both $\delta^{18}O$ and δD values to be too low over the Southern Ocean, over eastern Africa, and over the Arctic Ocean north of Scandinavia. However, as stippling in Figure 5.3 indicates, there are certain regions of the Southern Ocean where data are too sparse for the RT approach to be well constrained. Over most of Canada and Alaska, the regression predicts both $\delta^{18}O$ and δD values that are not depleted enough. These large biases can be explained by differences in vapor transport within the latitudinal zones. For example, vapor in the North Atlantic (where temperatures are high) are advected northeastward towards the Arctic Ocean where the resulting rain will be enriched in the heavy isotopes compared to other locations within the latitudinal zone. A similar argument for significant biases found in a different regression model was also given by *Bowen and Wilkinson* [2002].

Biases in deuterium excess values, *d*, show a different distribution. The magnitude of the bias is large (and positive) over the Antarctica Peninsula and a large portion of Russia. The western coast of North America and the southern tip of Greenland are also regions where the biases are large, which is likely due to omission of the most relevant predictors of the *d* values in the regression for these locations. For instance, *Vimeux et al.* [2001] suggest SSTs, sea ice conditions, and relative humidity over the source water region are highly correlated with *d* values, which are absent in the RT approach used here.

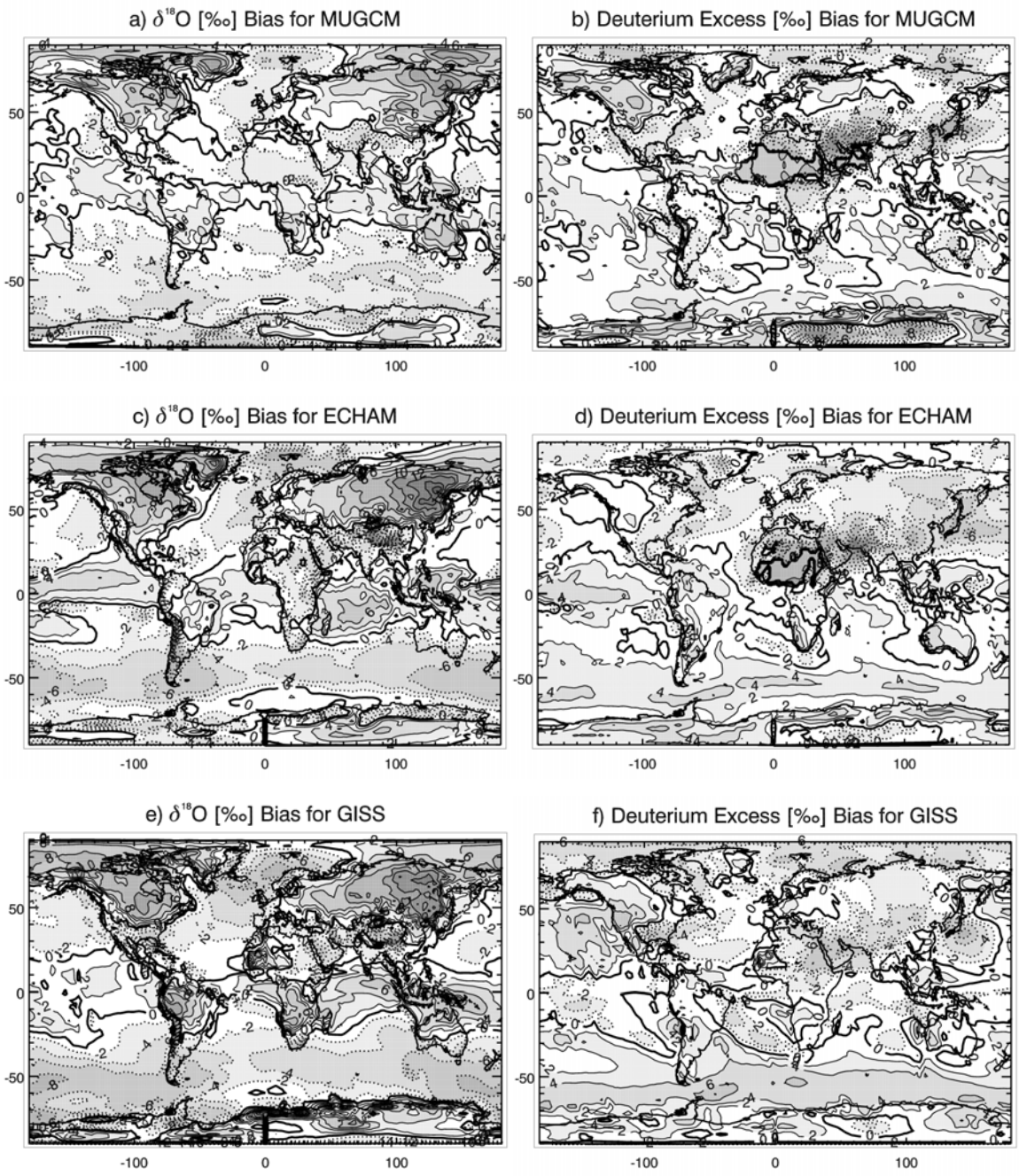

Figure 5.4. Annual mean GCM bias for $\delta^{18}O$ (a, c, and e), and *d* (b, d, and f) values, and in units of ‰. Contour intervals are 2‰. The models are MUGCM (a and b), ECHAM (c and d), and GISS (e and f). Solid lines indicate positive values and dotted lines indicate negative values. Gray shading indicates region where the absolute value of the bias is above 2‰.

To assess the degree to which the GCM errors described above are due to a failure in simulating the balance between local and non-local processes, regression models were established based on the GCM output rather than the GNIP observations. The GCM $\delta^{18}O$ values are "predicted" by applying equation (2) to the simulated fields, and the bias relative to the GCM simulated $\delta^{18}O$ values are computed. Figure 5.4 shows that many of the biases that appeared in the observationally based regression also appear in the regressions based on GCM output; however, the magnitudes and geographic extent differ in detail. For example, all four of the $\delta^{18}O$ regression biases are large and positive in northern Canada; though, the GCM-based biases are higher in the eastern portion of the continent and are generally large throughout the high and mid northern latitudes. This indicates that the GCMs inadequately simulate the non-local controls of the hydrological cycle for the northern continents. Furthermore, the observational and GCM-based regressions all have negative biases in the Southern Ocean. However, the extent and magnitude of this bias over the oceans is much greater than the observational-based regression (with the exception of the regions adjacent to Africa). Similarly, there is a region in the Arctic Ocean north of Scandinavia that also has large negative bias for both the observational-based and GCM-based regressions. As noted above, this bias is suspected to be due to moisture transport from lower latitudes, and is a feature of the hydrological cycle that the models over-emphasize. The models' overemphasis of these non-local processes is likely responsible for the model errors in $\delta^{18}O$ values within the mid and high high-latitudes (Figure 5.2). In other words, the models overemphasize the role of large-scale transport in the simulation of the hydrologiocal cycle. These findings also suggest that the role of local cloud processes is modeled to be less important than is suggested by the observed isotopes in precipitation. As such, these three GCMs give a

misleading view of the atmospheric hydrology as being (overly) dominated by dynamical controls rather than cloud microphysical controls.

Similar results emerge in the *d* value regressions; however, *d* values are believed to be largely affected by non-local meteorological conditions (specifically conditions over the source region), so differences between observed and GCM biases could be due to incorrect source region and/or non-local meteorological conditions within correct regions. For instance, the GCMs simulate *d* values that are too high (positive errors) over Siberia and much of Asia, with MUGCM being a slight exception (Figure 5.2). The observational-based regression has large positive biases for this region, indicating that the non-local influence act to lower *d* values in this region. On the other hand, the GCMs all have large negative biases over much of Asia, which indicates that the non-local influence causes *d* values to increase (and not decrease as the observation-based bias would suggest). This non-local increase in *d* values could be the cause for simulated values that are too high when compared to observations. There could be a number of causes of these improper simulations. For example, in the GCM simulations, the vapor over Asia could be derived from waters with higher sea surface temperatures or waters in more arid regions than those actually occurring in nature. However, it is important to note that while MUGCM has a smaller negative bias over Asia, which is similarly reflected in the smaller model errors in the region, it is unlikely that the simulation of the regional hydrology is perfect.

Within the GCMs, $\delta^{18}O$ and *d* values are known quantities at each grid-cell, and yet the regression approach has significant bias for many regions. This implies that although regression-type of mapping gives reasonable qualitative similarity, the use of temperature and precipitation as predictors has significant quantitative limitations, especially for *d* values. This is because of both the strong non-local influences and physical dependence of *d* on other quantities. Because *d*

values are not as well predicted using the RT approach, the following section focuses on $\delta^{18}O$ values only.

5.5 Controls on the seasonal cycle

Figure 5.5 compares observed seasonal cycles in $\delta^{18}O$ values for six representative stations with those produced by the RT approach. Also shown are simulated $\delta^{18}O$ values from the SWING GCMs (using the three model mean), a case where the RT approach excludes the bias term, and a case when the station of interest is removed from the fitting to illustrate the cross-validation. GCM and RT values use the nearest grid cell for the comparison. The RT approach in its complete form is able to capture both the phase and amplitude of the seasonal cycle for five of the six stations (Reykjavik, Iceland being the exclusion). Furthermore, when the bias term is removed from the RT approach, the phase and amplitude of the seasonal cycle change little. The GCM mean and RT prediction (station of interest removed for cross-validation) curves are similar in a number of respects. In the mid-latitudes (Vienna, Ottawa, and Melbourne), the models adequately predict the phase and amplitude of the seasonal cycle (for both hemispheres). However, in the tropics and high-latitudes both the RT approach prediction and the GCM mean are less capable of predicting the phase and (especially) the amplitude well. Thus, there must be some component of the seasonal variation in the hydrological cycle that the models are not accurately capturing at these locations. Given the local nature of the RT approach, this is likely to be from shortcomings in rainfall recycling or seasonal moisture transport.

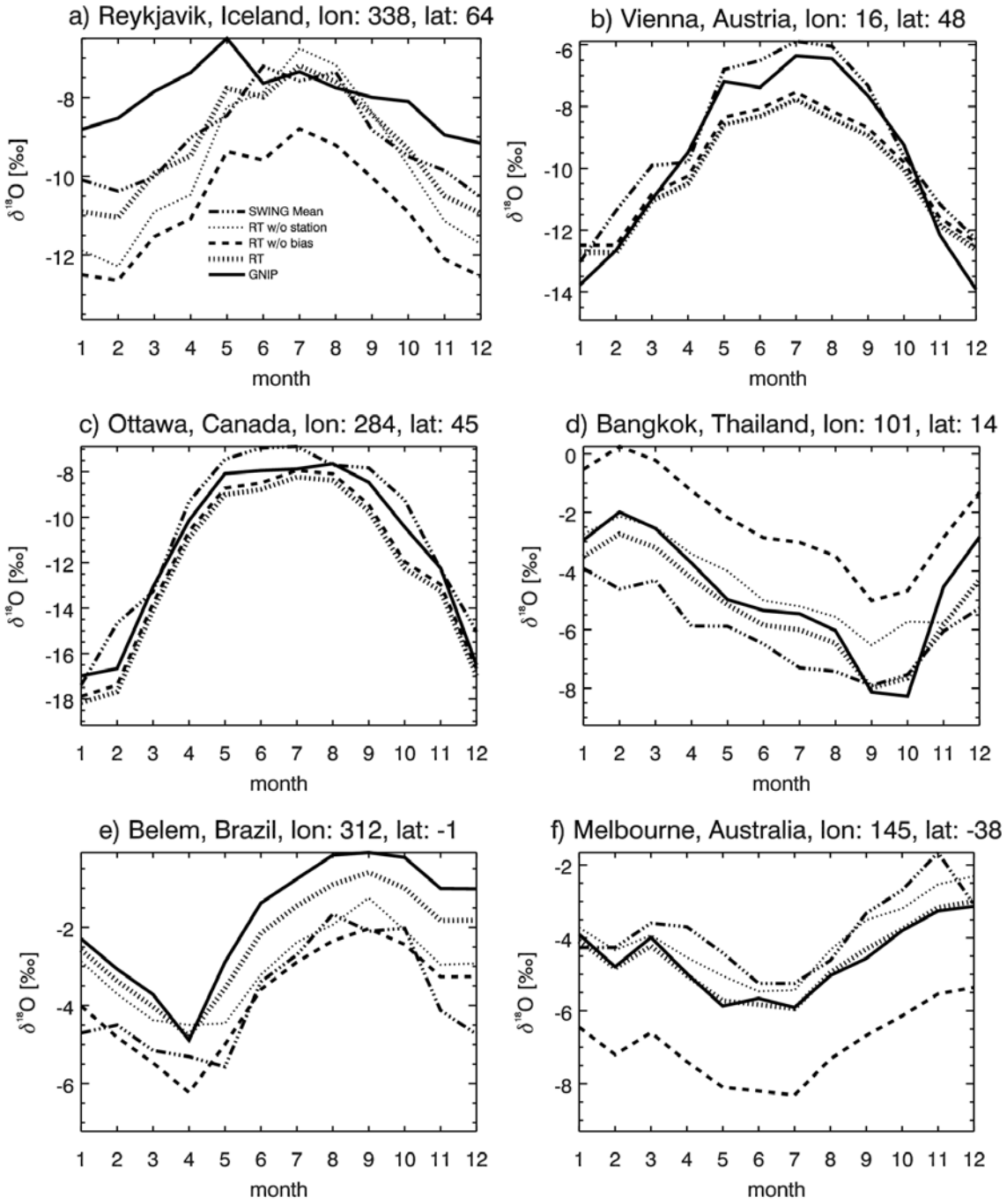

Figure 5.5. Seasonal cycles of $\delta^{18}O$ for the GNIP observations (solid line) and the SWING GCM means (dash dotted line) for six separate regions: a) Reykjavik, b) Vienna, c) Ottawa, d) Bangkok, e) Belem, and f) Melbourne. Also plotted is the RT approach using all of the stations (thick dotted line) and using all but the given station in the regression and transform (dashed), and without the bias term (dashed line).

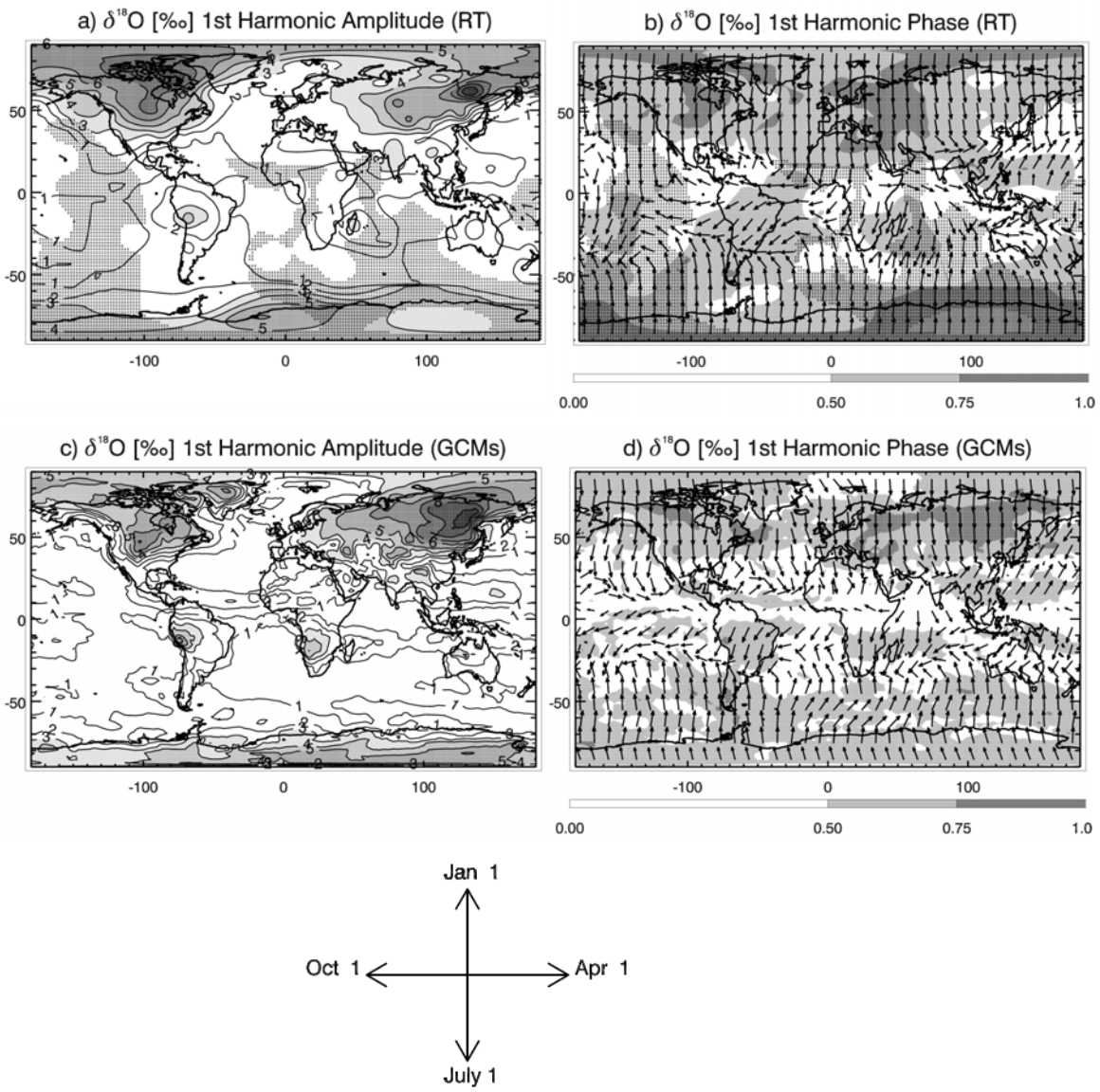

Figure 5.6. Spatial distribution of the amplitude (a, c) and phase (b, d) of the 1st harmonic in the $\delta^{18}O$ seasonal cycle from the RT approach and GCM mean. Contours of the phase plots indicate the fraction of the total amplitude explained by the 1st harmonic. Phases are represented by arrows that are oriented such that the angle relative to north indicates the phase of the harmonic. Bottom key is used to determine the phase in terms of the month of maximum value. The amplitude is half of the difference between maximum and minimum values. Stippling in a and b indicates regions where observational data are sparse (station probability is less than.0.1×10^{-6} km^{-2}).

5.5.1 Physical drivers of seasonality in the 1st harmonic

The geographic variations in the shapes of the seasonal cycle predicted by the RT approach and simulated by the GCMs are established in Figure 5.6, which shows the spatial distribution of the amplitude and phase of the 1st harmonics of the seasonal cycle. Although the amplitude and phase of the 1st harmonic have been shown by others [*Bowen*, 2008; *Feng et al.*, 2009], I focus here on evaluating the simulated seasonal distribution relative to that which is captured by GNIP observations. The observed amplitude of the 1st harmonic is largest in the mid and high-latitudes and over continents, which is believed to be a result of the temperature effect and large seasonal temperature variations. In the U.S., the amplitude of the 1st harmonic is largest in the interior of the country (i.e. the Midwest and along the Rocky Mountains) and decreases towards the coasts, a result that is consistent with findings of *Vachon et al.* [2007] and *Bowen* [2008]. GCM simulations also capture these high amplitude regions in the mid and high-latitudes, though the amplitudes are typically smaller in the GCM simulations (Figure 5.6). Because the models generally capture the geographic areas with high amplitudes in temperature it is likely that the subsequent seasonal influence on isotopic rainout in the mid and high-latitudes can be considered robust, albeit of reduced amplitude in the models.

Although observed amplitudes are smaller within the tropics there are still many regions where the 1st harmonic contributes more than half (shading in Figure 5.6b) of the total amplitude (e.g., much of South America, Southeast Asia, and a region centered on Madagascar). The largest observed 1st harmonic amplitude within the tropics is on the east coast of South America, which is a feature that the GCMs simulate remarkably well. The models also simulate a high amplitude region in southwestern Africa. This does not appear in the RT results due to lack of data within this region, an indication of the need for more isotope measurements within the

global network. Because this feature over Africa is geographically similar to the one over South America, it is likely real. Both high amplitude regions do not have unusually large amplitudes in precipitation amount (not shown), which suggests that the high amplitudes could be largely due to shifts in wind and water source regions, a result consistent with the findings of *Feng et al.* [2009].

To better understand the degree to which temperature and precipitation correlations accurately explain the underlying thermal and hydrological controls on variations in both the observed and simulated seasonal cycle of $\delta^{18}O$ values, the differences in the phases between $\delta^{18}O$ values and both temperature and precipitation amount are plotted in Figure 5.7. These can be considered in relation to the phase of the leading harmonic of $\delta^{18}O$ alone shown in Figures 5.6b and 5.6d. In the mid and high-latitudes, the observed phase of the 1st harmonic is such that the maximum is in July in the Northern Hemisphere and January in the Southern Hemisphere, and indicative of the dominating role of seasonal temperature variations. However, in the Northern Hemisphere oceans the $\delta^{18}O$ values leads by 1-2 months because temperature maxima are typically later in the summer. Similarly in the Southern Hemisphere, the phase of the 1st harmonic in $\delta^{18}O$ values begins to diverge from the phase of temperature, suggesting that other processes are playing a role in the seasonal cycle. For instance, changes in cloud processes (perhaps linked to precipitation amount), storm track position and strength, and advection pathways from the source region would all give rise to phase offsets. Some aspects of these mechanisms were explored recently and shown by *Feng et al.* [2009] in the context of seasonal changes in the position and strength of the Intertropical Convergence Zone, and a moisture source in the region of subtropical highs. The GCMs simulate $\delta^{18}O$ values that are in phase with temperature over land, and slightly lead over the ocean (in the 1st harmonic). This is consistent

with the RT results and associated with the strong temperature control on saturation and isotopic rainout in mid and high-latitudes that gives rise to the temperature effect in both spatial and temporal data.

Table 5.1. Average phase lead of the precipitation maximum with $\delta^{18}O$ minimum in the 1st harmonic (lags are negative). Average phase lead of the precipitation maximum with $\delta^{18}O$ maximum in the 2nd harmonic. Bold numbers show statistical significance at the 90% level.

	1st harmonic (anti-phase)			***2nd harmonic (in phase)***		
Region	*RT*[1]	*GCM*[1]	*RT-GCM*[1]	*RT*[1]	*GCM*[1]	*RT-GCM*[1]
Pacific Ocean[2]	8.5 (5.6)	**-7.6 (3.0)**	**16.1 (2.6)**	-6.9 (4.9)	**-24 (0.92)**	**17.1 (3.5)**
South America[3]	6.6 (5.5)	-1.3 (2.0)	7.9 (3.5)	**-17 (4.1)**	**-15 (0.66)**	-2 (3.1)
Atlantic Ocean[4]	**-46 (16)**	-7.4 (5.6)	-39 (10)	**-41 (21)**	**-15 (1.6)**	-26 (22)
Africa[5]	15 (23)	**-17 (5.4)**	**32 (18)**	**-17 (10)**	**-27 (1.9)**	10 (10)
Indian Ocean[6]	**16 (4.8)**	**30 (3.8)**	**-14 (1.0)**	**-20 (10)**	0.16 (1.1)	**-20 (8)**
SE Asia[7]	2.7 (8.9)	-12 (5.7)	**15 (3.2)**	**-29 (9.1)**	**10 (1.8)**	**-39 (7.3)**
Total[8]	1.3 (4.8)	**-2.1 (1.7)**	3.4 (3.1)	**-23 (4.1)**	**-15 (0.58)**	**-8 (3.5)**

[1]Unit in days, standard deviation in parenthesis

[2]From 15°S to 15°N and 150°E to 280°E

[3]From 15°S to 15°N and 280°E to 330°E

[4]From 15°S to 15°N and 330°E to 10°E

[5]From 15°S to 15°N and 10°E to 55°E

[6]From 15°S to 15°N and 55°E to 110°E

[7]From 15°S to 15°N and 110°E to 150°E

[8]From 15°S to 15°N

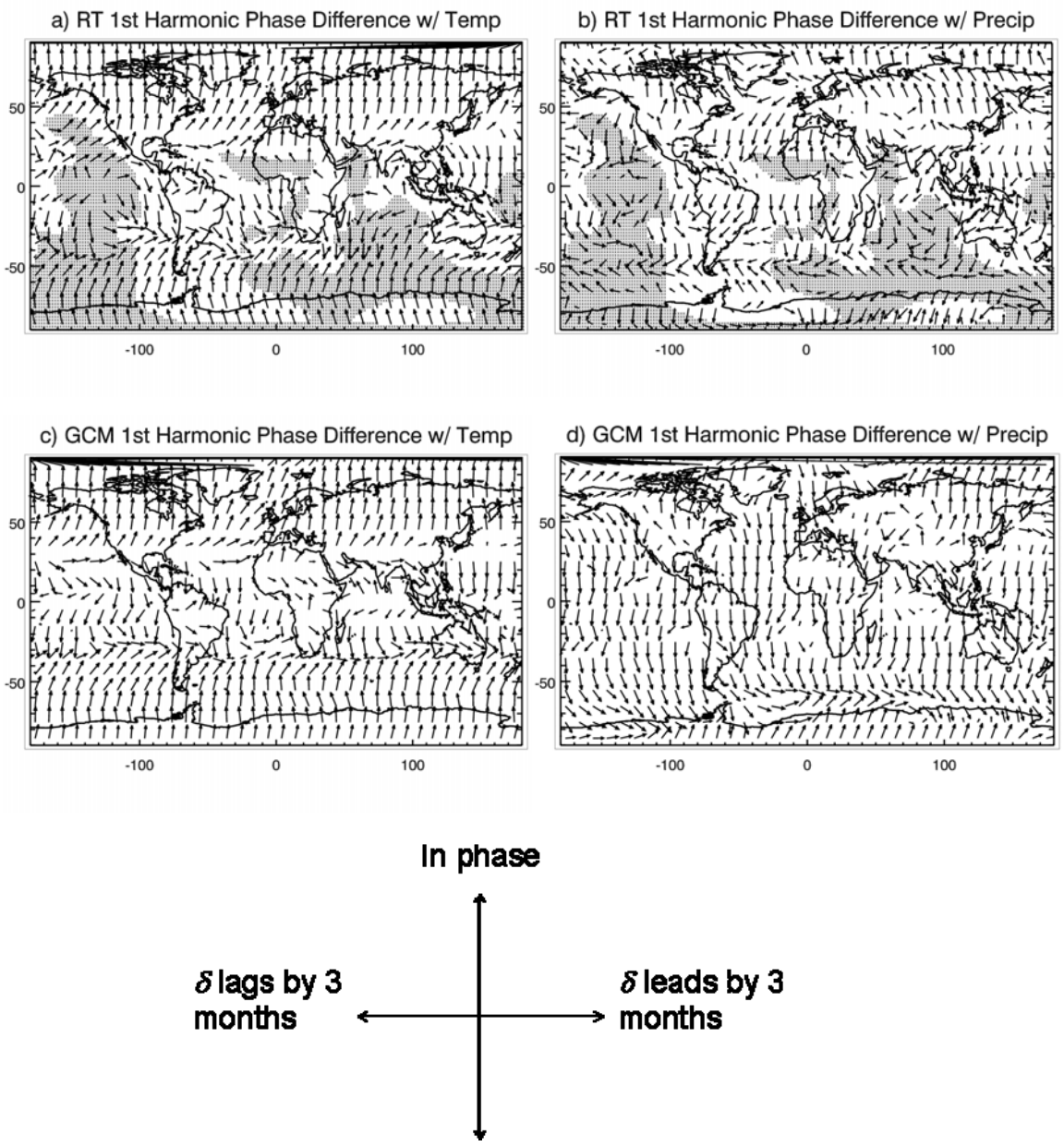

Figure 5.7. Spatial distribution of the phase differences of the 1st harmonic between $\delta^{18}O$ values and temperature (a and c) and precipitation (b and d) seasonal cycles from the RT approach and GCM mean. Phase differences are represented by arrows that are oriented such that the angle relative to north indicates the extent to which the two variables are out of phase. Stippling in a and b indicates regions where observational data are sparse (station probability is less than.0.1×10^{-6} km^{-2}).

Within the tropics and subtropics, precipitation amounts are believed to be the most prominent predictor in determining the phase of the seasonal cycle in $\delta^{18}O$ values [*Noone and Simmonds*, 2002; *Bowen*, 2008]. Indeed, for the regions within the tropics where the 1st harmonic is considerably large (e.g., South America, Southeast Asia, and Madagascar), it is found here that both the observed and simulated phase of the 1st harmonic in $\delta^{18}O$ values appears to be mostly in anti-phase with the 1st harmonic phase in precipitation.

Table 5.1 shows phase differences between precipitation maximum and the $\delta^{18}O$ minimum for various tropical regions. Statistical significance in these differences are found via a Monte Carlo method, where the RT approach is applied after 50 random stations (or 2700 grid cells from model output) are removed; phase differences are then calculated, and the process is repeated 10,000. The phase differences that are larger than 1.645 standard deviations (for a given regions) of the 10,000 samples are viewed as significant at the 90% level. Within the entire tropics (between 15°S and 15°N,), the precipitation maximum typically leads the $\delta^{18}O$ minimum by only 1.3 day using the RT approach, while the GCMs simulate the maximum lagging by 2.1 days. Both values are lower than the significance threshold, and the two variables can be viewed as in anti-phase with one another within the tropics (in both observations and GCMs). These findings are consistent with an explanation of the variability in terms of the statistical relationship described as the amount effect.

When examining particular regions of the tropics, the leads and lags become larger. Over the Indian Ocean the precipitation maximum leads the $\delta^{18}O$ minimum by 16 days (Table 5.1), which is likely a result of local cloud processes that are typically attributed to the negative correlation between precipitation amount and $\delta^{18}O$ values [*Worden et al.*, 2007; *Lee et al.*, 2007; *Risi et al.*, 2008]. On the other hand, over the Atlantic, the maximum in precipitation lags the

$\delta^{18}O$ minimum by 46 days, and could be result of a change in the advective origin of the moisture within the region, a result that is consistent with the findings of *Feng et al.* [2009]. Despite these possible dissimilar mechanisms, the seasonal temperature and amount effect appear to be consistent with the phase of the 1st harmonic of the seasonal cycle in $\delta^{18}O$ values within the tropics.

The GCMs simulate leads and lags that are somewhat inconsistent with those found from the RT approach. For example, over Africa, the GCMs simulate the precipitation maximum lagging the $\delta^{18}O$ minimum by 17 days, while the RT approach has the precipitation maximum leading the $\delta^{18}O$ minimum by 15 days. These types of inconsistencies are likely a result of improper simulations of the physical processes (advective or cloud processes) that lead to the amount effect. As such this analysis suggests that these processes are a specific shortcoming that should be resolved in the GCMs, in order to properly simulate the hydrological cycle.

5.5.2 Physical drivers of seasonality in the 2nd harmonic

The observed amplitude of the 2nd harmonic is largest over equatorial regions of eastern South America and Africa (Figure 5.8), which is largely due to hydrologic changes linked to the semi-annual passage of the sun. However, the importance of the 2nd harmonic is not constrained to only the tropics. For example, the amplitude is high over much of Australia and above 0.5‰ over most of the middle to high-latitude regions of North America and Asia. The GCMs do remarkably well at capturing the correct regions

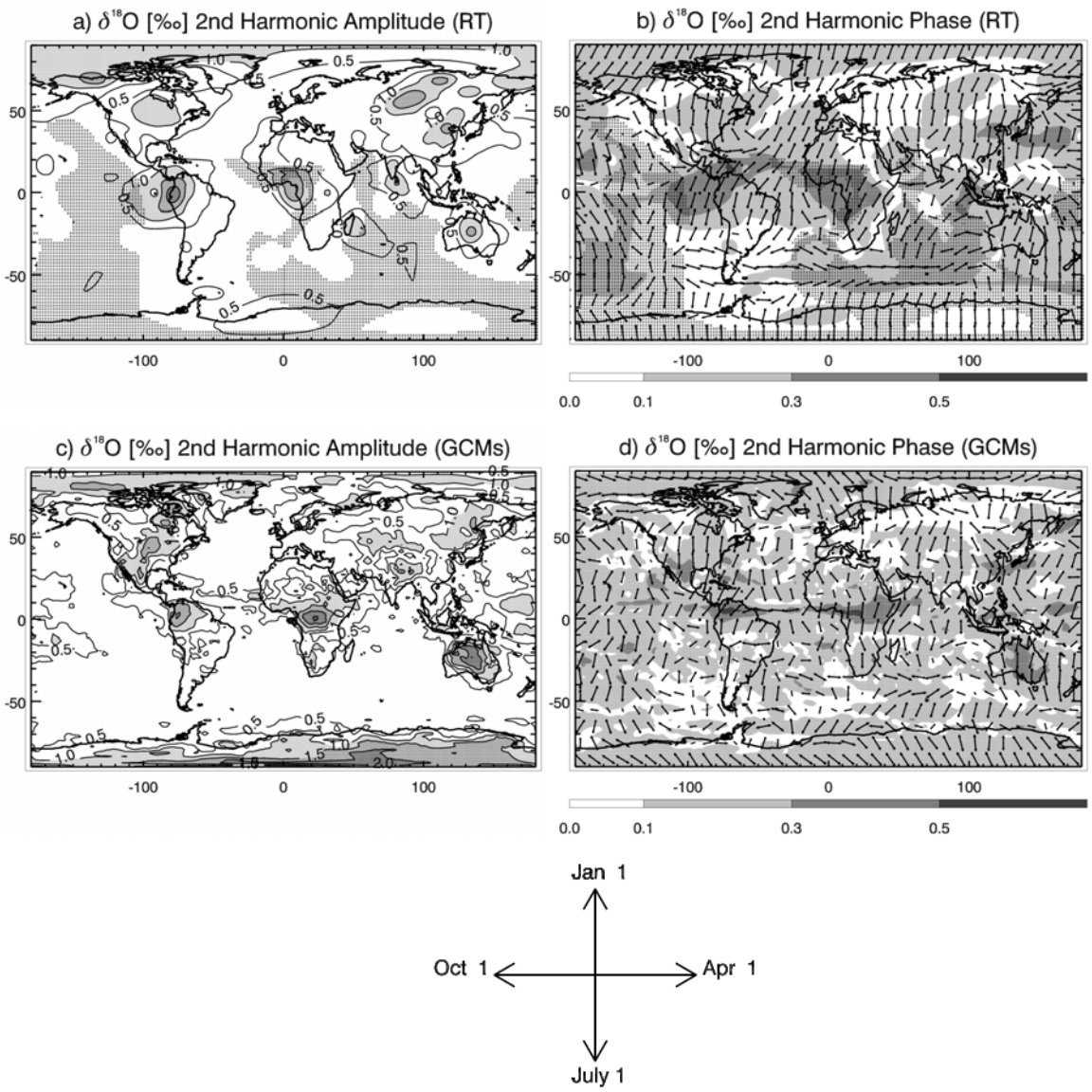

Figure 5.8. Spatial distribution of the amplitude (a, c) and phase (b, d) of the 2nd harmonic in the $\delta^{18}O$ seasonal cycle from the RT approach and GCM mean. Contours of the phase plots indicate the fraction of the total amplitude explained by the 2nd harmonic. Phases are represented by arrows that are oriented such that the angle relative to north indicates the phase of the harmonic. Bottom key is used to determine the phase in terms of the month of maximum value. The amplitude is half of the difference between maximum and minimum values. Stippling in a and b indicates regions where observational data are sparse (station probability is less than.0.1×10^{-6} km^{-2}).

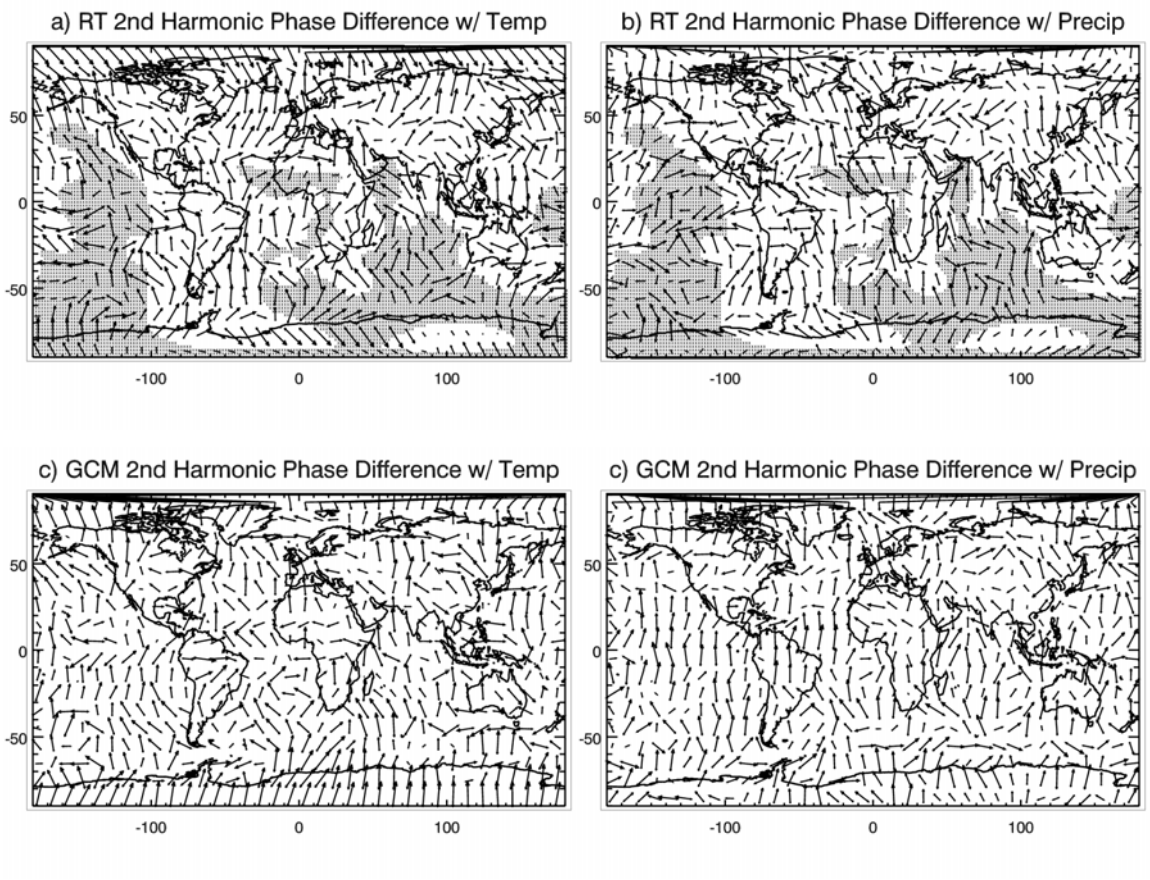

Figure 5.9. Spatial distribution of the phase differences of the 2nd harmonic between $\delta^{18}O$ values and temperature (a and c) and precipitation (b and d) seasonal cycles from the RT approach and GCM mean. Phase differences are represented by arrows that are oriented such that the angle relative to north indicates the extent to which the two variables are out of phase. Stippling in a and b indicates regions where observational data are sparse (station probability is less than.0.1×10^{-6} km^{-2}).

where the 2nd harmonic amplitude is high as well as the correct relative size of the amplitude. Furthermore, the simulated phase of the 2nd harmonic agrees well with the observations in these regions where the 2nd harmonic amplitude is large. This suggests that the models reasonably capture the physics that cause the semi-annual cycle in $\delta^{18}O$ values for certain regions across all latitudes.

To better understand what is driving both the observed and simulated semi-annual cycle in $\delta^{18}O$ values, phase differences between $\delta^{18}O$ values and both temperature and precipitation are shown in Figure 5.9. Over the two northern mid-latitude continental regions when a temperature effect may be expected, Figure 5.9a shows the phase of the 2nd harmonic in $\delta^{18}O$ values does not match-up with that of the 2nd harmonic in air temperature (arrows not vertical in Figures 5.9a). Similarly, simulated $\delta^{18}O$ values are not consistently in phase with temperature in the 2nd harmonic (Figure 5.9c). Thus, both observations and model simulations indicate that the phase of the 2nd harmonic outside of the tropics is unrelated to the temperature effect and likely due to other processes like variations in vapor transport and baroclinicity

In tropical regions where the observed 2nd harmonic amplitude is high, the maximum in $\delta^{18}O$ values is not completely in anti-phase with precipitation amount (arrows are not horizontal in Figures 5.9b). Table 5.1 shows the 2nd harmonic phase difference between $\delta^{18}O$ values and precipitation amount for certain regions within the tropics. The values in Table 5.1 reveal that the 2nd harmonic is closer to being in phase with precipitation than in anti-phase. The simulated 2nd harmonic in $\delta^{18}O$ values also does not appear to be in anti-phase with the precipitation as the 1st harmonic was. On average, the phase of the simulated 2nd harmonic in precipitation lags $\delta^{18}O$ values by only 23 days (far from 90 days, which would be anti-phase). Similar to the findings

for the mid and high-latitudes, these results suggest that the phase of the semi-annual cycle within the tropics is largely influenced by processes other than those which control precipitation amount, and as such a description of the variability as a simple amount effect is misleading. Instead, variations in moisture transport direction are more likely drivers. In addition, these results indicate that the GCMs not only simulate the correct amplitude and phase of the 2nd harmonic globally, but also correctly simulate non-local processes as a major driver of the seasonality of the 2nd harmonic.

5.5.3 Conclusion

An analysis was performed to establish to what degree GCMs are able to simulate the relationships between the isotopic composition of precipitation and temperature and precipitation amount and to illustrate that the model errors are largely results from an inability to correctly simulate the balance between the local controls on isotopic composition and the variable processes which set the isotopic composition at some upstream location. The use of a statistical model in the analysis confirms the work of *Bowen and Wilkinson* [2001] and *Farquhar et al.* [1993] in that simple regressions can predict the annual mean $\delta^{18}O$ values well, however, I note that the apparent great skill with which regression-based models reproduce isotopic distribution stems from the dominant role of the latitudinal variations poleward of the tropics. While about 84% of the total spatial variance is modeled, only 50% of the variance in zonal anomalies is captured by the empirically based RT approach.

By comparing the biases of the observation-based regression with that of the GCM-based regressions, it was found that the biases from GCM-based regressions are much larger and have greater spatial extent than those from observations. Because the isotopic composition is known in

GCMs, these results show that temperature and precipitation are not completely accurate predictors, and that a regression model based on these has clear quantitative limitations even though there are reasonable qualitative similarities in the spatial maps that result. These results also suggest that the GCMs overemphasize the role of non-local processes (e.g., large scale transport) in the simulation of the hydrological cycle, and, in so doing, downplay the role of local microphysical cloud processes and local surface exchange. Furthermore, the regions where the GCM mismatch is greatest (the mid and high-latitudes) are also large regions where the models simulate δ values that are not depleted enough. Thus, the overemphasis of large scale transport without temperature controlled condensation, or under emphasis of local cloud processes acting on the large-scale, is likely causing simulated δ values to be less negative in the mid and high-latitudes. Beyond transport the GCMs could also be simulating too much evaporation and boundary layer mixing that would tend to re-enrich a poleward moving air mass. In both cases the lack of agreement provides a clear indicator that the balance of different fluxes which contribute to the hydrolocial cycle is incorrectly simulated.

From both observations and GCM simulations, the phase of the 1st harmonic of the seasonal cycle is very uniform in the mid to high-latitudes, and corresponds to a maximum that is consistent with temperature maxima. Similarly, the phase of the 1st harmonic within the tropics and subtropics is consistent with precipitation minima where 1st harmonic amplitudes are high. However, my analysis of the leads and lags suggests that for some tropical regions (like over the Atlantic) the observed seasonal amount effect is likely caused by seasonal air mass changes, which would be consistent with the findings of *Feng et al.* [2009] of seasonal changes in subtropical vapor sources. On the other hand, for other regions (like over Africa and the Indian Ocean) the amount effect is expected to be due to cloud processes described by *Risi et al.* [2008].

Thus, the present study argues that the cause of the seasonal amount effect is not the same throughout the tropics, but is expected to be due to a combination of local and non-local controls depending on the region.

GCM simulations produce lags and leads associated with the amount effect, but which are inconsistent with the RT approach. Thus, the causality of the amount effect in the simulations is not in agreement with the causes reflected in the observed data. This would indicate that either the models are not correctly simulating the processes that are leading to the seasonal amount effect or that the RT approach needs to be better constrained by observations, which would indicate a need to measure δ values at more tropical locations.

Both the observed and simulated phase of the 2nd harmonic does not seem to be related to the amount effect within the tropics or the temperature effect in the mid and high-latitudes. Thus, the phase of the 2nd harmonic is likely to arise from variability in storm track activity or other non-local processes such as vapor transport and/or mixing, and is a feature which is not explained well with regression techniques. This result provides a cautionary example of the need to better understand the underlying physics to be confident in simple empirical relationships.

While local temperature and precipitation are used as predictors in the regressions, and deviations are viewed as the non-local component, local temperature and precipitation themselves are also influenced by non-local processes such as advection, which must be borne in mind for the definition of "non-local" used here. A limitation in the analysis here is that regression coefficients for the GNIP stations are unfairly biased to fit the large number of European stations, and not the more remote stations, whereas the GCM based regression coefficients do not favor a particular region. Consequently, the RT results from regions like Europe can be viewed with more confidence. Nonetheless, the challenge still remains for GCMs

to correctly simulate the impact of non-local processes on the water cycle, and specifically shift the balance more towards local processes like cloud physics and boundary layer exchange. This would likely reduce the large errors seen in simulated δ and d values over the mid and high-latitudes and also have beneficial implications for the simulated water and energy balance.

5.6 Appendix 5A: Detailed Model Description

The annual mean values at each (GNIP) location are estimated by establishing a regression model. The variables considered are the five used by *Farquhar et al.* [1993], T, T^2, P, P^2, and $Z^{1/2}$; the three used by *Bowen and Wilkinson* [2001], $|\phi|$, ϕ^2, and Z, and three others, $P^{1/2}$, potential temperature (θ), and θ^2. It is neither necessary nor statistically rigorous to include a large subset of these variables in the regression. As such, a stepwise approach is used to select a limited set of predictors. Table 5.2 shows the dependence of annual mean $\delta^{18}O$ values on these variables, as the correlation with each of the variables (left-hand column of Table 5.2). The T term had the highest correlation, which was then chosen for a single variable regression to estimate annual mean $\delta^{18}O$ values. The remaining predictor candidates were then correlated with the regression residual. As indicated in the table, the variable that had the highest correlation with the residual was the $P^{1/2}$ term, which was added to the regression. This method was repeated until the separate variables and the regression residual failed to produce a correlation coefficient of r = 0.0535 (significant at the 80% level). As such, a total of five variables were selected: T, $P^{1/2}$, P^2, Z, and $|\phi|$. However, when these five variables are used in the regression, they produce many large and positive values within the tropics and subtropics. Additional regressions were calculated using the five selected variables plus one of each of the non-selected variables. It was found that the addition of the T^2 term greatly reduced the number of high and

positive values, thus leading to the regression equation (2). Once the regression coefficients are found, they are applied to gridded *T*, *P*, and *Z* fields to obtain the gridded $\delta_a(\lambda,\phi)$ field.

A second step in evaluating (5.1) makes use of a Fourier transform to estimate the seasonal cycle at each GNIP station for each of the 12 months. The transform produces a set of six complex coefficients that capture the leading harmonics that make up the seasonal cycle without aliasing. The time series for each station can then be represented by the summation of these six harmonics:

$$\delta_m = \sum_{k=1}^{6} A_k \cos\left(\frac{2\pi mk}{12}\right) - B_k \sin\left(\frac{2\pi mk}{12}\right) \qquad (5.A1)$$

where k is the frequency, and A_k and B_k are the real and imaginary parts of the complex amplitudes, respectively. For many stations, only 3 to 4 years of data exist, which in turn can cause the long term mean of the seasonal cycle to be noisy, and unlikely to be statistically stationary. To avoid over fitting, particularly where there are only a few years of data, only the first four harmonics are used. Once A_k and B_k are obtained for each station, they are interpolated onto a grid as $A_k(\lambda,\phi)$ and $B_k(\lambda,\phi)$ (see Appendix B). At each gridcell the monthly mean anomaly is calculated by evaluating a summation similar to equation (A1), to produce fields for the 12 monthly values that characterize the mean seasonal anomalies $\delta_m(\lambda,\phi,t)$. The bias term is calculated by applying (3) and interpolated onto a grid using the method described in Appendix 5B.

Table 5.2. Correlation of variables with $\delta^{18}O$ and regression residuals.

	r	r_1	r_2	r_3	R_4	r_5
T	**0.902**	-	-	-	-	-
$\|\phi\|$	**-0.686**	**0.211**	-	-	-	-
Z	**-0.149**	**-0.115**	**0.152**	-	-	-
$P^{1/2}$	**0.529**	**-0.063**	0.034	**0.060**	-	-
P^2	**0.280**	**-0.201**	**-0.080**	-0.034	**-0.089**	-
T^2	**0.893**	-0.020	-0.012	-0.010	-0.010	-0.008
P	**0.425**	**-0.140**	-0.023	0.014	0.047	-0.013
$Z^{1/2}$	**-0.144**	**-0.103**	**0.119**	-0.034	-0.034	-0.031
ϕ^2	**-0.783**	**0.094**	-0.045	-0.024	-0.025	-0.015
Θ	**0.737**	**-0.056**	**0.086**	0.003	0.003	0.003
Θ^2	**0.718**	**-0.070**	**0.082**	-0.002	-0.001	0.001

5.7 Appendix 5B: Interpolation

A Cressman-like objective analysis [*Cressman*, 1959] is used for many of the components that make up (1). The procedure entails finding the weighted mean value of some quantity X on a grid, given a number of values X_j with irregularly distributed positions λ_j, ϕ_j. That is,

$$X(\lambda,\phi) = \frac{1}{A(\lambda,\phi)} \frac{\sum_j X_j W(d_j)\cos\phi_j}{\sum_j W(d_j)\cos\phi_j} \tag{5B.1}$$

where A is the area of each grid cell, and included for quantities needed in per unit area. An example is where a probability distribution of observational points is desired where X is set to

one for all points *j*, and the resulting field has units of probability per unit area. The weight *W* is a function of the great circle distance (d_j) between each grid cell center and each observation,

$$W(d_j) = \frac{R_c^2 - d_j^2}{R_c^2 + \left(\gamma^{-1} - 1\right) d_j^2} \qquad \text{(5B.2)}$$

R_c is a critical radius that ensures *W* is positive for all d_j larger than the critical radius, R_c. The shape of the weighting is modified by the "pinching" factor (γ), such that the mean radius of the weighting is reduced with smaller values. Here the weight is defined with R_c = 4100 km, and γ=0.008, and yields a mean effective radius of 312 km. The computational grid is chosen to be 2.0° longitude x 2.0°.

Chapter 6

Climatic controls on the deuterium isotopic composition of modeled leaf wax n-alkanes and implications for Eocene climate proxies

6.1 Introduction

Organic matter derived from plants has the potential to capture the deuterium/hydrogen ratio of precipitation, as meteoric water provides the hydrogen source for most plant organisms on Earth [*Epstein et al.*, 1976]. The hydrogen isotopic composition of a plant's leaf wax *n*-alkanes reflects the δD value (expressed as the deviation of the measured hydrogen isotope ratio from a standard) of a plant's source (i.e. soil) water [*Sessions et al.*, 1999]. In turn, the isotopic composition of source water is largely controlled by the δD value of local precipitation. Numerous studies have demonstrated spatial and temporal relationships between δD values of precipitation and temperature and precipitation amount [*Dansgaard*, 1964]. Provided that the δD values of water isotope proxies (e.g. through leaf wax derived *n*-alkanes) are preserved, past changes in local environmental conditions can be reconstructed.

Past temperature reconstructions using *n*-alkane δD values are based on a local δD-T conversion factor derived from modern observations, and are typically around 9‰/K [*Jouzel et al.*, 1993, 1996; *Petit et al.*, 1999]. An uncertainty in proxy-derived δD values due to variable leaf water enrichment, as a consequence of evapotranspiration (e.g. *Leaney et al.* [1985] found deuterium enrichment ranged from 20‰ to 80‰) on the order of 50‰ results in an error in estimates of local past temperature of about 5.6K.

In addition to the potential variations in the original δD value of source water, the final isotopic composition of n-alkanes found in leaf waxes is influenced by a sequence of fractionation processes prior to and during the biosynthesis of the hydrocarbons. Evaporation of soil and leaf water causes leaf water δD values to become enriched relative to precipitation [*Craig and Gordon*, 1965; *Flanagan et al.*, 1991; *Still et al.*, 2009], while fractionation during the biosynthesis of the *n*-alkanes causes depletion of δD values through preferential incorporation of the lighter isotopologue. Recent studies suggest that fractionation during biosynthesis is constant (amongst plant species and under varying environmental conditions) at a value of about -160‰ [*Sessions et al.*, 1999; *Sachse et al.*, 2004, 2006]. Evaporative enrichment from leaf and soil water is rarely large enough to outweigh the large -160‰ fractionation from biosynthesis [*Sachse et al.*, 2006]. Consequently, the overall offset between the isotopic composition of precipitation (δD_P) and that of the *n*-alkanes (δD_a) (hereafter $\varepsilon_{w/a} = \delta D_a - \delta D_P$) is almost always negative. Using an $\varepsilon_{w/a}$ value, measured δD_a values from ancient sediments are converted to δD_P values, which are used to estimate past temperatures and infer hydrological changes. However, *Sachse et al.* [2006] and *Liu et al.* [2006] have shown differing $\varepsilon_{w/a}$ values between different plant species due to variations in both plant anatomy and environmental conditions.

Craig and Gordon [1965] presented a steady-state theory for approximating the isotopic composition of surface water, which has been modified by *Flanagan et al.* [1991] to predict the isotopic composition of leaf water (δD_L) under steady state conditions such that:

$$\delta D_L = \varepsilon_{L-V}(T) + (1-h)(\delta D_{SW} - \varepsilon_k) + h\delta D_{CV} \qquad (6.1)$$

where $\varepsilon_{L\text{-}V}(T)$ is the temperature (T) dependent equilibrium fractionation of HDO during the liquid-vapor phase transition, ε_k is the kinetic fractionation of HDO during the diffusion of vapor across the stomata and leaf boundary layer, h is relative humidity at the surface of the leaf, δD_{SW} is the isotopic composition of the soil water taken up by roots, and δD_{CV} is the isotopic composition of the canopy vapor. *Still et al.* [2009] have shown that this steady state assumption is remarkably robust during the daytime when transpiration and photosynthetic production are high. Equation (6.1) shows that the isotopic composition of leaf water is largely controlled by the δD values of soil water and canopy vapor, which in turn are set by δD values of precipitation and atmospheric vapor. Equation (6.1) shows how relative humidity influences the balance between soil water and canopy vapor contributions to δD_L, as well as that it regulates the strength of the kinetic fractionation term. Indeed, equation (6.1) predicts that a relative humidity change of 10% units corresponds to a leaf water change of approximately 12‰. Also, the value of $\varepsilon_{L\text{-}V}(T)$ changes by -1.1 ‰/K at a temperature of about 300K, which is typically neglected for proxy-reconstructions.

It is likely that many of the parameters controlling δD_L were different during different periods of the past. For example, the Eocene (57.8–36.6 Ma) was characterized by high temperatures and an intensified hydrological cycle relative to today [*Jahren and Sternberg*, 2003], which likely modified $\varepsilon_{L\text{-}V}$, h, δD_{SW} and δD_{CV} values (Equation 6.1). Using a comprehensive isotopic fractionation model fitted to a detailed land surface model and atmospheric general circulation model, this study evaluates the degree to which Eocene environmental conditions cause changes to δD_L values and thus $\varepsilon_{w/a}$ as recorded in leaf wax *n*-alkanes.

6.2 Model Description and Experiment Configuration

The H_2O, HDO, and $H_2{}^{18}O$ content of precipitation and water vapor as well as meteorological conditions for both the Eocene and the present-day were simulated using ISOCAM. ISOCAM is a modified version of CAM3, the National Center for Atmospheric Research (NCAR) Community Atmosphere Model (CAM) [*Noone*, 2003, 2006; *Noone and Sturm*, 2010]. The fractionation scheme is based on that of *Noone and Simmonds* [2002] but includes a more detailed multiphase cloud microphysical model adapted from *Federer et al.* [1982] and a more detailed treatment of convective transport of moisture [*Noone and Sturm*, 2010]. Output from ISOCAM was used to force the isotopic version of the NCAR Land Surface Model (ISOLSM) [*Bonan*, 1996; *Riley et al.*, 2002; *Noone et al.*, 2002]. ISOLSM simulates the δD and $\delta^{18}O$ values in soil, xylem, and leaf waters based on modeled hydrologic and energy balance constraints. The leaf water model within ISOLSM employs a time-dependent mass balance that includes a transpiration dependent leaf turnover time-scale to calculate δD_L values [*Dongman*, 1974; *Still et al.*, 2009]. The deuterium content of leaf wax *n*-alkanes (δD_a) was then estimated by computing the photosynthesis-weighted δD value of leaf water and subtracting 160‰ to account for biosynthetic fractionation [*Sessions et al.*, 1999; *Sachse et al.*, 2004]. Finally, $\varepsilon_{w/a}$ values were calculated by subtracting the amount weighted δD of local precipitation from local δD_a values.

Table 6.1. Name and description of the three Eocene and three present-day simulations and the four sensitivity experiments.

Simulation	Description
PD-VAR	Forced with a present day ISOCAM simulation with varied best guess vegetation type
EOC-VAR	Forced with an Eocene-like ISOCAM simulation with varied best guess vegetation type
PD-BET	Forced with a present day ISOCAM simulation with broadleaf evergreen tress at each grid-cell
EOC-BET	Forced with an Eocene-like ISOCAM simulation with broadleaf evergreen trees at each
PD-BDT	Forced with a present day ISOCAM simulation with broadleaf deciduous trees at each grid-cell
EOC-BDT	Forced with an Eocene-like ISOCAM simulation with varied best guess vegetation type
EOC/PD-CO2	EOC-BDT with present day CO_2 levels
EOC/PD-TEMP	EOC-BDT with present day temperatures
EOC/PD-RAD	EOC-BDT with present day solar radiation
EOC/PD-RH	EOC-BDT with present day relative humidity

Both present-day and Eocene simulations were performed with ISOCAM and described in detail elsewhere [*Speelman et al.*, submitted]. For the Eocene simulations, I incorporated realistic, best guess, Eocene bathymetry, topography, land surface conditions, and vegetation as boundary conditions (described in *Sewall et al.* [2000]). The Eocene ISOCAM simulations were initialized using the atmospheric state from an equilibrium simulation of a fully coupled CSM1.4 Eocene run [*Huber and Nof*, 2006]. Eocene sea surface temperatures (SST) were adapted using a fixed, zonally constant, offset based on TEX_{86} SST estimates from the Early/Middle Eocene

[*Brinkhuis et al.*, 2006; *Pearson et al.*, 2007]. To evaluate the influence of vegetation type on $\varepsilon_{w/a}$ values, three separate sets of ISOLSM simulations were conducted for each time period (Table 6.1). The first of these simulations sets the vegetation at each grid cell to be the type closest to the plant function type used in ISOCAM. The two other sets of simulations were configured to have only 1) broadleaf evergreen trees and 2) broadleaf deciduous trees at every land grid-cell that contains vegetation. Thus, these last two sets of simulations can be used to evaluate differences irrespective of vegetation type. For similar reasons, the soil type is prescribed to be the same for all simulations and for all grid-cells (43% sand, 41% silt, and 16% clay, with 5% of the land fraction lakes and 5% wetlands). The horizontal resolution of the model is given by triangular truncation of the spherical harmonic spectrum at wave number 31, which corresponds to a Gaussian grid of about 3.75 degree longitude x 3.75 degree latitude. The ISOCAM simulations ran for 30 years, with the last 10 individual years used cyclically to force ISOLSM. ISOLSM simulations ran for 40 years with the last 20 years averaged and used for the analysis.

This off-line model configuration did not allow feedbacks to local canopy level relative humidity and the δD values of precipitation and vapor, and there were no diurnal cycles within the CAM forcing data. These limitations should be kept in mind while considering the analysis below.

6.3 Model Results

6.3.1 Present-day Eocene comparison

Many studies that measure δD_a values also calculate the apparent fractionation (ε'), which is slightly different than my definition of the δD_a-δD_p offset ($\varepsilon_{w/a}$). Apparent fractionation is on average 7‰ lower than $\varepsilon_{w/a}$ values and is defined as:

$$\varepsilon' = 1000\left[\frac{\delta D_a + 1000}{\delta D_P + 1000} - 1\right] \qquad (6.2).$$

Table 6.2. Present-day model results and comparison with other studies.

Plant	Reference	[a]Reference ε'	[a]Model ε'
Quercus	*Yang and Huang* [2003]	-117	-110
Platanus	*Yang and Huang* [2003]	-93	-110
Salix	*Yang and Huang* [2003]	-144	-110
C_3 plants	*Chikaraishi and Naraoka* [2003]	-117 ± 27	-130
C_4 plants	*Chikaraishi and Naraoka* [2003]	-132 ± 12	-131
CAM plants	Chikaraishi and Naraoka [2003]	-147 ± 10	-131
Fern	*Chikaraishi and Naraoka* [2003]	-131 ± 6	-136
Lake sediments	*Sachse et al.* [2004]	-128 ± 12	-119
C_3-gymnosperm	*Chikaraishi et al.* [2004]	-91 to -152	-128
C_3 grasses	*Smith and Freeman* [2006]	-165 ± 12	-137
C_4 grasses	*Smith and Freeman* [2006]	-140 ± 15	-139
Deciduous trees	*Sachse et al.* [2006]	-122	-121
Sphagnum	*Sachse et al.* [2006]	-131	-119
Plant biomass	*Sachse et al.* [2006]	-118	-119

[a]Units of ‰

For validation, I compared measured ε' values with modeled values. For modeled values, single grid-cell simulations are conducted for the region where the measured values were taken from. Vegetation type was adjusted for each simulation to best reflect the plant species from which the *n*-alkanes were derived. Table 6.2 shows estimated ε' values from these simulations, and compares them with measured present-day values. The modeled values were within the measured range for deciduous trees in Idaho [*Yang and Huang*, 2003], C_4 grass in South Dakota [*Smith and Freeman*, 2006], and ferns, C_3 and C_4 plants in Japan [*Chikaraishi and Naraoka*, 2003; *Chikaraishi et al.*, 2004]. Modeled values also fell within the observed range for European deciduous trees and terrestrial lake sediments [*Sachse et al.*, 2004, 2006]. The model failed to predict ε' values for Japanese CAM plants and European Sphagnum, though this might have been due to inadequate (or complete lack of) representation of these particular plant species in the model. Simulated values also did not agree with C_3 grasses measured by *Smith and Freeman* [2006], which could have been a consequence of mismatch between model conditions and their greenhouse growing conditions. Nonetheless, results in Table 6.2 demonstrate that the model does an adequate job in predicting fractionation processes that controlled δD_a values.

Figure 6.1a and 6.1b show simulated $\varepsilon_{w/a}$ values for present-day and Eocene conditions using the most realistic, "best guess", vegetation type, while Figures 6.1c-6.1e shows how $\varepsilon_{w/a}$ values spatially vary when the vegetation type is constant. For present-day, simulated $\varepsilon_{w/a}$ values were noticeably high (less negative) in regions of Asia and North America. However, $\varepsilon_{w/a}$ values were remarkably lower in northwest North America when the grid-cells contained broadleaf evergreen trees. Importantly, the model results demonstrate strong spatial variations in present-day $\varepsilon_{w/a}$ values, a result of variations in local meteorological and environmental conditions. For the present-day simulations, the choice of vegetation type partially affected the spatial variations

in $\varepsilon_{w/a}$ values, though many features in panels 6.1a, 6.1c, and 6.1e are consistent across all three present-day simulations (e.g. high $\varepsilon_{w/a}$ values over most of Asia).

Table 6.3. Simulated mean $\varepsilon_{w/a}$ values and the spatial standard deviation of $\varepsilon_{w/a}$ values.

Simulation	Standard Deviation $\varepsilon_{w/a}$ (‰)	Global Mean $\varepsilon_{w/a}$ (‰)	NH mid and high-lat Mean $\varepsilon_{w/a}$ (‰)[a]
PD-VAR	19.2	-102	-90.5
EOC-VAR	9.6	-103	-97.2
PD-BET	13.2	-105	-96.4
EOC-BET	10.4	-105	-98.0
PD-BDT	16.7	-109	-96.2
EOC-BDT	10.9	-110	-102.8

[a]poleward of 35°N

Compared to the present-day simulations, the Eocene spatial variations in $\varepsilon_{w/a}$ values were less dependent on vegetation type. Table 6.3 displays the global mean, the northern mid- and high-latitude mean, and the global standard deviation in $\varepsilon_{w/a}$ values for the three present-day and three Eocene simulations. The predicted global mean Eocene $\varepsilon_{w/a}$ values tend to be just slightly more negative than present day (Table 6.3). When comparing the mean for the northern mid- and high-latitude (where most of the world's deciduous trees are found), the difference between Eocene and present-day $\varepsilon_{w/a}$ values was much greater, however, the difference was not spatially uniform. For example, for the broadleaf deciduous tree simulations $\varepsilon_{w/a}$ values were almost the same during the Eocene compared to the present-day simulation over much of Europe (~1‰ difference) and eastern North America (~2‰ difference), whereas differences were large over Siberia (~18‰ difference), central Asia (~20‰ difference), and western North America (a 22‰ difference in the Yukon and a -18‰ difference in the western U.S.). In the Eocene southwestern region of North America, $\varepsilon_{w/a}$ values were remarkably higher (less negative with a maximum value of -67‰), while values were lower to the north. Figure 6.1 clearly shows that

Eocene $\varepsilon_{w/a}$ values differ from present-day values depending on location, and these discrepancies have potential to bias estimates of past δD_P values and past temperature.

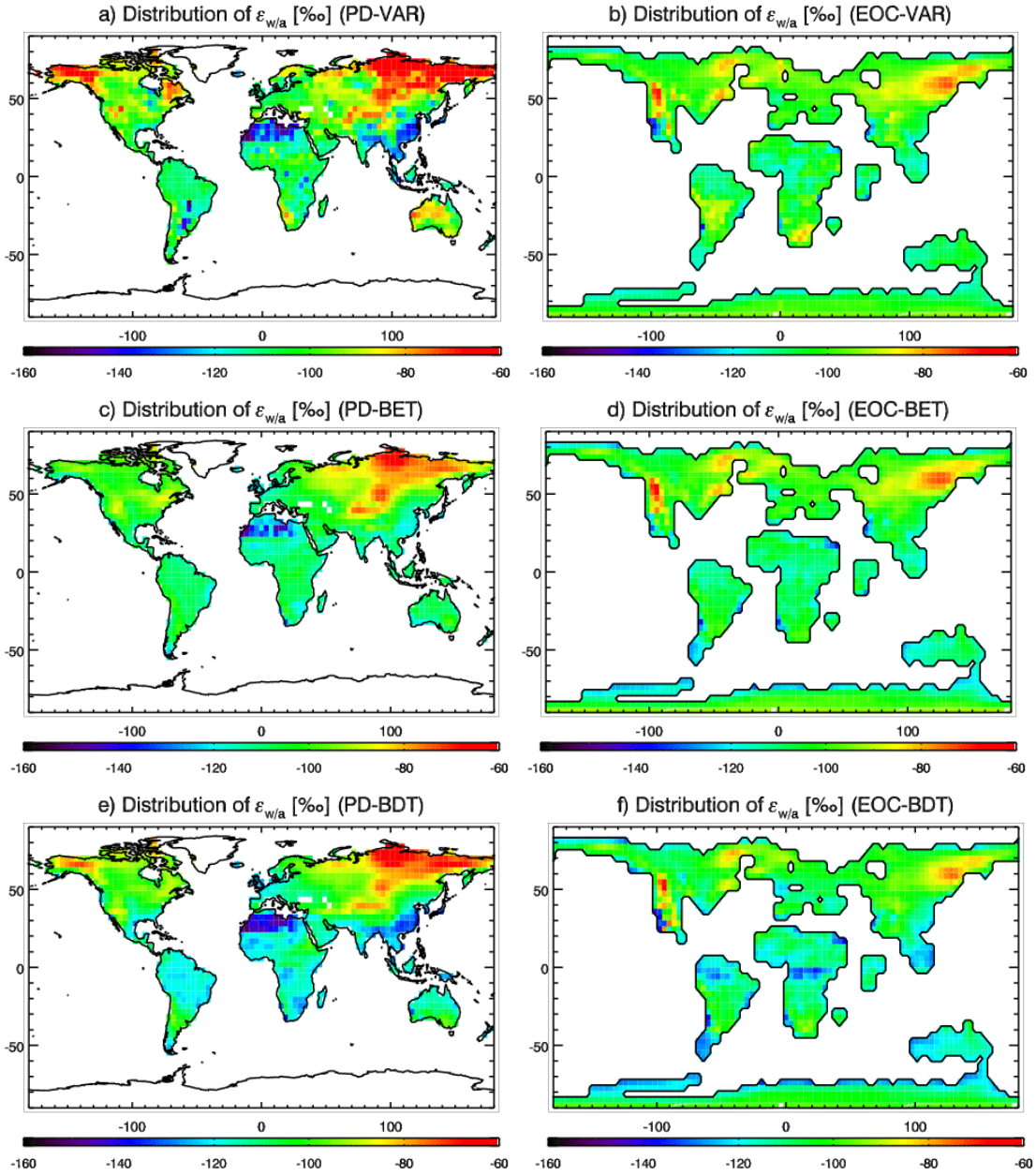

Figure 6.1. Global distribution of the offset value, $\varepsilon_{w/a}$ (‰), for the Present simulations and Eocene simulations using best guess vegetation type (a and b) broadleaf evergreen trees (c and d), and broadleaf deciduous trees (e and f).

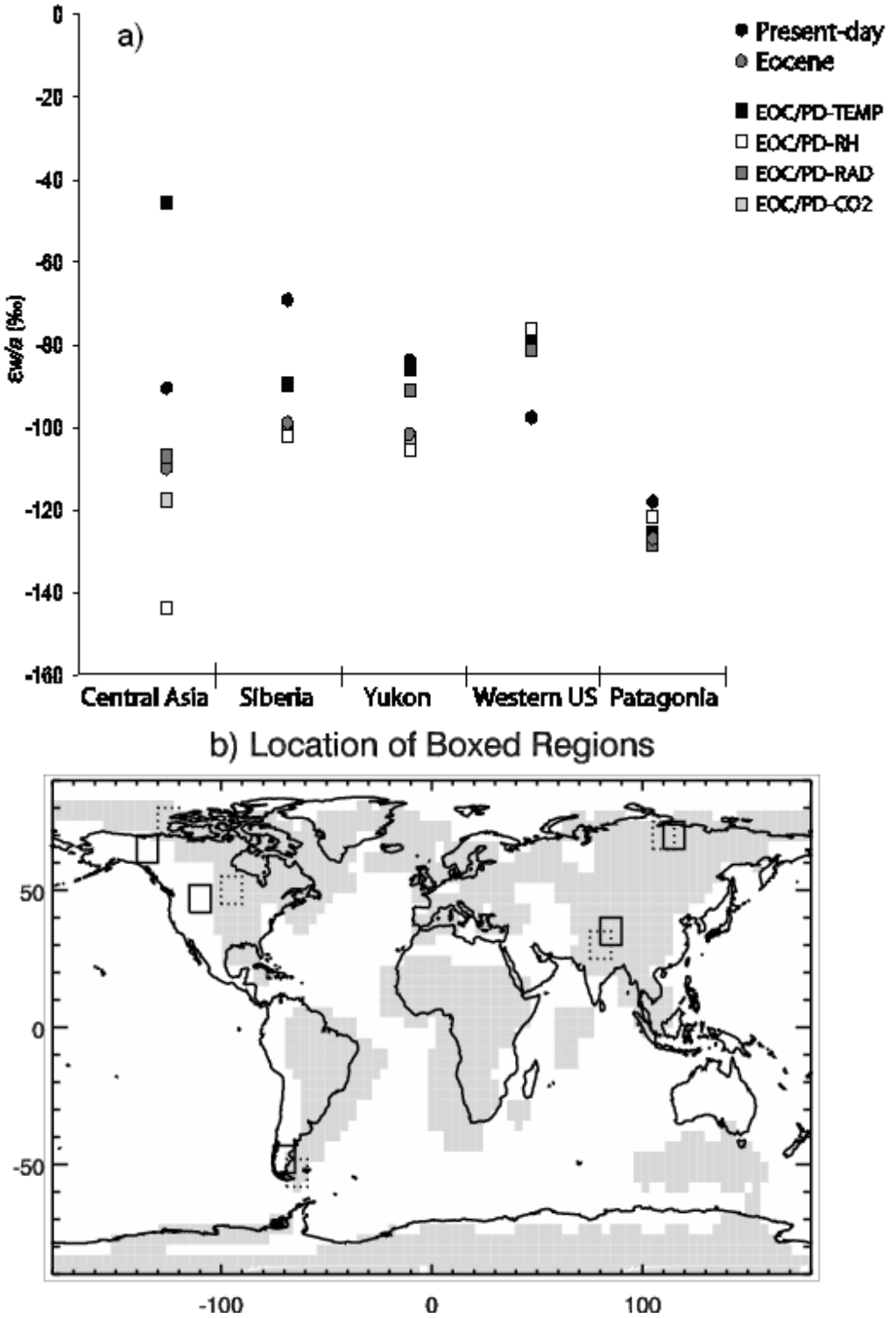

Figure 6.2. Mean $\varepsilon_{w/a}$ values (‰) for five regions for the six separate simulations listed in Table 6.1 (a). The locations of the five regions are shown in (b) as solid-line boxes for Present and dashed line boxes for Eocene. Continental locations during the Eocene are shown with light gray shading in panel b.

Assuming δD_P changes by 9‰/K [*Jouzel et al.*, 1993; 1996; *Petit et al.*, 1999; *Noone*, 2009] outside of the tropics, an average Eocene/present-day difference in $\varepsilon_{w/a}$ values of 7‰ at the northern mid- to high-latitudes would introduce a temperature estimate error of about 0.9K. However in specific regions where the difference between Eocene and present-day $\varepsilon_{w/a}$ values was relatively large reconstructed temperature errors will also be large. In Siberia, for instance, the modeled 18‰ difference results in an error of about 2K.

6.3.2 Results from sensitivity experiments

Relative humidity and air temperature directly influence equation (6.1) and therefore $\varepsilon_{w/a}$. Furthermore, atmospheric CO_2 concentration and solar fluxes influence stomatal resistance indirectly and can thus change h in equation (6.1). All of these variables were probably different during the Eocene. Four sensitivity experiments were performed in which each one of these four variables (temperature, relative humidity, solar radiation, or atmospheric CO_2 concentration) were set to present-day values, while maintaining Eocene-based values for all other variables. These sensitivity experiments were performed using only broadleaf deciduous trees to control physiologically induced differences. A list and description of each sensitivity experiment is given in Table 6.1. The influence of variables set to present-day values on Eocene model results is compared in five selected regions. The size of these regions is set to 10º of longitude by 10º of latitude, positioned at present day Central Asia, Siberia, the Yukon Territory, Western U.S., and Patagonia (shown as solid-line boxes in Figure 6.2b). To account for continental drift, Eocene results examined here are taken from regions that have been subjectively positioned at the approximate former location of these 5 areas (shown as dashed–line boxes in Figure 6.2b).

Figure 6.2a compares model results for these regions that showed a clear discrepancy between the present-day and Eocene modeled $\varepsilon_{w/a}$ values.

The EOC/PD-TEMP sensitivity simulation used modern-day surface air temperatures to reveal the impact of high temperatures on latent heat fluxes, stomatal conductance, fractionation, and ultimately the value of $\varepsilon_{w/a}$. For this simulation, specific humidity was adjusted to match Eocene relative humidity, ensuring that the model's response was not associated with a vapor pressure response. The lower present-day temperatures caused $\varepsilon_{w/a}$ values to increase (less negative), which can be seen in Central Asia, Siberia, and in the Yukon regions. This temperature response was partially due to changes in the equilibrium vapor pressure offset above a liquid surface ($\varepsilon_{L\text{-}V}$). At temperatures around 300K, the fractionation factor changes by -1.1 ‰/K. For the Central Asia region (where the modeled response was largest) the ISOCAM results suggest that the growing season temperatures were about 21K warmer during the Eocene, which decreased the fractionation factor by 23‰. The modeled difference in $\varepsilon_{w/a}$ values between the Eocene and EOC/PD-TEMP simulations were about 64‰ for this region, so changes in the fractionation factor alone can potentially account for about one-third of the total $\varepsilon_{w/a}$ response to temperature changes.

Comparing the Eocene simulation with a simulation in which relative humidity is set to present-day values (EOC/PD-RH experiment) shows drastic changes in δD of leaf water and $\varepsilon_{w/a}$ for some regions. In general, the use of present-day relative humidity caused $\varepsilon_{w/a}$ values to be more negative (with the exception of Patagonia). For these regions, the higher present-day relative humidity decreased leaf water isotope fractionation, due to decreased transpiration, causing δD of leaf water (and subsequently δD of *n*-alkanes) to be less enriched. The strongest isotopic response to relative humidity was found in Central Asia, where flux-weighted relative

humidity was 24% lower during the Eocene. Taking the derivative of equation (6.1) and assuming a kinetic fractionation factor of 42‰ and an 80‰ difference between δD_{SW} and δD_{CV} values gives sensitivity: $\partial \delta D_L / \partial h_a$ = -1.22‰/%. The modeled decrease in relative humidity would, therefore, cause δD_L values (and $\varepsilon_{w/a}$ values) to decrease by about 29‰ using the Craig-Gordon derived sensitivity, which is close to the modeled change of 33‰. A similar sensitivity was found in Chapter 3 in a set of experiments that simulated the ^{18}O content of leaf water, which was supported by observations of atmospheric $CO^{18}O$ in Chapter 2. For Patagonia, the lower present-day relative humidity does bring $\varepsilon_{w/a}$ values closer to present day simulated values, which indicates relative humidity is one of the variables that contributed to higher $\varepsilon_{w/a}$ values during the Eocene. For the other four regions, however, the model results suggest that relative humidity was not the main driver for the difference in $\varepsilon_{w/a}$ values between the two climatic states. In fact, in most regions humidity kept present day and Eocene $\varepsilon_{w/a}$ values from becoming too dissimilar by opposing changes associated with temperature and other factors (Figure 6.2a).

The Eocene simulations using modern-day radiation and modern-day CO_2 concentration only slightly altered δD and $\varepsilon_{w/a}$ values relative to the Eocene base simulation. In the Yukon region, however, radiation did appear to play a role as the region was at higher latitudes during the Eocene. The drastically lower solar energy input would have limited photosynthesis (Figure 1a in *Nemani et al.* [2003]), and caused both stomatal conductance and isotope fractionation to decrease.

To quantify the sensitivity of $\varepsilon_{w/a}$ to the parameters that showed the strongest impact, small perturbations were applied to both atmospheric temperature (T in units of K) and atmospheric relative humidity (h_a in units of %). Additional simulations were performed to test the sensitivity of the global mean $\varepsilon_{w/a}$ value to small global perturbations in temperature and

relative humidity. Sensitivities are thus approximated in terms of partial derivatives ($\partial\varepsilon_{w/a}/\partial T$ and $\partial\varepsilon_{w/a}/\partial h_a$). These sensitivities can be written as partial derivatives (rather than total derivatives) since the change in the forcing is on that of the parameter of interest (i.e., all other forcing terms held fixed). The sensitivities can be used to construct a prediction model where deviations from the global mean value can be estimated as:

$$\Delta\varepsilon_{w/a} = \Delta T \frac{\partial \varepsilon_{w/a}}{\partial T} + \Delta h_a \frac{\partial \varepsilon_{w/a}}{\partial h_a} \qquad (6.3).$$

The resulting modeled sensitivities were approximately: $\partial\varepsilon_{w/a}/\partial T$ = -1.4‰/K and $\partial\varepsilon_{w/a}/\partial h_a$ = -0.43‰/%. Consequently, these values can be used together with equation (6.3) to better estimate the $\varepsilon_{w/a}$ value to apply for any δD_a given known temperature and relative humidity anomalies. Because ΔT appears on the right, (6.3) must be modified to be useful for paleo-temperature reconstructions. Specifically, the reconstruction problem is posed as $T_{Eocene} = T_{Present} + \Delta T$. Noting that one can write:

$$\Delta(\delta D_P) = \Delta(\delta D_a) - \Delta\varepsilon_{w.a} \qquad (6.4)$$

$$\Delta T = \Delta(\delta D_P)\frac{\partial T}{\partial(\delta D_P)} \qquad (6.5).$$

Substituting equation (6.3) into (6.4) gives

$$\Delta(\delta D_P) = \Delta D_a - \Delta T \frac{\partial \varepsilon_{w/a}}{\partial T} + \Delta h_a \frac{\partial \varepsilon_{w/a}}{\partial h_a} \qquad (6.6)$$

which can be combined with equation (6.5) and rearranged to find an expression for the change in temperature:

$$\Delta T = \frac{\partial T}{\partial(\delta D_P)}\left(\Delta\delta D_a - \Delta h_a \frac{\partial \varepsilon_{w/a}}{\partial h_a}\right)\left[1 + \frac{\partial T}{\partial(\delta D_P)}\left(\frac{\partial \varepsilon_{w/a}}{\partial T}\right)\right]^{-1} \qquad (6.7).$$

The value of $\Delta\delta D_a$ is derived from analysis of deuterium in leaf wax *n*-alkanes from present-day and from those found within Eocene sediments. With the temperature isotope relationship specified by others (e.g. $\partial T/\partial(\delta D_P)$ [*Jouzel et al.*, 1993, 1996; *Petit et al.*, 1999]) and $\partial\varepsilon_{w/a}/\partial T$ and $\partial\varepsilon_{w/a}/\partial h_a$ derived here, equation 6.7 provides a more accurate estimate of past temperatures given a known difference in δD_a values and an assumed change in h_a, which could be difficult to estimate.

Table 6.4. Values used in equation (6.7) for the three simulated cases.

	Case 1	Case 2	Case 3
[a] $\partial T/\partial(\delta D_P)$	0.11 K‰$^{-1}$	0.11	0.11
[b] $\Delta\delta D_a$	-0.43‰	7.6	7.2
[c] Δh_a	1%	0	1%
[d] $\partial\varepsilon_{w/a}/\partial h_a$	-0.43‰%$^{-1}$	-0.43	-0.43
[e] $\partial\varepsilon_{w/a}/\partial T$	-1.4‰K^{-1}	-1.4	-1.4
[f] ΔT	0K	1	1

To demonstrate the usefulness of equation (6.7), three additional ISOLSM simulations were conducted to validate the reconstruction. The three scenarios considered here were 1) a 1% increase in relative humidity; 2) a 1K increase in global temperatures; and 3) both a 1K increase in temperature and a 1% increase in relative humidity. For the last two additional simulations, the δD values of precipitation and atmospheric vapor were also increased by 9‰. The values used in equation 6.7 and the simulated change in global mean δD_a values are shown in Table 6.4. There was no temperature change in case 1, only a 1% increase in relative humidity, which caused the simulated global δD_a value to decrease by 0.43‰. Evaluating equation (6.7) with this

change in δD_a values and the other values listed in Table 6.4 results in an estimated temperature change of 0K, which was the expected result. For the 2nd case, the 1K increase in temperature and the 9‰ increase in the δD values of precipitation and vapor caused global δD_a values to increase by 7.6‰, yielding a predicted temperature change of 1.0K (Table 6.4). When both changes are applied (case 3) ISOLSM simulates a 7.2‰ increase to global δD_a values, which also predicts a 1K increase in global temperatures. Thus, all 3 simulations demonstrate the ability of equation 6.7 to estimate temperature changes given differences in δD_a values and relative humidity.

Comparing Eocene and present-day simulations, equation (6.7) works remarkably well for some locations but poorly for others. For example, in Siberia, relative humidity and δD_a values were simulated to be about 10% and 25‰ higher during the Eocene, respectively, and equation (6.7) accurately backs out the 4K temperature difference. On the other hand, in the western U.S., equation (6.7) only predicts temperatures to be 1K higher during the Eocene, whereas the set temperature difference was 9K. The reason why equation (6.7) did not work for certain locations is that it relies on the seasonality of the growing season, precipitation amount, and the δD value of precipitation to be constant in time.

6.3.3 Validity of annual mean proxy

In addition to environmental controls on the biophysics, the premise that the *n*-alkane δD values can be used as a proxy for annual mean δD of precipitation (δD_P) rests on the stability in the seasonality of δD of precipitation relative to the growing season in which the leaf wax *n*-alkanes are produced. To evaluate these influences, the processes resulting in the final $\varepsilon_{w/a}$ value were broken down into three separate fractionation steps, including (1) precipitation to plant

xylem water, (2) xylem water to leaf water, and (3) leaf water to leaf wax *n*-alkanes. The focus here is on the isotopic fractionation within the first two processes, assuming as before, the fractionation in the final step is approximately constant at –160‰.

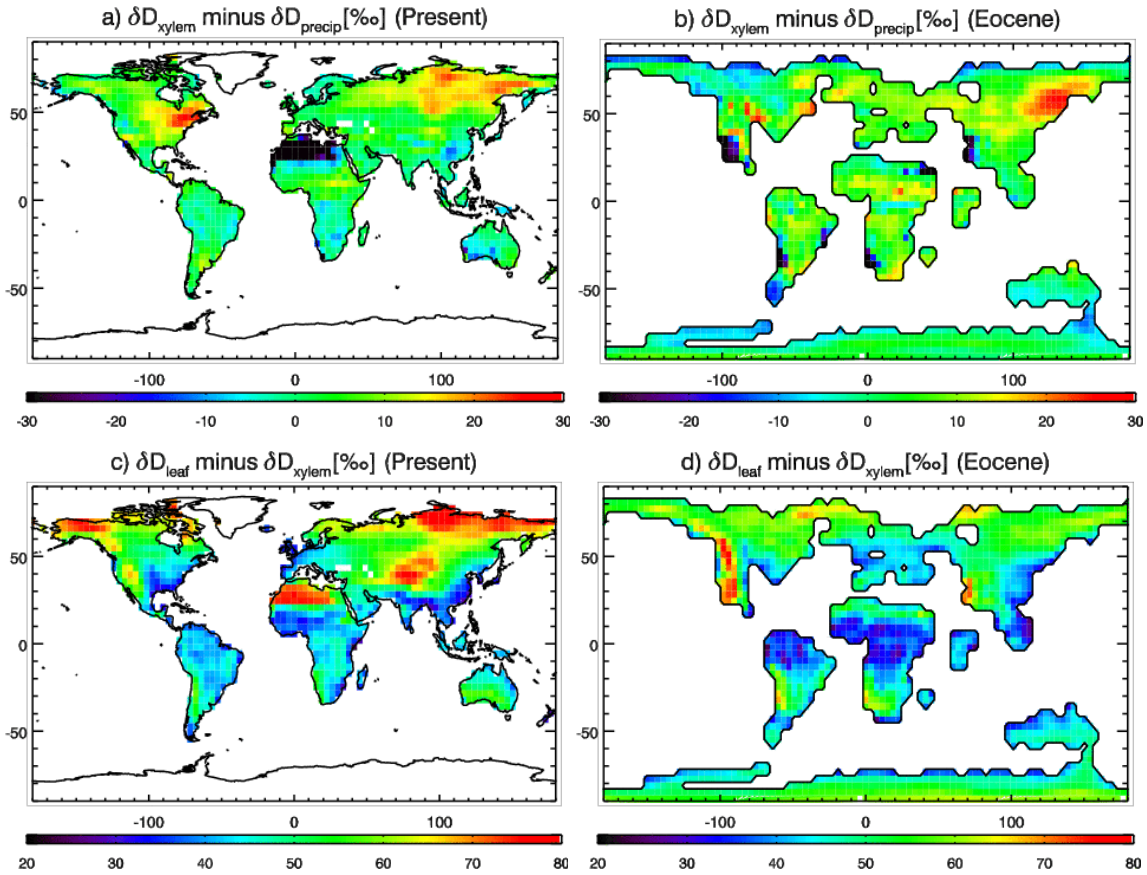

Figure 6.3. Photosynthesis weighted δD of xylem water minus amount weighted annual mean δD of precipitation (‰) for both Present and Eocene simulations (a and b). Also plotted are photosynthesis weighted mean δD of leaf water minus photosynthesis weighted mean δD of xylem (‰) (c and d).

Simulated amount-weighted δD_P values were subtracted from the photosynthesis weighted xylem δD_X values (1st component), and the same δD_X values were subtracted from photosynthesis weighted δD_L values (2nd component). Results are shown in Figure 6.3 for both present-day and Eocene broadleaf deciduous tree simulations. For the present-day simulation,

the δD_P and δD_X difference exerted a minor influence on $\varepsilon_{w/a}$ values, with an exception for Patagonia and parts of Asia where it acts to keep $\varepsilon_{w/a}$ values relatively high. On the other hand, much of the spatial variation in $\varepsilon_{w/a}$ values was a consequence of the differences between δD_X and δD_L values. For instance, in the Siberian and Yukon regions the high simulated $\varepsilon_{w/a}$ values (Figure 6.1e) largely reflect the δD_L-δD_X difference (Figure 6.3c). These findings suggest that present-day $\varepsilon_{w/a}$ values are largely influenced by the δD_L-δD_X difference (as modeled by equation 6.1), with the exception of some locations (Patagonia and Central Asia) where water isotope seasonality appears to play some role.

Compared to the present-day simulation (Figures 6.3c and 6.3d), the Eocene simulation predicted less enrichment from xylem to leaf water (with an exception to a broad region in western North America). As shown through the sensitivity experiments, this was largely a result of higher temperatures during the Eocene growing season, causing $\varepsilon_{w/a}$ values to become relatively low. Additionally, the influence of the δD_X-δD_P difference was not the same during the Eocene. Particularly, in Patagonia the δD_X-δD_P difference (Figure 6.3b) decreased $\varepsilon_{w/a}$ values on average by 14‰, in contrast to the present-day simulation, which increased $\varepsilon_{w/a}$ values by about 2‰. This decrease in δ values seems to primarily reflect seasonality in the isotopic composition of precipitation relative to the growing season and is partially responsible for the lower $\varepsilon_{w/a}$ values during the Eocene in this region. These results suggest that differences or changes in the seasonality of precipitation and/or the isotopic composition of precipitation can potentially change the values of $\varepsilon_{w/a}$, which is a factor that has not previously been accounted for in *n*-alkane proxy reconstructions.

6.4 Conclusion

This study showed that the offset between δD values of precipitation and δD values of leaf wax *n*-alkanes ($\varepsilon_{w/a}$) varies in space and that the relationship was different under Eocene environmental conditions. Results from model simulations suggest that in the northern mid- to high-latitudes $\varepsilon_{w/a}$ values were on average 6‰ lower during the Eocene. Sensitivity experiments showed temperature and relative humidity exert a large influence on $\varepsilon_{w/a}$ values, where the influence of temperature is partially associated with the temperature dependence of equilibrium fractionation. Over Siberia and Central Asia the lower $\varepsilon_{w/a}$ values found for the Eocene simulation were largely a result of the higher growing season temperatures, which reduced the efficiency of fractionation during evaporation from leaves. Over the Yukon differences in $\varepsilon_{w/a}$ values resulted from changes in solar radiation and temperature, while the differences in Patagonia were driven by a combination of relative humidity and the seasonal timing of the isotopic composition of precipitation.

Model results suggest that using a constant $\varepsilon_{w/a}$ value for reconstructing δD of paleo-precipitation from measured δD of *n*-alkanes is inaccurate. For the Eocene, the offset should be more negative than $\varepsilon_{w/a}$ values typically found today. This holds for many regions outside of the tropics (with the large exception in the western U.S.). Hence, when modern-day $\varepsilon_{w/a}$ values are used to reconstruct δD of paleo-precipitation, the reconstructed values will be skewed towards lower values, which in turn will lead to inaccurate interpretations of the paleo-hydrological cycle. Similarly, when using modern-day $\varepsilon_{w/a}$ values to estimate Eocene temperatures based on the δD of *n*-alkanes, the reconstructed values will be biased towards lower temperatures. This

would suggest that the Eocene epoch might have been warmer than suggested by temperatures previously derived from *n*-alkane proxies. Differences in leaf water enrichment introduce an uncertainty in temperature reconstruction from δD values of leaf wax *n*-alkanes and should be taken into account when using δD_a values as a temperature proxy.

Chapter 7

Conclusions

The first portion of the work presented here (Chapters 2-4) aims to better understand δC_a and specifically to understand the mechanisms that drive the interannual δC_a variations. I first examined the δC_a budget equation and identified meteorological variables that would potentially influence the δC_a year-to-year changes. To this end, I looked for empirical evidence of potential driving mechanisms by correlating interannual δC_a variations with various meteorological variables. Negative correlations were found between δC_a observations and relative humidity observations in both the Asia-Pacific and the Tropical Americas. I also found evidence for positive correlations between δW_P (the isotopic composition of precipitation) and δC_a variations. Examining the variations, I calculated rough estimates of changes to δC_a due to relative humidity and the isotopic composition of precipitation. These results indicated that interannual changes in δC_a were potentially driven by changes to isotope hydrology (i.e. δW_P) with a smaller and non-trivial contribution from relative humidity.

A model was constructed to simulate atmospheric CO_2 and $CO^{18}O$, and thus predict values of δC_a. Motivated by the correlations and estimations from the correlations analysis, sensitivity experiments were conducted (after demonstrating excellent model performance). The experiments revealed that δC_a was sensitive to relative humidity and temperature, but especially to the isotopic composition of precipitation and water vapor. The model was then reconfigured to simulate the interannual δC_a variations, and experiments were performed to quantify the contribution of a certain variable to the overall interannual δC_a variations. The simulated δC_a variations were greatly dependent on the δW_P variations, with some contribution from other

variables such as relative humidity and temperature. I suggest here that interannual δC_a variations are mostly caused by interannual δW_P and/or δW_{AV} variations. This does not agree with other studies [*Gillon and Yakir*, 2001; *Stern et al.*, 2001; *Ishizawa et al.* 2002; *Flanagan* 2005] that have suggested (with little or no empirical evidence) that interannual δC_a variations were caused by changes to ecosystem CO_2 fluxes. My results suggest that δC_a is (and can be used as) an indicator of hydrological cycle within high flux regions.

Motivated by these results, the second portion of this work (Chapter 5) focused on the observed and simulated $\delta^{18}O$ values of precipitation. In particular this work focused on understanding the controls of local and non-local processes on the observed annual means of δW_P. This was done through regression analysis, with regressions applied to both isotope equipped General Circulation Models (GCMs) and observations. I found that the GCM inability to simulate the relative importance of local and non-local processes may explain why the models inadequately simulate δW_P at mid and high latitudes. When examining leads and lags between the phase of the 1st and 2nd harmonic in δW_P and that of temperature and precipitation amount, I found that the phase of the 1st harmonic in the mid and high latitudes is consistent with what would be expected from a temperature effect. However, the 2nd harmonic was likely due to non-local processes such as advection changes and shifts in the storm track. A similar analysis was performed on GCM results and it was found that the models accurately simulate these phase dependencies. In general, it was found that the models do reasonably well at simulating the influences of local and non-local processes on the seasonality of δW_P though when analyzing the annual mean, the models overestimate the role of non-local (dynamical) processes in determining the annual mean δW_P at mid- and high-latitudes.

Finally, the third portion of this work (Chapter 6) focuses on differences between the offset of the δD value of precipitation and the δD value of leaf wax *n*-alkanes during two different periods of geological time. In particular, this work examined how the offset between the two δD values ($\varepsilon_{w/a}$) may have been different during the Eocene. To solve this problem, I employed the same isotope equipped land model (ISOLSM) that I used in Chapters 3 and 4 to simulate values of $\varepsilon_{w/a}$ for the two time-periods. The model results revealed that the values of $\varepsilon_{w/a}$ were not spatially uniform, nor were they same during the Eocene (which some studies assume to be true), depending on the location. The reason for the discrepancies involved differences in temperature, relative humidity, and the seasonality of the isotopic composition of precipitation and water vapor relative to the growing season. The implication of these results is that paleo-climate reconstructions may be inaccurate without accounting for the change in environmental conditions. In fact, the environmental conditions that are attempting to be reconstructed may be causing the inaccurate reconstructions.

References

Adler, R.F., G.J. Huffman, A. Chang, R. Ferraro, P. Xie, J. Janowiak, B. Rudolf, U. Schneider, S. Curtis, D. Bolvin, A. Gruber, J. Susskind, P. Arkin (2003), The Version 2 Global Precipitation Climatology Project (GPCP) Monthly Precipitation Analysis (1979-Present). *J. Hydrometeor*., *4*,1147-1167

Anders, R. J., G. Merland, I. Fung, and E. Matthews (1996), A 1 × 1 distribution of carbon dioxide emissions from fossil fuel consumption and cement manufacture, 1950-1990, *Global Biogeochem. Cycles*, *10*, 419-429.

Baldocchi, D., E. Falge, L. Gu, R. Olson, D. Hollinger, S. Running, P. Anthoni, C. Bernhofer, K. Davis, R. Evans, J. Fuentes, A. Goldstein, G. Katul, B. Law, X. Lee, Y. Malhi, T. Meyers, W. Munger, W. Oechel, K. T. Paw U, K. Pilegaard, H. P. Schmid, R. Valentini, S. Verma, T. Vesala, K. Wilson, S. Wofsy (2001), FLUXNET: a new tool to study the temporal and spatial variability of ecosystem-scale carbon dioxide, water vapor, and energy flux densities, *Bull. Am. Meteorol. Soc*., *82*, 2415–2434.

Ball, J.T., I. E. Woodrow, J. A. Berry (1987), A model predicting stomatal conductance and its contribution to the control of photosynthesis under different environmental conditions. In: Biggins, J. (Ed.), Progress in Photosynthesis Research, vol. 4. Proceedings of the 7th International Congress on Photosynthesis. Martins Nijhoff, Dordrecht, The Netherlands, 221–224.

Bonan, G. (1996), A land surface model (LSM version 1.0) for ecological, hydrological, and atmospheric studies: Technical description and user's guide, TN-417+STR, Natl. Cent. For Atmos. Res., Boulder, Colo.

Brenninkmeier, C., K. Kraft, and W. Mook (1983), Oxygen isotope fractionation between CO_2 and H_2O. *Isot. Geosci. 1*, 181-190.

Brinkhuis, H, S. Schouten, M. E. Collinson, A. Sluijs, J. S. Sinninghe Damsté, G. R. Dickens, M. Huber, T.M. *Cronin*, J. Onodera, K. Takahashi, J. P. Bujak, R. Stein, J van der Burgh, J. S. Eldrett, I. C. Harding, A F. Lotter, F. Sangiorgi, H. van Konijnenburg-van Cittert, J.W. de Leeuw, J. Matthiessen, J. Backman, K. Moran, and the Expedition 302 Scientists (2006), Episodic fresh surface waters in the Eocene Arctic Ocean, *Nature*, *441*, 606–609.

Bony, S., C. Risi, and F. Vimeux (2008), Influence of convective processes on the isotopic composition (δ18O and δD) of precipitation and water vapor in the tropics: 1. Radiative-convective equilibrium and Tropical Ocean–Global Atmosphere–Coupled Ocean-Atmosphere Response Experiment (TOGA-COARE) simulations, *J. Geophys. Res.*, *113*, D19305, doi:10.1029/2008JD009942

Bowen, G. J., and B. Wilkinson (2002), Spatial distribution of $\delta^{18}O$ in meteoric precipitation, *Geology*, *30*, 315-318.

Bowen, G. J. and J. Revenaugh (2003), Interpolating the isotopic composition of modern meteoric precipitation. *Water Resour. Res*., *39*(10), 1299, doi:10.1029/2003WR002086.

Bowen, G. J. (2008), Spatial analysis of the intra-annual variation of precipitation isotope ratios and its climatological corollaries, *J. Geophys. Res*., *113*, D05113, doi:10.1029/2007JD009295.

Brown, J. and I. Simmonds (2004), Sensitivity of the delta-18O-temperature relationship to the distribution of continents, *Geophys. Res. Lett.*, 31, L09208, doi:10.1029/2004GL019870.

Cappa, C. D., M. B. Hendricks, D. J. DePaolo, and R. C. Cohen (2003), Isotopic fractionation of water during evaporation, *J. Geophys. Res.*, *108*(D16), 4525, doi:10.1029/2003JD003597.

Chikaraishi, Y., and H. Naraoka (2003), Compound-specific δD-$\delta^{13}C$ analyses of n-alkanes extracted from terrestrial and aquatic plants. *Phytochemistry*, *63*(3), 361-371.

Chikaraishi, Y., Naraoka, H., Poulson, S.R. (2004), Carbon and hydrogen isotopic fractionation during lipid biosynthesis in a higher plant (Cryptomeria japonica). *Phytochemistry*, *65*, 323-330.

Ciais, P., A.S., Denning, P. P. Tans, J. A. Berry, D. A. Randall, G. J. Collatz, P. J. Sellers, J. W. White, M. Trolier, H. A. J. Meijer, R. J. Francey, P. Monfray, and M. Heimann (1997a), A three-dimensional synthesis study of $\delta^{18}O$ in atmospheric CO_2, Part I: Surface fluxes. *J. Geophys. Res.*, *102*, 5857-5872.

Ciais, P., P. P. Tans, A. S. Denning, R. J. Francey, M. Trollier, H. J. Meijer, J. W. White, J. A. Berry, D. A. Randall, G. J. Collatz, P. J. Sellers, P. Monfray, and M. Heimann (1997b), A three-dimensional synthesis study of $\delta^{18}O$ in atmospheric CO_2, Part II: Simulations with the TM2 transport model. *J. Geophys. Res.*, *102*, 5873-5883.

Ciais, P. and Meijer, H. A. J. (1998), The $^{18}O/^{16}O$ isotope ratio of atmospheric CO2 and its role in global carbon cycle research. In: *Stable isotopes: integration of biological, ecological and geochemical processes* (ed. H. Griffiths), pp. 409-431. Oxford: Bios.

Collatz, G. J., J. T. Ball, C. Grivet, and J. A. Berry (1991), Physiological and environmental regulation of stomatal conductance, photosynthesis, and transpiration: a model that includes a laminar boundary layer. *Agric. For. Meteorol. 54*, 107-136.

Collins, W.D., C.M. Bitz, M.L. Blackmon, G.B. Bonan, C.S. Bretherton, J.A. Carton, P. Chang, S.C. Doney, J.J. Hack, T.B. Henderson, J.T. Kiehl, W.G. Large, D.S. McKenna,

B.D. Santer, and R.D. Smith (2006), The Community Climate System Model: CCSM3. *J. Climate*, *19*, 2122-2143.

Craig, H., and A. Gordon, Deterium and Oxygen-18 variations in the ocean and the marine atmosphere (1965), In: *Stable isotopes in oceanic studies and paleotemperatures* (ed. Laboratory of Geology and Nuclear Sciences), Pisa, Italy.

Cressman, G. P. (1959), An operative objective analysis system, *Mo. Weather Rev.*, *87*, 367-374.

Cuntz, M., P. Ciais, G. Hoffman, and W. Knorr (2003a), A comprehensive global three-dimensional model of $\delta^{18}O$ in atmospheric CO_2: Part I: Validation of surface processes. *J. Geophys. Res.*, *108*(D17), 4527, doi:10.1029/2002JD003153.

Cuntz, M., P. Ciais, G. Hoffman, C. E. Allison, R. J. Francey, W. Knorr, P. P. Tans, J. W. White, and I. Levin (2003b), A comprehensive global three-dimensional model of $\delta^{18}O$ in atmospheric CO_2: Part II: Mapping the atmospheric signal. *J. Geophys. Res.*, *108*(D17), 4528, doi:10.1029/2002JD003154.

Dai, A, T. R. Karl, B. Sun, and K. E. Trenberth (2006), Recent trends in cloudiness over the United States: A tale of monitoring inadequacies. *Bull. Amer. Meteor. Soc.*, *87*, 597-606.

Dansgaard, W. (1964), Stable isotopes in precipitation, *Tellus*, *16*, 436-468.

Dansgaard, W., S. J. Johnsen, J. Moller, and C. C. Langway (1969), One thousand centuries of climatic record from Camp Century on the Greenland ice sheet, *Science*, *166*, 377-381.

Denman, K.L., G. Brasseur, A. Chidthaisong, P. Ciais, P.M. Cox, R.E. Dickinson, D. Hauglustaine, C. Heinze, E. Holland, D. Jacob, U. Lohmann, S Ramachandran, P.L. da Silva Dias, S.C. Wofsy and X. Zhang (2007), Couplings Between Changes in the Climate System and Biogeochemistry. In: *Climate Change 2007: The Physical Science Basis. Contribution of Working Group I to the Fourth Assessment Report of the Intergovernmental Panel on Climate Change* [Solomon, S., D. Qin, M. Manning, Z. Chen, M. Marquis, K.B. Averyt, M.Tignor and H.L. Miller (eds.)]. Cambridge University Press, Cambridge, United Kingdom and New York, NY, USA.

Denning, A. S., G. J. Collatz, C. G. Zhang, D. A. Randall, J. A. Berry, P. J. Sellers, G. D. Colello, and D. A. Dazlich (1996), Simulations of terrestrial carbon metabolism and atmospheric CO_2 in a general circulation model: 1. Surface carbon fluxes, *Tellus, Ser. B*, *48*(4), 521-542.

Dongman, G., H. W. Nürnberg, H Förstel, K. Wagener (1974), On the enrichment of H218O in the leaves of transpiring plants, *Radiation and Environmental Biophysics*, *11*, 41-52.

Epstein, S., C. J. Yapp, J. H. Hall (1976), Determination of the D-H ratio of non-exchangeable hydrogen in cellulose extracted from aquatic and land plants. *Earth and Planetary Science Letters*, *30*(2), 241-251.

Ekaykin, A. A., V. Ya. Lipenkov, N. I. Barkov, J. R. Petit, V. Masson (2001), Izotopniy sostav poverhnostnogo sloya snezhnoy tolschi v rayone stantsii Vostok, Tsentral'naya Antarctida [Isotope composition of surface snow in the vicinity of Vostok Station, central Antarctica]. *Materialy Glyatsiologicheskih Issledovaniy*, *90*, 69-79

Farquhar, G. D. and J. Lloyd (1993), Carbon and oxygen isotope effects in exchange of carbon dioxide between terrestrial plants and the atmosphere *Stable Isotopes and Plant Carbon-Water Relations*, edited by J. R. Ehlleringer *et al.*, pp. 47-70, Academic, San Diego, Calif.

Farquhar, G. D., J. Lloyd, J. A. Taylor, L. B. Flanagan, J. P. Syvertsen, K. T. Hubick, S. Wong, and J. R. Ehleringer (1993), Vegetation effects on the isotope composition of oxygen in atmospheric CO_2. *Nature*, *363*, 439-443.

Federer, B., N. Brichet, and J. Jouzel (1982), Stable isotopes in hailstones, I, the isotopic cloud model, *J. Atmos. Sci.*, *39*, 1323-1336.

Feng, X., A. M. Faiia, and E. S. Posmentier (2009), Seasonality of isotopes in precipitation: A global perspective, *J. Geophys. Res.*, *114*, D08116, doi:10.1029/2008JD011279.

Flanagan, L. B., J. P. Comstock, and J. R. Ehleringer (1991), Comparison of modeled and observed environmental influences on stable oxygen and hydrogen isotope composition of leaf water in Phaseolus-vulgaris L, *Plant Physiology*, *96*, 439-443.

Flanagan, L. B. (2005), Ecosystem CO_2 exchange and variation in the $\delta^{18}O$ of atmospheric CO_2, In Stable Isotopes and Biosphere-Atmosphere Interactions (Eds. Flanagan, L. B., Ehleringer, J. R. & D. E. Pataki). Elsevier-Academic Press, Physiological Ecology Series, San Diego, CA.

Francey, R. J. and P. P. Tans (1987), Latitudinal Variation in O-18 of Atmospheric CO2, *Nature*, *327*, 495-497.

Francey, R. J., P. P. Tans, C. E. Allison, I. G. Enting, J. W. C. White, and M. Trolier (1995), Changes in oceanic and terrestrial uptake since 1982, *Nature*, 373, 326-330.

Fung, I. Y., Field, C. B., Berry, J. A.,Thompson, M. V., Randerson, J. T., Malmstrom, C. M., Vitousek, P. M., Collatz, G. J., Sellers, P. J., Randall, D. A., Denning, A. S., Badeck, F. and J. John (1997), Carbon-13 exchanges between the atmosphere and biosphere, *Global Biogeochem. Cycles*, *11*, 507-533.

Gates, W. L. and A. B. Nelson (1975), A New (Revised Tabulation of the Scripps Topography on a 1 degree Global Grid. Part I. Terrain Heights, RAND CORP.

Gemery, P. A., M. Trolier, and J. W. C. White (1996), Oxygen isotopic exchange between carbon dioxide and water following atmospheric sampling using glass flasks, *J. Geophys. Res.*, *101*, 14,415–14,420.

Gurney, K.R., R. M. Law, A. S. Denning, P. J. Rayner, D. Baker, P. Bousquet, L. Bruhwiler, Y.-H. Chen, P. Ciais, S. Fan, I.Y. Fung, M. Gloor, M. Heimann, K. Higuchi, J. John, T. Maki, S. Maksyutov, K. Masarie, P. Peylin, M. Prather, B.C. Pak, J. Randerson, J. Sarmiento, S. Taguchi, T. Takahashweand C.-W. Yuen (2002), Towards robust regional estimates of CO2 sources and sinks using atmospheric transport models. *Nature*, *415*, 626-630.

Gurney, K. R., et al. (2003), Transcom 3 CO2 inversion intercomparison: 1. Annual mean control results and sensitivity to transport and prior flux information, *Tellus, Ser. B*, *55*, 555– 579.

Gurney, K., et al. (2004), Transcom 3 inversion intercomparison: Model mean results for the estimation of seasonal carbon sources and sinks, *Global Biogeochem. Cycles*, *18*, GB1010, doi:10.1029/2003GB002111.

Gillon, J. S., and D. Yakir (2000), Naturally low carbonic anhydrase activity in C-4 and C-3 plants limit discriminations against (COO)-O-18 during photosynthesis, *Plant Cell Environ*., *23*, 903-915.

Gillon, J.S., Yakir, D. (2001), Influence of carbonic anhydrase activity in terrestrial vegetation on the O-18 content of atmospheric CO2. *Science*, *291*, 2584-2587.

Gilgen, H., M. Wild, and A. Ohmura (1998), Means and trends of shortwave irradiance at the surface estimated from global energy balance archive data. *J. Climate, 11***,** 2042-2061.

Grootes, P. M., M. Stuiver, J. W. C. White, S. Johnsen, and J. Jouzel (1993), Comparing of oxygen isotope records from the GISP2 and GRIP Greenland ice cores, *Nature*, *266*, 552-554.

Gu, L., D. D. Baldocchi, S. C. Wofsy, J. W. Munger, J. J. Michalsky, S. P. Urbanski, and T. A. Boden, (2003) Response of a Deciduous Forest to the Mount Pinatubo Eruption: Enhanced Photosynthesis. *Science 299*, 2035-2038.

Gurney, K.R., R. M. Law, A. S. Denning, P. J. Rayner, D. Baker, P. Bousquet, L. Bruhwiler, Y.-H. Chen, P. Ciais, S. Fan, I.Y. Fung, M. Gloor, M. Heimann, K. Higuchi, J. John, T. Maki, S. Maksyutov, K. Masarie, P. Peylin, M. Prather, B.C. Pak, J. Randerson, J. Sarmiento, S. Taguchi, T. Takahashweand C.-W. Yuen (2002), Towards robust regional estimates of CO2 sources and sinks using atmospheric transport models. *Nature*, *415*, 626-630.

Harley P. C. and J. D. Tenhunen (1991), Modeling the photosynthetic response of C3 leaves to environmental factors. In: K.J. Boote and R.S. Loomis, Editors, *Modeling Crop Photosynthesis—From Biochemistry to Canopy. CSSA Special Publication no. 19*, 17–39.

Hoffmann, G., M. Werner, and M. Heimann (1998), Water isotope module of the ECHAM atmospheric general circulation model - a study on time scales from days to several years, *J. Geophys. Res*, *103* (D14), 16871-16896.

Hoffmann, G., M. Cuntz, C. Weber, P. Ciais, P. Fridlingstein, M. Heimann, J. Jouzel, J. Kaduk, E. Maier-Reimer, U. Seibt, and K. Six (2004), A model of the Earth's Dole effect, *Global Biogeochem Cycles*, *18*, GB1008, doi:10.1029/2003GB002059.

Hollinger, D. Y., J. Aber, B. Dail, E. A. Davidson, S. M. Goltz, H. Hughes, M. Y. Leclerc, J. T. Lee, A. D. Richardson, C. Rodrigues, N. A. Scott, D. Achuatavarier, and J. Walsh (2004), Spatial and temporal variability in forest-atmosphere CO_2 exchange, *Global Change Biology*, *10*, 1689–1706, doi: 10.1111/j.1365-2486.2004.00847.

Horita, J., and D. J. Wesolowski (1994), Liquid-vapor fractionation of oxygen and hydrogen isotopes of water from the freezing to the critical temperature, *Geochim. Cosmochim. Acta*, *58*(16), 3425 – 3437, doi:10.1016/0016-7037(94)90096-5.

Huber, M., and D. Nof (2006), The ocean circulation in the southern hemisphere and its climatic impacts in the Eocene, *Palaeogeogr, palaeoclimatol, palaeoecol* , *231*, 9-28.

Ishizawa, M., Nakazawa, T., Higuchi, K. (2002), A multi-box model study of the role of the biospheric metabolism in the recent decline of $\delta^{18}O$ in atmospheric CO_2, *Tellus*, *Ser. B*, *54,* 307-324.

Isotope Hydrology Section (2006), Global Network of Isotopes in Precipitation. The GNIP Database, http://isohis.iaea.org, Int. At. Energy Agency, Vienna.

Jarvis, P.G. (1976), The interpretation of the variations in leaf water potential and stomatal conductance found in canopies in the field. *Phil. Trans. R. Soc. Lond., Ser. B,* ***273***, 593–610.

Jehren, A. H. and L. S. L. Sternberg (2003), Humidity estimate for the middle Eocene Arctic rain forest, *Geology*, *31*(5), 463–466.

Jones, H.G. and K.H. Higgs (1989), Empirical models of the conductance of leaves in apple orchards. *Plant Cell Environ*., *12*, 301-308.

Joussaume, S., R. Sadourny, and J. Jouzel (1984), A general circulation model of water isotope cycles in the atmosphere, *Nature*, *311*, 24-29.

Jouzel, J., G. L. Russell, R. J. Suozzo, R. D. Koster, J. W. C. White, W. S. Broecker (1987), Simulations of the HDO and H2O-18 atmospheric cycles using the NASA GISS General-Circulation Model – the seasonal cycle for present-day conditions, *J. Geophys. Res*, *92*(D12), 14,739-14,760.

Jouzel, J., N. I. Barkov, J. M. Barnola, M. Bender, J. Chappellaz, C. Genthon, V. M. Kotlyakov, V. Lipenkov, C. Lorius, J. R. Petit, D. Raynaud, G. Raisbeck, C. Ritz, T. Sowers, M. Stievenard, F. Yiou, and P. Yiou (1993), Extending the Vostok ice-core record of palaeoclimate to the penultimate glacial period, *Nature*, *364*, 407-12.

Jouzel, J., C. Waelbroeck, B. Malaize, M. Bender, J.R. Petit, M. Stievenard, N.I. Barkov, J.M. Barnola, T. King, V.M. Kotlyakov, V. Lipenkov, C. Lorius, D. Raynaud, C. Ritz, and T. Sowers. (1996), Climatic interpretation of the recently extended Vostok ice records. *Climate Dynamics*, *12*, 513-521.

Jouzel, J., G. Hoffmann, R. D. Koster, V. Masson (2000), Water isotopes in precipitation: Data/model comparison for present-day and past climates. *Quat. Sci. Rev*, *19*, 363-379.

Kafaki, S. B., Mataji, A., and Hashemi, S. A. (2009), Monitoring Growing Season Length of Deciduous Broad Leaf Forest Derived From Satellite Data in Iran, *Am. J. of Enviorn. Sci., 5*(5), 647-652.

Kalnay, E., M. Kanamitsu, R. Kistler, W. Collins, D. Deaven, L. Gandin, M. Iredell, S. Saha, G. White, J. Woollen, Y. Zhu, M. Chelliah, W. Ebisuzaki, W. Higgins, J. Janowiak, K. C. Mo, C. Ropelewski, J. Wang, A. Leetmaa, R. Reynolds, R. Jenne, and D. Joseph (1996), The NCEP/NCAR 40-Year Reanalysis Project, *Bull. Amer. Meteor. Soc., 77*, 437-470.

Keeling, R. D. (1961), The concentration and isotopic abundance of carbon dioxide in rural and marine air, *Geochim. Cosmochim. Acta, 24*, 277-298.

Keeling, C. D., T. P. Whorf, M. Wahlen, and J. van der Plicht (1995), Interannual extremes in the rate of rise of atmospheric carbon dioxide since 1980, *Nature*, *375*, 666-670.

Kendall, C., and T. B. Coplen (2001), Distribution of oxygen-18 and deuterium in river waters across the United States, *Hydrol. Processes, 15,* 1363-1393.

Leaney, F. W., C. B. Osmond, G. B. Allison, H. Ziegler (1985), Hydrogen-isotope composition of leaf water in C-3 and C-4 plants – its relationship to the hydrogen isotope composition of dry-matter, *Planta*, *164*(2), 215-220.

Lee, K. S., D. B. Wenner, and I. Lee (1999), Using H-and O-isotopic data for estimating the relative contributions of rainy and dry season precipitation to groundwater: Example form Cheju Island, Korea, *J. Hydrol., 222*, 65-74.

Lee, X., R. Smith, and J. Williams (2006), Water vapour 18O/16) isotope ratio in surface air in New England, USA, *Tellus*, *Ser. B*, *58,* 293–304.

Lee, J. E., I. Fung, D. J. DePaolo, C. C. Henning (2007), Analysis of the global distribution of water isotopes using the NCAR atmospheric general circulation model, *J. Geophys. Res*, *112*, D16306 doi: 10.1029/2006JD007657.

LeGrande, A.N., and G.A. Schmidt (2006), Global gridded data set of the oxygen isotopic composition in seawater. *Geophys. Res. Lett.*, *33*, L12604, doi:10.1029/2006GL026011.

Liu W., H. Yang, L. Liwu (2006), Hydrogen isotopic composition of *n*-alkanes from terrestrial plants correlate with their ecological life forms, *Oceologia*, *150*, 330-338.

Lipenkov, V., A. A. Ekaykin, N. I. Barkov, and M. Pourchet (1998), On the relation between surface snow density in Antarctica and wind speed (in Russian). *Data of Glaciological Studies*, *85*, 148-158.

Lorius, C., L. Merlivat, J. Jouzel, and M. Pourchet (1979), A 30,000 year isotope record from Antarctic ice, *Nature*, *280*, 644-648.

Lu, E., and X. Zeng (2005), Understanding different precipitation seasonality regimes from water vapor and temperature fields: Case studies, *Geophys. Res. Lett.*, *32*, L22707, doi:10.1029/2005GL024333.

Lu, E. and E. S. Takle (2010), Concurrent variations of water vapor and temperature corresponding to the interannual variation of precipitation in the North American Regional Reanalysis, *J. Geophys. Res. 115*, D11101, doi:10.1029/2009JD012956.

Masson-Delmotte, V., S. Hou, A. Ekaykin, J. Jouzel, A. Aristarain, R. T. Bernardo, D. Bromwich, O. Cattani, M. Delmotte, S. Falourd, M. Frezzotti, H. Gallée, L.Genoni, E. Isaksson, A. Landais, M. Helsen, G. Hoffmann, J. Lopez, V. Morgan, H. Motoyama, D. Noone, H. Oerter, J.R. Petit, A. Royer, R. Uemura, G. A. Schmidt, E. Schlosser, J. C. Simões, E. J. Steig, B. Stenni, M. Stievenard, M. R. van den Broeke, R. S. W. van de Wal, W. J. van de Berg, F. Vimeux, and J.W.C. White (2008). A review of Antarctic surface snow isotopic composition: observations, atmospheric circulation and isotopic modelling. *J. of Climate*, *21* (13), 3359-3387, doi: 10.1175/2007JCLI2139.1.

Majoube, M. (1971), Factionnement en oxygene-18 te en deuterium entre l'eau et sa vapeur, *J. Clim. Phys.* 58, 1423-1436.

Mathieu, R., and T. Bariac (1996), A numerical model of the simulation of stable isotope profiles in drying soils, *J. Geophys. Res. 101*, 12,685-12,696.

Mayewski, P., and S. Whitlow (2000), South Pole snow pit, National Snow and Ice Data Center, Boulder, CO.

Meehl, G.A., T.F. Stocker, W.D. Collins, P. Friedlingstein, A.T. Gaye, J.M. Gregory, A. Kitoh, R. Knutti, J.M. Murphy, A. Noda, S.C.B. Raper, I.G. Watterson, A.J. Weaver and Z.-C. Zhao (2007), Global Climate Projections. In: *Climate Change 2007: The Physical Science Basis. Contribution of Working Group I to the Fourth Assessment Report of the Intergovernmental Panel on Climate Change* [Solomon, S., D. Qin, M. Manning, Z. Chen, M. Marquis, K.B. Averyt, M. Tignor and H.L. Miller (eds.)]. Cambridge University Press, Cambridge, United Kingdom and New York, NY, USA.

Menzel, A. and P. Fabian (1999), Growing season extended in Europe. *Nature*, *397*, 659, doi:10.1038/17709.

Michaelson, J. (1987), Cross-validation in statistical climate forecast models. *J. Climate Appl. Meteor.*, *26*, 1589-1600.

Miller, J. B., D. Yakir, J. W. C. White, and P. P. Tans (1999), Measurements of O-18/O-16 in the soil-atmosphere CO_2 flux. *Global Biogeochem. Cycles 13*, 761-774.

Mitchell, K. E., D. Lohmann, P. R. Houser, J. C. Schaake, A. Robock, B. A. Cosgrove, J. Sheffield, Q. Duan, L. Luo, R. W. Higgins, R. T. Pinker, J. D. Tarpley, D. P. Lettenmaier, C. H. Marshall, J. K. Entin, M. Pan, W. Shi, V. Koren, J. Meng, B. H. Ramsay, A. A. Bailey (2004), The multi-institution North American Land Data Assimilation System (NLDAS): Utilizing multiple GCIP products and partners in a continental distributed hydrological modeling system. *J. Geophys. Res.*, 109 D18102, doi:10.1029/2004JD004583.

Naegler, T., P. Ciais, K. Rodgers, and I. Levin (2006), Excess radiocarbon constraints on air-sea gas exchange and the uptake of CO2 by the oceans, *Geophys. Res. Lett.*, *33*, L11802, doi:10.1029/2005GL025408.

Nemani, R. R., C. D. Keeling, H. Hashimoto, W. M. Jolly, S. C. Piper, C. J. Tucker, R. B. Myneni, S. W. Running (2003), Climate-Driven Increases in Global Terrestrial Net Primary Production from 1982 to 1999, *Science*, *300*, 1560-1563.

New, M., M. Hulme, and P. Jones (1999), Representing twentieth-century space-time climate variability, Part I: Development of a 1961-90 mean monthly terrestrial climatology. *J. Climate*, *12*, 829-856.

Noone, D., and I. Simmonds (2002), Associations between delta O-18 of water and climate parameters in a simulation of atmospheric circulation for 1979-95, *J. of Climate*, *15* (22), 3150-3169.

Noone, D., C. Still and W. Riley (2002), A global biophysical model of 18O in terrestrial water and CO2 fluxes. Research Activities in Atmospheric and Oceanic Modeling, Report No. 32, H. Ritchie, Ed., World Meteorological Organization, 4.19-4.20.

Noone, D. (2003), Water isotopes in CCSM for studying water cycles in the climate system. Eighth Annual CCSM Workshop, Breckenridge, CO.

Noone, D. (2006), Isotopic composition of water vapor modeled by constraining global climate simulations with reanalyses. Research Activities in Atmospheric and Oceanic Modelling, J. Cote (Ed.), *35*, 2-37 pp.

Noone, D., (2006), 130-year trends and variability in the isotopic composition of meteoric water from the Stable Water-isotope Intercomparison Group experiments. *EOS Trans. AGU*, 87 *Fall Meet. Assem. Suppl.*, Abstract B11E-02.

Noone, D. (2008), The influence of midlatitude and tropical overturning circulation on the isotopic composition of atmospheric water vapor and Antarctic precipitation *J. Geophys. Res., 113*, D04102, doi:10.1029/2007JD008892.

Noone, D., and C. Sturm (2009), Comprehensive dynamical models of global and regional water isotope distributions. In: West, J., G. Bowen, T. Dawson and K. Tu (eds.) Isoscapes: Understanding movement, patterns, and process on Earth through isotope mapping. Springer, in press.

Ogée, P. Peylin, M. Cuntz, T. Bariac, Y. Brunet, P. Berbigier, P. Richard, and P. Ciais (2004) Partitioning net ecosystem carbon exchange into net assimilation and respiration with canopy-scale isotopic measurements: an error propagation analysis with 13CO2 and CO18O, *Glob. Biogeochem. Cycles*, *18* (2), GB2019, doi:10.1029/2003GB002166.

Pearson, P. N., B. E. van Dongen, C. J. Nicholas, R. D. Pancost, S. Schouten, J. M. Singano, B. S. Wade (2007), Stable warm tropical climate through the Eocene Epoch, *Geology*, *35*(3), 211-214.

Petit, J.R., J. Jouzel, D. Raynaud, N.I. Barkov, J.-M. Barnola, I. Basile, M. Bender, J. Chappellaz, M. Davis, G. Delayque, M. Delmotte, V.M. Kotlyakov, M. Legrand, V.Y. Lipenkov, C. Lorius, L. Pépin, C. Ritz, E. Saltzman, and M. Stievenard (1999), Climate and atmospheric history of the past 420,000 years from the Vostok ice core, Antarctica, *Nature*, *399*, 429-436.

Peylin, P., P. Ciais, S. Denning, P. P. Tans, J. A. Berry, and J. W. C. White (1999), A 3-dimensional study of $\delta^{18}O$ in atmospheric CO_2: contribution of different land ecosystems. *Tellus*, *Ser. B*, *51*, 642-667.

Potter, C. S. (1999), Terrestrial biomass and the effects of deforestation on the global carbon cycle, *BioScience*, *49*, 769– 778.

Potter, C. S., S. A. Klooster, and V. Brooks (1999), Interannual variability in terrestrial net primary production: Exploration of trends and controls on regional to global scales, *Ecosystems*, *2*, 36– 48.

Quay, P. D., B. Tilbrook, C. S. Wong (1992), Oceanic Uptake of Fossil Fuel CO2: Carbon-13 Evidence, *Science*, *256*, 74-79.

Qian, T., A. Dai, K. E. Trenberth, and K. W. Oleson (2006), Simulation of global land surface conditions from 1948-2004. Part I: Forcing data and evaluation. *J. Hydrometeorology*, *7*, 953-975.

Rayner, P. J., Law, R. M., Allison, C. E., Francey, R. J., Trudinger, C. M., Pickett-Heaps, C. (2008), Interannual variability of the global carbon cycle (1992-2005) inferred by inversion of atmospheric CO2 and delta(CO2)-C-13 measurements, *Global Biogeochemical Cycles*, *22*(3), GB3008.

Richardson, A. D., D. Y. Hollinger, D. B. Dail, J. T. Lee, J. W. Munger, and J. O'Keefe (2009), Influence of spring phenology on seasonal and annual carbon balance in two contrasting New England forests, *Tree Physiology*, *29*, 321–331.

Riley, W. J., C. J. Still, M. Torn, and J. A. Berry (2002), A mechanistic model of $H_2{}^{18}O$ and CO18O fluxes between ecosystems and atmosphere: model description and sensitivity analyses. *Global Biogeochem. Cycles*, *16*, 1095-1108.

Riley, W. J., C. J. Still, B. R. Helliker, M. Ribas-Carbo, and J. A. Berry (2003), 18O composition of CO2 and H2O ecosystem pools and fluxes in a tallgrass prairie: Simulations and comparisons to measurements, *Global Change Biol.*, *9(11)*, 1567-1581.

Riley, W. J. (2005), A modeling study of the impact of the delta O-18 value of near-surface soil water on the delta O-18 value of the soil-surface CO2 Flux. *Geochemica et Cosmochemica Acta, 69*(8), 1939-1946.

Risi, C., S. Bony, F. Vimeux (2008), Influence of convective processes on the isotopic composition (delta O-18 and delta D) of precipitation and water vapor in the tropics: 2. Physical interpretation of the amount effect. *J. Geophys. Res*, *113*, D19306, doi: 10.1029/2008JD009943.

Roderick, M. L., G. D. Farquhar, S. L. Berry, and J. R. Noble (2001), On the direct effect of clouds and atmospheric particles on the productivity and structure of vegetation. *Oecologia, 129*(1), 21-30.

Sachse, D., J. Radke, G. Gleixner (2004) Hydrogen isotope ratios of recent lacustrine sedimentary n-alkanes record modern climate variability, *Geochimica et Cosmochimica Acta*, *68*(23), 4877-4889.

Sachse, D., J. Radke, G. Gleixner (2006), δD values of individual *n*-alkanes from terrestrial plants along a climatic gradient – Implications ofr the sedimentary biomarker record, *Org. Geochem*, *37*, 469-483.

Sarmiento, J. L. and N. Gruber (2002), Sinks for Anthropogenic Carbon. *Physics Today 55*(8), 30-36.

Schneider, D. P., and D. C. Noone (2007), Spatial covariance of water isotopes in ice cores during 20th Century climate change. *J. Geophys. Res*, *112*, D18105, doi:10.1029/2007JD008652.

Sessions, A. L., T. W. Burgoyne, A. Schimmelmann, J. M. Hayes (1999), Fractionation of hydrogen isotopes in lipid biosynthesis, *Org. Geochem., 30*, 1193-1200.

Sewall, J. O., L. C. Sloan, M. Huber, and S. Wing (2000), Climate sensitivity to changes in land surface characteristics, *Global and Planetary Change*, *26*, 445-465.

Smith, F. A., K. H. Freeman (2006), Influence of physiology and climate on δD of leaf wax n-alkanes from C3 and C4 grasses, *Geochimica et Cosmochimica Acta*, *70*, 1172-1187.

Speelman, E. N., J. O. Sewall, D. Noone, M. Huber, A. von der Heydt, J. S. Damsté, G. Reichart (submitted) Modeling the influence of a reduced equator-to-pole sea surface temperature gradient on the distribution of water isotopes in the Eocene, *submitted to Earth and Planetary Science Letters.*

Steig, E. J., P. A. Mayewski, D. A. Dixon, M. M. Frey, S. D. Kaspari, D. P. Schneider, S. A. Arcone, G. S. Hamilton, V. B. Spikes, M. Albert, D. Meese, A. J. Gow, C. A. Shuman, J. W. C. White, S. Sneed, J. Flaherty, M. Wumkes (2005), High-resolution ice cores from US-ITASE (West Antarctica): development and validation of chronologies and determination of precision and accuracy, *Annals of Glaciology*, *41*, 77-84.

Stern, L.A., Amundson, R., Baisden. W.T. (2001), Influence of soils on oxygen isotope ratio of atmospheric CO2, *Global Biogeochemical Cycles, 15*, 753-759.

Stewart, J.B. (1988), Modelling surface conductance of Pine forest. *Agric. For. Meteorol.*, *43*, 19-35.

Stewart, M. K. (1975), Stable isotope fractionation due to evaporation and isotopic exchange of falling water drops: applications to atmospheric processes and evaporation of lakes. *J. Geophys. Res. 80*, 1133–1146.

Still, C. J., W. J. Riley, S. C. Biraud, D. Noone, N. H. Buenning, J. T. Randerson, M. S. Torn, J. Welker, J. W. C. White, R. Vachon, G. D. Farquhar, and J. A. Berry (2009), The influence of clouds and diffuse radiation on ecosystem-atmosphere CO_2 and $CO^{18}O$

exchanges, *Journal of Geophysycal Research-Biogeosciences*, *114*, G01018, doi:10.1029/2008JG000675.

Takahashi, T., S. C. Sutherland, C. Sweeney, A. Poisson, N. Metzl, B. Tillbrook, N. Bates, R. Wanninkhof, R. A. Feely, C. Sabine, J. Olafsson, and Y. Nojiri (2002), Global sea-air CO2 flux based on climatological surface ocean pCO2, and seasonal biological and temperature effects, *Deep-Sea Res. II*, *49*, 1601-1622.

Tans, P. P. (1998), Oxygen isotopic equilibrium between carbon dioxide and water in soils, *Tellus*, *Ser. B*, *50*, 163-178.

Thompson, L. G., E. Mosley-Thompson, M. E. Davis, P. N. Lin, K. A. Henderson, J. Cole-Dai, J. F. Bolzan, and K. B. Liu (1995), Late glacial stage and Holocene tropical ice core records from Huscaran, Peru, *Science*, *269*, 46-50.

Trenberth, K.E., P.D. Jones, P. Ambenje, R. Bojariu, D. Easterling, A. Klein Tank, D. Parker, F. Rahimzadeh, J.A. Renwick, M. Rusticucci, B. Soden and P. Zhai, (2007), Observations: Surface and Atmospheric Climate Change. In: *Climate Change 2007: The Physical Science Basis*. Contribution of Working Group I to the Fourth Assessment Report of the Intergovernmental Panel on Climate Change [Solomon, S., D. Qin, M. Manning, Z. Chen, M. Marquis, K.B. Averyt, M. Tignor and H.L. Miller (eds.)]. Cambridge University Press, Cambridge, United Kingdom and New York, NY, USA.

Vachon, R. W., J. W. C. White, E. Gutmann, and J. M. Welker (2007), Amount-weighted annual isotopic values are affected by the seasonality of precipitation: A sensitivity study, *Geophys. Res. Lett.*, *34*, L21707, doi:10.1029/2007GL030547.

Van der Werf, G.R., J.T. Randerson, L.Giglio, G.J. Collatz, and P.S. Kasibhatla (2006), Interannual variability in global biomass burning emission from 1997 to 2004, *Atmospheric Chemistry and Physics*, 6, 3423-3441. SRef-ID: 16807324/acp/2006-6-3423, 2006.

Vimeux, F., V Masson, J. Jouzel, J. R. Petit, E. J. Steig, M. Stievenard, R. Vaikmac, and J. W. C. White (2001), Holocene hydrological cycle changes in Southern Hemisphere documented in East Antarctic deuterium excess records, *Clim Dyn.*, *19*, 503-513.

Vogel, J. C., P. M. Grootes, and W. G. Mook (1970), Isotopic fractionation between gaseous and dissolved carbon dioxide, *Z. Phys.*, *230*, 225-238.

Welker, J. (2000), Isotopic ($\delta^{18}O$) characteristics of weekly precipitation collected across the USA: An initial analysis with application to water source studies, Hydrol. Processes, 14, 1449 – 1464, doi:10.1002/1099- 1085(20000615)14:8<1449::AID-HYP993>3.0.CO;2-7.

Wen, X.-F., S.-C. Zhang, X.-M. Sun, G.-R. Yu, and X. Lee (2010), Water vapor and precipitationisotope ratios in Bejing, China, *J. Geophys. Res.*, 115, D01103, doi:10.1029/2009JD012408.

Werner, M., U. Mikolajewicz, M. Heimann, and G. Hoffmann (2000), Borehole Versus Isotope Temperatures on Greenland: Seasonality Does Matter, *Geophys. Res. Lett.*, *27(5)*, 723–726.

Werner, M., et al., (2004) SWING - The Stable Water Isotope Intercomparison Group: *Eos Trans. AGU*, 85 Fall Meet. Assem. Suppl., Abstract C51B-1034.

Worden, J., D. Noone, K. Bowman (2007), Importance of rain evaporation and continental convection in the tropical water cycle, *Nature*, *445*, 528-532.

White, J. and B. Vaughn (2009), University of Colorado, Institute of Arctic and Alpine Research (INSTAAR), Stable Isotopic Composition of Atmospheric Carbon Dioxide (13C and 18O) from the NOAA ESRL Carbon Cycle Cooperative Global Air Sampling Network, 1990-2007, Version: 2009-06-01, Path: ftp://ftp.cmdl.noaa.gov/ccg/co2o18/flask/event/.

Wong, S.C., I.R Cowan,, G.D. Farquhar (1978), Leaf conductance in relation to assimilation in *Eucalyptus pauciflora* Sieb. cx Spreng: Influence of irradiance and partial pressure of carbon dioxide. *Plant Physiol., 62*, 670–674.

Xie, P. P. and P. A. Arkin (1997), Global precipitation: a 17-year monthly analysis based on gauge observations, satellite estimates, and numerical model outputs. *Bull. Amer. Meteor. Soc., 78*, 2539-2558.

Yakir, D., and L. D. L. Sternberg (2000), The use of stable isotopes to study ecosystem gas exchange, Oecologia, *123(3)*, 297 – 311, doi:10.1007/s004420051016.

Yang, H., Y. Huang (2003), Preservation of lipid hydrogen isotope ratios in Miocene lacustrine sediments and plant fossils at Clarkia, northern Idaho, USA, *Organic Geochemistry*, *34*, 413-423.

Zhang, Y.-C., W. B. Rossow, A. A. Lacis, V. Oinas, and M. I. Mishchenko (2004), Calculation of radiative fluxes from thesurface to top of atmosphere based on ISCCP and other global data sets: Refinements of the radiative transfer model and the input data. *J. Geophys. Res., 109***,** D19105, doi:10.1029/2003JD004457.

Zhang, X, Z Yang, G Niu, X Waag (2009), Stable water isotope simulation in different reservoirs of Manaus, Brazil, by Community Land Model incorporating stable isotopic effect, *Int J. Climatol.*, *29*, 619-628.